

A Size-Adaptive Radiofrequency Coil with Integrated NMR Field Probes for Magnetic Resonance Imaging of the Pediatric Human Brain at 7 T

Christian Sprang

Department of Biological and Biomedical Engineering

McGill University

Montreal, Quebec, Canada

October 2023

A thesis submitted to McGill University in partial fulfillment of the requirements of a degree of
Master of Engineering

© Christian Sprang, 2023

Abstract

Ultra-high field (UHF), 7 Tesla (T) magnetic resonance imaging (MRI) has advanced human brain imaging by enabling higher spatial and spectral resolution, improved tissue contrast and increased signal-to-noise ratio (SNR) compared to MR imaging at clinical field strengths (1.5 T, 3 T). Nonetheless, the advantages of 7 T MRI are coupled with an increase in specific absorption rate (SAR). This can result in tissue heating and is an additional safety consideration for the design of safe 7 T MRI coils. Because of SAR considerations, there are currently no commercially available 7 T MRI radiofrequency (RF) head coils for imaging pediatric subjects with body weights below 30 kg. Consequently, pediatric neurodevelopmental researchers are presently precluded from leveraging the advantages of 7 T MRI. In addition to SAR, pediatric neuroimaging is further complicated by the variations in head size among pediatric subjects during neurodevelopment. This can result in alterations in electromagnetic (EM) coupling between brain tissue and the MRI coil system. Pediatric neuroimaging is also more prone to image artifacts and data loss due to subject motion. In this thesis, we present the design and construction of a novel, size-adaptive RF head coil with integrated field monitoring Nuclear Magnetic Resonance (NMR) probes for whole brain, pediatric MRI at 7 T. The coil consists of an 8-channel parallel transmit (pTx) coil and a 32-channel, conformal receive (Rx) phased array. The transmit (Tx) coil consists of 8 dipole antennas optimized to provide coverage and uniform excitation over the entire head. A commercial field monitoring system consisting of 16 NMR field probes is integrated into the coil to allow for retrospective correction of image data. The Rx coil consists of 32 magnet wire loop elements mounted on a custom, size-adjustable, 3D printed housing. The housing is designed to be adjustable in the lateral-medial and anterior-posterior directions to accommodate subjects with head sizes ranging from the 5th to the 95th percentile of children aged 4-9 years. The performance of the coil with and without integrated NMR field probes and at the largest and smallest dimensions of the Rx housing was evaluated based on SNR, scattering parameters, noise correlation matrices, and transmit efficiency. Simulations of transmit efficiency and SAR performance demonstrated that the coil is safe for pediatric neuroimaging at 7 T. MR Imaging and workbench test results showed small but measurable changes in coil and probe performance with different coil configurations. Preliminary evaluations of coil performance in phantom imaging demonstrated it

has comparable SNR to a commercially available 8-channel transmit, 32-channel receive head coil (Nova Medical Head Coil). This was particularly true when the size of the proposed pediatric coil was well-adjusted to match the dimensions of the imaged sample. With *in vivo* MRI experiments, we demonstrated that the proposed pediatric coil was capable of producing high-quality structural images over the entire human brain. Overall, the results support the potential of the proposed head coil for accurate, reproducible and safe pediatric brain imaging at 7 T.

Résumé

L'imagerie par résonance magnétique (IRM) à champ ultra-élevé (UHF) de 7 Tesla (T) a fait progresser l'imagerie du cerveau humain en permettant une résolution spatiale et spectrale plus élevée, un contraste tissulaire amélioré et un rapport signal/bruit (SNR) augmenté par rapport à l'imagerie IRM aux intensités de champ clinique (1,5 T, 3 T). Néanmoins, les avantages de l'IRM 7 T s'accompagnent d'une augmentation du débit d'absorption spécifique (DAS). Cela peut entraîner un échauffement des tissus et constitue une considération de sécurité supplémentaire pour le développement de bobines IRM 7 T sécuritaire. En raison de considérations liées au DAS, il n'existe actuellement aucune bobine de tête radiofréquence (RF) IRM 7 T disponible dans le commerce pour l'imagerie des sujets pédiatriques pesant moins de 30 kg. Par conséquent, les chercheurs en neurodéveloppement pédiatrique ne peuvent actuellement pas bénéficier des avantages de l'IRM 7 T. Outre le SAR, la neuroimagerie pédiatrique est encore compliquée par les variations de la taille de la tête chez les sujets pédiatriques au cours du développement neurologique. Cela peut entraîner des altérations du couplage électromagnétique (EM) entre le tissu cérébral et le système de bobines IRM. La neuroimagerie pédiatrique est également souvent affligée d'artefacts d'image et par la perte de données dus au mouvement du sujet. Dans cette thèse, nous présentons la conception d'une nouvelle bobine de tête RF adaptative en taille avec des sondes de résonance magnétique nucléaire (RMN) de surveillance de champ pour l'IRM du cerveau pédiatrique entier à 7 T. La bobine se compose d'une bobine de transmission parallèle (pTx) à huit canaux et un réseau multiéléments de réception (Rx) à 32 canaux. La bobine d'émission (Tx) se compose de huit antennes dipôles optimisées pour fournir une couverture et une excitation uniforme de toute la tête. Un système de surveillance de champ commercial composé de 16 sondes de champ RMN est intégré à la bobine pour permettre une correction rétrospective des données d'image. La bobine Rx se compose de 32 éléments de boucle de fil magnétique montés sur un casque imprimé en 3D et de taille réglable. Le casque est réglable dans les directions latérale-médiale et antéro-postérieure pour conformer à des sujets dont la taille de tête varie du 5e au 95e percentile des enfants âgés de 4 à 9 ans. Les performances de la bobine avec et sans sondes de champ RMN et dans les dimensions les plus grandes et les plus petites du casque Rx ont été évaluées sur la base du SNR, des paramètres de diffusion, des matrices de corrélation de bruit et

de l'efficacité du champ de transmission. Les simulations de DAS et de l'efficacité de la bobine de transmission ont démontré que la bobine est sûre pour la neuroimagerie pédiatrique à 7 T. Les résultats des tests d'imagerie et en laboratoire ont démontré des changements mineurs mais mesurables dans les performances de la bobine et des sondes avec différentes configurations de bobine. Des évaluations préliminaires des performances de la bobine en imagerie fantôme ont démontré que son rapport signal/bruit est comparable à celui d'une bobine de tête à 8 canaux de transmission et 32 canaux de réception disponible dans le commerce (Nova Medical). Cela était particulièrement vrai lorsque la taille de la bobine pédiatrique était bien ajustée pour correspondre aux dimensions du fantôme. Grâce à des expériences d'IRM in vivo, nous avons démontré que la bobine pédiatrique était capable de produire des images structurelles sur l'ensemble du cerveau humain. Dans l'ensemble, les résultats confirment le potentiel de la bobine de tête proposée pour une imagerie cérébrale pédiatrique précise, reproductible et sûre à 7 T.

Acknowledgements

I would like to thank my supervisor, Prof. David Rudko, for all his support and guidance throughout my graduate work. I couldn't have asked for a kinder, more knowledgeable, and more inspiring supervisor, and I feel privileged to have had such an exceptional role model during my time at McGill.

I would also like to thank Pedram Yazdanbakhsh Ph.D., whose expertise in RF coil design was crucial to the success of this project. It is no understatement to say that Pedram is a master Jedi in the art of coil design, and I am grateful to have had the opportunity to be his padawan.

I would also like to thank my co-supervisor, Prof. Christine Tardif for her support and advice throughout my graduate degree.

I would like to thank Marcus Couch Ph.D. and Sajjad Feizollah for all their assistance in implementing the imaging sequences that form the bulk of the results of this work. I would also like to thank them for all their help throughout the data analysis process. Additionally, I'd like to thank the MRI technologists at the McConnell Brain Imaging Centre, David Costa, Ron Lopez and Soheil Mollamohseni Quchani, for their assistance in performing human imaging experiments. I would also like to acknowledge Mike Ferreira, who assisted in the coordination of all component orders, ensuring the timely completion of the project. Additionally, I would like to thank Paul Weavers Ph.D. and Cameron Cushing of Skope Magnetic Resonance Technologies, whose insights helped propel the project forward. I would also like to thank Mahmoud Ebesh of OSSY House Inc. for his helpful advice regarding mechanical design.

I would also like to thank my fellow lab members for all their support, notably, Johnny Der Hovagimian, Vladimir Grouza, Michael Caouette-Mansour, Hande Halilibrahimoglu, Risavarshni Thevakumaran, Ilana Leppert and Jana Strizak. I am fortunate to have had the opportunity to work with such wonderful people.

I would like to thank my friends, whose support and company have made my master's, and my life in general, more fulfilling. I would especially like to thank Tessa Warburton for all of her support, kindness and good humour.

Lastly, I would like to thank my brother and sister, Benjamin and Evelyne Sprang, and my father and mother, Geoff Sprang and Michèle Caveen for their unconditional love and support.

Contribution of Authors

The objectives and methodologies of this work were developed by Christian Sprang with the assistance of his supervisors, Prof. David Rudko and Prof. Christine Tardif, and the manager of the RF laboratory at the McConnell Brain Imaging Centre of the Montreal Neurological Institute, Pedram Yazdanbakhsh Ph.D.. Christian Sprang designed all mechanical hardware components presented in this thesis, and designed and assembled the receive radiofrequency coil of the full pediatric coil array with the guidance of Pedram Yazdanbakhsh Ph.D.. All simulations presented in this work were performed by Pedram Yazdanbakhsh Ph.D.. The transmit radiofrequency coil of the final pediatric coil array was also designed and built by Pedram Yazdanbakhsh Ph.D., with the assistance of Christian Sprang. Imaging experiments were performed with the assistance of Marcus Couch Ph.D., the Siemens MR Collaboration Scientist at the McConnell Brain Imaging Centre of the Montreal Neurological Institute, and Sajjad Feizollah, a graduate student in Prof. Tardif's lab. Data analysis was performed by Christian Sprang, with the assistance of Marcus Couch Ph.D. and Mr. Feizollah. Offline Skope reconstruction was performed by Mr. Feizollah. Christian Sprang wrote the manuscript in Chapter 5, which was revised by all co-authors.

Table of Contents

Abstract	i
Résumé	iii
Acknowledgements	v
Contribution of Authors	vi
Table of Contents	vii
List of Figures	x
List of Tables	xiii
List of Abbreviations.....	xiv
Chapter 1 – Introduction.....	1
Chapter 2 – Principles of Magnetic Resonance Imaging	5
2.1 NMR Principles.....	5
2.2 Spin Systems and Bulk Magnetization	7
2.3 The Rotating Reference Frame	7
2.4 Generating the MR Signal	8
2.5 Relaxation	10
2.6 The Bloch Equations	11
2.7 Detecting the MR Signal.....	11
2.8 Spatial Encoding: from a 1D signal to a 2D image.....	12
Chapter 3 – Principles of RF Coil Design.....	15
3.1 Fundamental Principles of RF Coils.....	15
3.1.1 Transmit Coil: Principles of Operation.....	15
3.1.2 Receive Coil: Principles of Operation	18
3.2 RF Coil Classes	19
3.2.1 Surface Coils	19
3.2.2 Surface Coil Arrays	20
3.2.3 Volume Coils.....	21
3.2.4 Volume Coils at UHF: Parallel Transmit Coils (pTx).....	22
3.3 Coil Safety Considerations: SAR.....	22
3.3.1 Electric Fields in MRI: Conservative vs. Non-Conservative.....	23

3.3.2 Modelling SAR.....	23
3.3.3 SAR Limits.....	24
3.4 RF Coil Design.....	25
3.4.1 Resonance	25
3.4.2 Impedance Matching.....	26
3.4.3 Geometric Decoupling (Phased Arrays)	27
3.4.4 Coil Safety Features: Coil Detuning.....	28
3.4.5 Eliminating Common-Mode Currents: Cable traps and Baluns.....	30
3.4.6 Preamplifier Decoupling (receive arrays).....	31
3.5 Coil Design and the RF Lab.....	32
3.5.1 Simulation	32
3.5.2 Vector Network Analyzer (VNA)	32
3.6 Coil Performance Metrics.....	33
3.6.1 Quantifying Coil Losses (Quality Factor).....	33
3.6.2 Signal-to-Noise Ratio (SNR)	34
3.6.3 B_1^+ Efficiency and Homogeneity	35
3.6.4 Parallel Imaging and the Geometry Factor (g-Factor).....	35
3.7 Concurrent Studies in Size-Adaptive RF Coil Design	36
Chapter 4 – Nuclear Magnetic Resonance (NMR) Field Probes.....	41
4.1 NMR Probe Design	41
4.2 Principles of Operation	42
4.3 NMR Probes in MRI	42
4.4 Principles of NMR Field Probe Array Operation.....	43
4.5 Concurrent Studies in Integrated NMR Field Probe and RF Coil Design.....	46
Chapter 5 - Manuscript.....	51
Abstract.....	53
Introduction.....	54
Methods	55
RF Coil Design.....	55
Coil Performance and Imaging	61
Results	63
Transmit Coil	63

Receive Coil.....	67
NMR Probe Performance	71
Discussion.....	74
Acknowledgements	76
References.....	77
Chapter 6 – Discussion and Conclusion.....	80
6.1 Discussion of Transmit Coil Results	80
6.2 Discussion of Receive Coil Results.....	84
6.3 NMR Field Probe Results	87
6.4 Imaging Results.....	87
6.5 Future Directions.....	89
6.6 Conclusion	91
References	93
Appendix	98
Updated Rx Former Design	98

List of Figures

Figure 1: Function of a) transmit element and b) receive element.	18
Figure 2: Resonance splitting at the Larmor frequency (f_0) because of coupling between two coil elements.	21
Figure 3: LC resonant loop with tuning capacitor (C_{tune}), matching capacitor (C_m), and capacitor C_2 (equal to $2 \times C_{\text{tune}}$).	26
Figure 4: Two overlapped loop elements, with overlap shown in red.	28
Figure 5: A receive loop with a) active detuning circuit, activated by forward biasing a PIN diode (D_a) with an external DC input isolated from RF current by an RF choke (RFC), and b) passive detuning circuit, activated when the cross diode (D_p) is forward biased by an excessive voltage across its terminals.	29
Figure 6: Example of a cable trap. Here the coiled coaxial cable forms the inductance of the LC circuit, and a lumped element capacitor forms the capacitance.	31
Figure 7: Diagram of an NMR probe. In this specific design, the susceptibility of the probe casing is matched to the susceptibility of the solenoid wire to minimize the effects of susceptibility on the magnetic field measurement. ⁴⁹	41
Figure 8: Mechanical design of pediatric coil receive and transmit former: a) CAD model of combined Tx (white) and Rx (grey) coil formers without the outer Tx cylinder, b) Rx coil former adjusted to smallest size, c) Rx coil former adjusted to largest size, d) mechanical components of Rx coil former (i) superior, ii) posterior, iii) anterior, iv) right, v) left), e) receive coil with electronic components, f) Tx coil with electronic components, g) combined Rx and Tx coils with integrated Skope NMR field probes.	57
Figure 9: Electrical circuit diagrams and images of: a) transmit dipole, b) preamplifier interface board, c) passive detuning circuit, d) active detuning circuit, matching circuit and loop output, e) receive loop, f) receive loops, cabling and cable traps, g) receive loop circuit diagram showing passive detuning, active detuning and preamplifier decoupling circuits, and h) transmit dipole circuit with active detuning.	60
Figure 10: a) Simulated B_1^+ map in phantom and experimental B_1^+ efficiency map for all pediatric coil configurations (from left to right: largest coil size, largest coil size with integrated field probes, smallest coil size, smallest coil size with field probes), b) Simulated B_1^+ efficiency and SAR maps in pediatric head voxel model and c) simulated B_1^+ efficiency and SAR maps in adult head voxel model and experimental B_1^+ efficiency map.	64
Figure 11: a) B_1^+ efficiency maps of individual channels measured in the phantom at the largest and smallest size of the receive coil, with and without probes, and b) B_1^+ efficiency and phase	

maps of individual channels measured in vivo, performed at the largest size of the receive former.	65
Figure 12: Tx coil scattering matrix (S-matrix) parameters and table of summarized key results. Difference maps for each coil configuration were calculated from S-parameters measured directly before and directly after probe integration.	66
Figure 13: Noise correlation matrices for the Rx coil array with the former at its largest and smallest size, with and without NMR field probes.	68
Figure 14: SNR measured in the phantom: a) average central SNR throughout the sensitive region of the coil, b) average peripheral SNR throughout the sensitive region of the coil, c) average central and peripheral SNR over the whole sensitive region of the coil, d) regions of interest (ROIs) used to calculate peripheral (1) and central (2) SNR, and e) SNR map of a representative slice of the phantom.	69
Figure 15: In vivo SNR maps: a) comparison of normalized SNR between the commercial Nova coil (top) and the pediatric coil (bottom), b) B_1^+ normalized in vivo SNR map generated using the pediatric coil, and c) ROIs used to calculate peripheral (1) and central (2) SNR.	71
Figure 16: Magnitude free induction decay signals measured on the Skope scaffold, large coil configuration and small coil configuration using Skope probes 1-16 (starting left to right, top-down).	72
Figure 17: 2D EPI phantom images reconstructed without (original) and with (Skope corrected) dynamic field correction. Red arrows indicate visually apparent distortions.	73
Figure 18: In vivo 2D spoiled GRE image of an adult human taken with the pediatric coil adjusted to its maximum size (left) and the Nova coil (right).	74
Figure 19: Transmit coil configurations evaluated for potential use with the size-adaptive pediatric head coil: a) eight-channel dipole pTx coil, b) eight-channel loop pTx coil, c) top view of eight-channel Rx coil used in comparing the dipole and loop pTx coils, and d) bottom view of eight-channel Rx coil, demonstrating loop element circuitry.	81
Figure 20: In vivo MPRAGE image of adult human taken with the pediatric coil adjusted to its maximum size (left) and the commercial Nova coil (right) showing axial, coronal and sagittal planes.	88
Figure 21: Testing setup used to optimize performance of individual Rx array elements. Since cabling from each component of the Rx former was fed to a single mechanical structure housing the preamplifiers at the top of the coil, optimization of elements required some disassembly of the adjustable pieces. Future designs are seeking to improve the stability of electrical and mechanical components of the size adjustable array design.	90
Figure 22: Updated former design with receive coil housing and base in gray and transmit coil housing in white: a) top view of coil with Tx and Rx coil in position for imaging, b) top view with Tx coil removed, c) top view with Rx and Tx coil removed to enable easy positioning of subject,	

d) isometric view with Tx and Rx coils in position for imaging, and e) isometric view with Tx and Rx coils removed for easy positioning of the subject.98

Figure 23: Updated pediatric receive coil housing: a) view of anterior component of the receive coil former, b) view of anterior component of the receive coil former showing cavity for housing preamplifiers, and c) anterior component of the receive coil former separated from the full 32-channel phased array, showing cavity for housing preamplifiers.....99

Figure 24: View of updated pediatric coil at a) the smallest size of the receive coil housing and b) the largest size of the receive coil housing. 100

List of Tables

Table 1: Whole body, Partial body and local SAR limits for the three different operating modes as listed by the IEC and ICNIRP (*IEC limit is 3.2 Wkg^{-1}).....	24
Table 2: Temperature rise limits at each of the three operating modes as listed by the IEC and ICNIRP.....	25
Table 3: Summary of Tx scattering parameter results.	84
Table 4: Channel combinations with noise correlations above 50%. Worst case, maximum noise correlations for each coil configuration are listed in red, and channel combinations with higher than 60% noise correlation are listed in yellow.....	85
Table 5: Mean central and peripheral SNR generated from root sum-of-squares covariance weighted reconstruction of GRE images of a $\text{NiSO}_4 \times 6\text{H}_2\text{O}$ doped water phantom.....	86

List of Abbreviations

BC	Birdcage Coil
CP	Circularly Polarized
dB	Decibel
DW	Diffusion Weighted
DWI	Diffusion Weighted Imaging
ECC	Eddy Current Correction
EM	Electromagnetic
emf	Electromotive Force
FEM	Finite Element Method
FID	Free Induction Decay
FIT	Finite Integration Method
FOV	Field of View
GRE	Gradient Echo
ICNIRP	International Commission on Non-Ionizing Radiation Protection
IEC	International Electrotechnical Commission
ISMIRM	International Society for Magnetic Resonance in Medicine
MoM	Method of Moments
MR	Magnetic Resonance
MRI	Magnetic Resonance Imaging
MS	Multiple Sclerosis
NMR	Nuclear Magnetic Resonance
OFC	Occipitofrontal Circumference
PEC	Perfect Electrical Conductor
PI	Proportional Integral
pTx	Parallel Transmit
RF	Radiofrequency
RFC	Radiofrequency Choke
RMS	Root Mean Square

ROI	Region of Interest
RSS-COV	Covariance Weighted Root Sum-of-Squares
Rx	Receive
SAR	Specific Absorption Rate
SMS	Simultaneous Multi-Slice
SNR	Signal-to-Noise Ratio
sTx	Single Transmit
T	Tesla
TEM	Transverse Electromagnetic
Tx	Transmit
UHF	Ultra-High Field
VNA	Vector Network Analyzer
VOP	Virtual Observation Point

Chapter 1 – Introduction

Magnetic Resonance Imaging (MRI) is a mainstay of modern medical science, both in the clinic and in the laboratory. In the clinic, MRI serves as a powerful tool for diagnosing and grading pathologies across a wide range of anatomical structures. In the lab, the excellent soft tissue contrast and versatility of MRI provides researchers with numerous means of studying the structure, function and composition of the human (and non-human) body. Some of the most appealing features of MRI are that it achieves all of this non-invasively, and without the use of ionizing radiation. This makes MRI well-suited for long-term studies of neurodevelopment, and, particularly, neuroimaging of pediatric subjects.

As a result of its extensive use, MRI has seen rapid and consistent technological development since its clinical introduction in the mid 1980s. Much of this has focused on increasing the signal-to-noise ratio (SNR) of the acquired Nuclear Magnetic Resonance (NMR) signal.¹ One of the most important developments in this regard has been the introduction of MRI scanners with superconducting magnets capable of generating magnetic fields on the order of several Tesla (T). As SNR is linearly proportional to the strength of the magnetic field, these high field MRI systems offer much greater SNR compared to their low field counterparts.^{1,2} As a result of their improved performance, high-field MRI systems with field strengths of 1.5 and 3 T are now standard in both clinical care and in research.

The recent advent of ultra-high field (UHF) MRI systems with field strengths of 7 T and beyond represents a next step in the technological development of MRI. Such systems enable the visualization of the human brain with unprecedented spatial, spectral, and temporal resolution, and neuroimaging researchers have achieved a more precise understanding of human neurodevelopment and cognition as a result.^{1,3-5} UHF 7 T MRI has also improved the general understanding of numerous neurological disorders, including Alzheimer's disease,⁶⁻⁸ multiple sclerosis (MS),^{9,10} epilepsy,¹¹⁻¹³ Parkinson's disease,¹⁴⁻¹⁶ and cerebrovascular disease.¹⁷ Apart from the increase in imaging performance, another advantage of 7 T MRI is that it offers the potential to acquire images with comparable quality to conventional MRI scanners, but with much shorter scan times.^{1,18} This makes 7 T MRI particularly useful for performing neuroimaging

experiments of pediatric subjects, who are more prone to motion during MR imaging experiments.^{2,19-21} Furthermore, as the pediatric brain and its accompanying anatomical structures are typically smaller than those of adults, pediatric neuroimaging research stands to benefit from the improved resolution of UHF 7 T MRI.²²

Despite the suitability of MRI for imaging pediatric subjects, especially at UHF, there remain a number of challenges to pediatric MRI at both UHF and as a whole.^{2,21} One of the biggest challenges in pediatric neuroimaging is ensuring that the subject remains motionless throughout the duration of the scan. Since pediatric MRI scans can often last between fifteen minutes and an hour, this poses considerable challenge.²⁰ Historically, motion in pediatric neuroimaging has been addressed using sedation and general anesthetic. Sedation methods are still used in clinical practice, but present additional risks to the subject.^{2,19-21} Subject motion can also be mitigated by performing scans while the subject is sleeping, though the subject may still move or wake-up during the scan. Other methods of reducing subject motion involve taking measures to reduce the level of noise generated during the scan, implementing practice sessions with an MRI simulator environment, and or breaking-up the duration of the scan into more manageable segments.^{2,19-21} However, all of these techniques require additional time and expertise. In contrast to the above techniques, which focus on restricting subject motion, other, more advanced techniques seek to compensate for it. This can be done in a multitude of different ways. For example, it is possible to apply MRI pulse sequences that are less sensitive to motion or track/correct for motion using the MRI signal. This can be done either during or after the scan.²³ The overall likelihood of subject motion is also decreased with shorter scan times,¹⁹ highlighting the benefit of higher achievable acceleration with pediatric imaging at UHF.

A second challenge of pediatric neuroimaging stems from variations in the size of neuroanatomical structures at different stages of neurodevelopment.² Head size, measured as occipitofrontal circumference (OFC), increases rapidly in the early years of life and continues to increase into adolescence.²⁴ As such, attempts to image a significant range of pediatric head sizes using a single radiofrequency (RF) head coil designed for adult neuroimaging often are impacted by alterations in coupling of tissue and coil elements. The result is an overall reduction in SNR. The problem is typically addressed by developing RF head coils that are optimized for pediatric subjects. Pediatric coils can be optimized both in terms of size and shape. Due to the variability in head size across

the pediatric population, this is often accomplished using multiple separate RF head coils corresponding to subsets of the pediatric population,²⁵ or by developing size-adjustable RF coils capable of adapting to a range of head sizes.^{26–28} Such head coil designs also typically assist in reducing head motion, as the dimensions of the RF coil better conform to the dimensions of the subject's head and better restrict its movement.^{25–28}

Despite its many advantages, UHF 7 T MRI provides its own challenges, some of which are more severe for imaging pediatric populations. For instance, field inhomogeneities typically become more severe as field strength increases. This leads to an increased prevalence of imaging artifacts and geometric distortions.^{29,30} The reduced wavelength of the RF excitation field at 7 T compared to lower field strengths also results in inhomogeneity of signal intensity throughout the brain. This problem may be addressed by implementing a separate transmit coil with multiple individual transmit elements operating together to mitigate the inhomogeneity of the excitation field (this is known as parallel transmission or pTx).³¹ Last, the increase in magnetic field is associated with an increase in specific absorption rate (SAR), a measure of the amount of energy deposited in the tissue of the subject.³² In terms of overall MRI safety, SAR is of particular interest at 7 T, as electric fields can result in tissue heating, particularly in pediatric subjects.^{22,33} As a result of SAR consideration and the above challenges to UHF pediatric neuroimaging, to the knowledge of the authors, there are currently no commercially available pediatric head coils for subjects below 30 kg at 7 T MRI.

The objective of this thesis was to design and build a size-adaptive RF head coil with integrated magnetic field monitoring capability for whole brain pediatric MRI at 7 T. Chapter 2 provides an overview of relevant background information regarding MRI physics. Chapter 3 focuses on background information pertaining to the principles of RF coil design, as well as current research being undertaken in the design of size-adaptive RF coils. Chapter 4 then introduces the principles of NMR field probe operation, including a description of current research in integrated magnetic field monitoring using NMR field probes. Chapter 5 is written in manuscript format and presents the bulk of the work undertaken during this thesis including a description of the methods undertaken to design and build the proposed coil and gather the presented results. Chapter 5 also serves to present these results, along with a brief discussion of their significance. A more thorough discussion, in the broader context of the field of pediatric MRI, is presented in Chapter 6. This

includes limitations and future directions for the present work. Additional information pertaining to the design of the coil is contained in the Appendix.

Chapter 2 – Principles of Magnetic Resonance Imaging

2.1 NMR Principles

Magnetic resonance imaging (MRI) is based on the principles of Nuclear Magnetic Resonance (NMR), which relies on a quantum property called spin, a form of angular momentum intrinsic to elementary particles. In MRI, it is the intrinsic angular momentum and charge of atomic nuclei, composite particles composed of neutrons and protons, which is relied upon to generate the MR signal. Nuclei possessing an odd atomic number or odd mass number exhibit non-zero intrinsic angular momentum and are said to be NMR-active. Nuclei with zero angular momentum are said to be NMR-inactive.³⁴⁻³⁶ It is these MRI-active nuclei which are of relevance to MRI. Though not entirely accurate, it can be helpful to imagine the source of angular momentum of these nuclei to be modeled as physical rotation around an axis, similar to the motion of a gyroscope. In such a physically rotating system, the circulation of the positive charge of the protons about the axis of rotation generates a small current loop. This current loop, in turn, generates a small magnetic dipole moment that is similar to the magnetic field produced by a bar magnet. The generated magnetic moment (μ) is proportional to the angular momentum of the nucleus (J), related by a constant known as the gyromagnetic ratio (γ), which is given in units of frequency per unit magnetic field strength.³⁴⁻³⁶

(2.1)

$$\mu = \gamma J$$

When placed in an external magnetic field (B_0), the dipole moment aligns in a specific orientation with B_0 .³⁴⁻³⁶ Conventionally, B_0 is chosen to lie along the z-axis, such that

(2.2)

$$\vec{B}_0 = B_0 \hat{z}$$

The interaction between the magnetic dipole moment and the external magnetic field produces a torque, given by the cross product of the magnetic moment and the external magnetic field.

(2.3)

$$\tau = \mu \times B_0$$

Due to the relationship between torque and angular momentum, specifically

(2.4)

$$\tau = \frac{dJ}{dt}$$

the torque will generate precession, which can be modelled by the equation of motion given by

(2.5)

$$\frac{dJ}{dt} = \mu \times B_0$$

and rewritten as the differential equation

(2.6)

$$\frac{d\mu}{dt} = \gamma(\mu \times B_0)$$

The solution to this differential equation yields a magnetic moment vector which rotates about B_0 at a frequency given by:³⁴⁻³⁶

(2.7)

$$\omega_0 = \gamma B_0$$

This is known as the Larmor equation. ω_0 is known as the Larmor frequency. The gyromagnetic ratio of a given nuclear species is unique, and as such, so is the precession frequency of the nucleus at a given magnetic field strength. The gyromagnetic ratio of a hydrogen nucleus is 42.58 MHz/T,³⁶ meaning that the ^1H nucleus will precess at a frequency of around 300 MHz in a 7 Tesla Magnetic field.

2.2 Spin Systems and Bulk Magnetization

The previous section dealt with a single nucleus (also called a “spin”), but in reality, MRI generates measurements of systems of nuclei. The dipole moment of a spin will align itself in some orientation with the main magnetic field. The overall number of orientations and the specific orientation chosen by an individual nucleus depends on the spin quantum number and spin energy state of the nucleus in question.³⁵ The overwhelming majority of nuclei relevant to MRI have a spin quantum number of $\frac{1}{2}$ and are called spin $\frac{1}{2}$ systems. Such systems at equilibrium have two possible orientations: either parallel (the lower energy state) or anti-parallel (the higher energy state) to the external magnetic field. Generally, there is a very slight excess of spins in the lower energy state (i.e., aligned with the external field), governed by the equation:³⁵

(2.8)

$$\text{spin excess} \cong N \frac{\hbar\omega_0}{2kT}$$

Where N is the total number of spins (i.e., nuclei), \hbar is the reduced Planck’s constant, ω_0 is the Larmor frequency of the nucleus, k is the Boltzmann constant and T is the temperature of the sample. At room temperature and conventional MRI field strengths, the spin excess is only a few nuclei in a million. However, given the size of the samples measured in MRI and NMR, the total number of excess spins in the lower energy state can be quite high, generating a substantial longitudinal equilibrium magnetization M_0 , given by the equation:^{35,36}

(2.9)

$$M_0 = \frac{\rho_0\gamma^2\hbar^2}{4kT} B_0$$

2.3 The Rotating Reference Frame

In the field of MRI it is conventional to specify two different reference frames that describe spin precession.^{34–36} The first is known as the “laboratory reference frame”. In cartesian coordinates, this frame is defined by the axes $(\hat{x}, \hat{y}, \hat{z})$. The second frame, known as the “rotating reference frame”, is a frame rotating at the Larmor frequency. In cartesian coordinates, the rotating frame is described by the following amended axes:³⁶

(2.10)

$$\hat{x}' = \cos(\omega_0 t) \hat{x} - \sin(\omega_0 t) \hat{y}$$

$$\hat{y}' = \cos(\omega_0 t) \hat{x} + \sin(\omega_0 t) \hat{y}$$

$$\hat{z} = \hat{z}'$$

This frame is used especially when discussing nuclear precession as it greatly simplifies the mathematical analysis.

2.4 Generating the MR Signal

In order to generate an MR signal, the bulk longitudinal magnetization of a system of NMR-active nuclei must be excited out of equilibrium, into the plane orthogonal to the static magnetic field B_0 (i.e., into the transverse x-y plane). This excitation is generally accomplished with the use of a RF “transmit” coil. The coil is an antenna tuned to the specific Larmor frequency of the nuclei under observation.^{34–36}

To perform RF excitation, the transmit RF coil typically is applied to generate a linearly, or circularly polarized magnetic field (B_1). The B_1 field is applied perpendicular to the direction of B_0 and oscillates at the Larmor frequency. It can be modelled mathematically as follows.^{36–39}

(2.11)

$$\vec{B}_1 = B_1 \cos(\omega t) \hat{x}$$

B_1 is the magnitude of the transmit field and ω is the Larmor frequency (note that the direction of oscillation along the x-axis was chosen arbitrarily; any direction orthogonal to the z-axis would result in the same effect). This linearly polarized field can be further separated into two, counter-rotating circularly polarized magnetic fields.

(2.12)

$$B_{CW} = \frac{B_1}{2} (\cos(\omega t) \hat{x} - \sin(\omega t) \hat{y})$$

$$B_{CCW} = \frac{B_1}{2} (\cos(\omega t) \hat{x} + \sin(\omega t) \hat{y})$$

Where B_{CW} and B_{CCW} represent the clockwise and counterclockwise rotating fields, respectively. Only the component rotating in the same direction as the nuclear spin precession (i.e., the clockwise B_{CW} component) is significant in exciting the magnetization into the transverse plane.^{34,36-38} This component is known as the B_1^+ field. Purely circularly polarized B_1 fields are more efficient, requiring half the energy of a linear pulse to produce the same spin excitation.

In general, the transmit field is only applied for as long as is required for the magnetization to reach a specific “flip angle” (i.e., the angle made between the z-axis and the magnetization after excitation). Such a circularly polarized B_1^+ pulse can be modelled as a complex, time varying function in the transverse plane with an envelope specifying the duration and shape of the pulse.³⁶

(2.13)

$$B_1^+(t) = B_1^e(t)e^{-j(\omega_0 t - \phi)}$$

In this function, $B_1^e(t)$ represents the envelope function and ϕ represents the initial phase of the transmit field. This pulse can be greatly simplified by analysing it in the rotating frame and assuming that the pulse has zero phase offset, such that³⁶

(2.14)

$$B_1^+(t) = B_1^e(t)$$

As mentioned above, the final flip angle (α) of the magnetization vector depends on the duration (τ_p) and amplitude of $B_1^+(t)$, and is defined as:³⁶

(2.15)

$$\alpha = \gamma \int_0^{\tau_p} B_1^e(t) dt$$

Once “tipped” out of alignment, the spin system begins to precess about the axis of the external magnetic field. This precession can be detected using an RF “receive” coil. The transmit (Tx) and receive (Rx) coils can either comprise the same antenna (i.e., a Tx/Rx coil) or can be wholly separate networks. In either case, the Tx and Rx coils must be tuned to the specific Larmor frequency of the nuclei under observation. This makes it possible to a) effectively excite the spins

into the transverse plane and b) sensitively measure the MR signal at the Larmor frequency.^{34,36-38,40} Once excited, the precessing spins will eventually return to their equilibrium state, aligned with the external magnetic field along the z-axis.

2.5 Relaxation

The process of returning to equilibrium is called longitudinal, or “spin-lattice” relaxation. The longitudinal relaxation time, that is, the time required for the bulk magnetization to return to its longitudinal equilibrium state after excitation, is known as T_1 .³⁴⁻³⁶

A second kind of relaxation, known as transverse or “spin-spin” relaxation and governed by the time constant T_2 is concerned with the decay of the transverse component of the magnetization vector. It is, in fact, a combination of longitudinal relaxation and the dephasing of the precessing spins which leads to the loss of the transverse magnetization (generally before the magnetization vector returns to equilibrium - i.e., $T_2 < T_1$).³⁴⁻³⁶ When the magnetization vector is initially tipped into the x-y plane, the transverse magnetization is generated by a system of coherently precessing spins. Because these spins are precessing in-phase, they generate an appreciable transverse magnetization. Over time, this coherent precession is lost as spins come out of phase, leading to an exponential decay of the transverse magnetization. This loss of coherence is a result of many different factors, most notably interactions between individual spins (hence the name “spin-spin” relaxation) and changes in the local magnetic field caused by differences in the chemical environment within a given sample. As a result, the transverse relaxation time T_2 is a tissue dependent quantity.³⁶

In addition to the theoretical causes of spin dephasing listed above, there are also practical factors that accelerate spin dephasing and the decay of the transverse magnetization. These include hardware imperfections, such as inhomogeneities in the main magnetic field, as well as experimental factors such as susceptibility-induced magnetic field distortions caused by the presence of the sample in the magnetic field. As such, the apparent decay of the transverse magnetization in practice will occur much faster, by a time constant of T_2^* , than what is theoretically predicted by T_2 (i.e., $T_2^* < T_2$).³⁶

2.6 The Bloch Equations

The evolution of the magnetization vector over time after RF excitation can be modelled using the Bloch equations. The total magnetization vector is divided into longitudinal (M_z) and transverse (M_{xy}) components, with M_{xy} given by:³⁴⁻³⁶

(2.16)

$$M_{xy} = M_x(t) + jM_y(t)$$

After excitation, the Bloch equation for the longitudinal magnetization vector is given by:³⁴⁻³⁶

(2.17)

$$M_z(t) = M_0 \left(1 - e^{-\frac{t}{T_1}}\right) + M_0 \cos(\alpha) e^{-\frac{t}{T_1}}$$

Where M_0 is the equilibrium longitudinal magnetization, t is the time, and α is the flip angle. The Bloch equation for the transverse magnetization is given by:³⁴⁻³⁶

(2.18)

$$M_{xy}(t) = M_0 \sin(\alpha) e^{-j(2\pi f_0 t - \phi)} e^{-\frac{t}{T_2}}$$

Where f_0 is the Larmor precession frequency and ϕ is the phase of the precessing magnetization.

2.7 Detecting the MR Signal

The MR signal is generated from the precession of the transverse magnetization. This is measured via Faraday induction in the Rx coil. To illustrate this process, consider a system of spins placed in an external static magnetic field and having been excited 90° into the transverse plane such that $M_z(t = 0) = 0$ and $M_{xy}(t = 0) = M_0$. As the spin system returns to equilibrium aligned with the static magnetic field, the transverse magnetization will precess about the static magnetic field and decay according to the Bloch equations. This precessing magnetization will generate a current in any nearby conductive receive loop in accordance with Faraday's law of induction.³⁴⁻³⁶ The

voltage measured at the terminals of this receive loop is then amplified and digitized, yielding the MR signal used to generate an image.

2.8 Spatial Encoding: from a 1D signal to a 2D image

The Rx coil measures a one-dimensional, time-based signal, called the free-induction decay (FID) of the transverse magnetization. This “bulk” signal is generated by all the precessing spins in the sensitive region of the receive coil.^{35,36} In order to use this signal to generate a two-dimensional image, the signal from individual spins must be localized and “binned” into discrete voxels (i.e., pixels). To accomplish this, the MRI system leverages a technique known as “spatial encoding”. Spatial encoding is a method by which the frequency and phase of a system of spins is made spatially dependent using a combination of linearly varying magnetic fields, called “gradients”. These linearly varying magnetic fields are generated by a set gradient coils.³⁴⁻³⁶ In general, there are three such gradient coils, G_x , G_y , and G_z , each producing a linearly varying magnetic field along one of the cartesian axes of the scanner (x,y, and z). When active, the gradient fields produced by these coils combine with the static magnetic field B_0 , such that the total field at a given position in the scanner bore is given by³⁶

(2.19)

$$\vec{B} = (B_0 + G_x x + G_y y + G_z z)\hat{z}$$

Where G_x , G_y , and G_z represent the strength of each of the gradient fields, generally in mT/m. The effect of these additional fields is to add spatial dependence to the local precession frequency, according to the Larmor equation.

(2.20)

$$\omega(x, y, z) = \gamma(B_0 + G_x x + G_y y + G_z z)$$

To illustrate how spatially dependent precession frequency can be used to generate a 2D image, consider the acquisition of an axial image. That is, in the case of a standard MR imaging experiment with the subject lying on the scanner bed in a supine position, an image in the x-y plane. In this orientation, the G_z coil produces a gradient that is linearly varying and impacting the precession frequency along the length of the bore. A specific “slab” of spins can now be excited

along the z-axis by applying an excitation RF pulse with a specific center frequency ($\bar{\omega}$) and bandwidth ($\Delta\omega$).^{34,36} The centre position of the slab along the z-axis (\bar{z}) and the thickness of the slab (Δz) are related to the center frequency and bandwidth of the excitation pulse by the following equations:^{34,36}

(2.21)

$$\Delta z = \frac{\Delta\omega}{\gamma G_z}$$

$$\bar{z} = \frac{\bar{\omega} - \omega_0}{\gamma G_z}$$

With a given slab or slice selected along the z-axis, the x and y gradients can now be used to spatially encode along the x and y axes. This is commonly achieved by using the G_x gradient to perform frequency encoding and the G_y gradient to perform phase encoding. In frequency encoding, the G_x gradient is applied during data acquisition (also known as “readout”), resulting in a linear variation in the precession frequency of spins along the x-axis given by the equation^{34,36}

(2.22)

$$\omega(x) = \gamma(B_0 + G_x x)$$

In phase encoding, the G_y gradient is applied for a period of time prior to data acquisition and then turned off. During the period over which the gradient is applied, spins along the y axis will accrue a position dependent phase offsets given by (assuming a rectangular gradient pulse)^{34,36}

(2.23)

$$\phi_y(y) = -\gamma G_y T_p y$$

where $\phi_y(y)$ is the accrued phase and T_p is the time over which the pulse is applied. The result is an image of a specific slab along the z-axis with voxel locations identified by a specific frequency and phase offset.

The choice of which gradient performs the duty of slice selection, frequency encoding and phase encoding is varied depending on the orientation of the image. A pulse sequence is used to describe

the specific duration, timing and amplitude of the RF pulses and gradient fields. These sequences can be optimized for different imaging applications.

The signal recorded by a receive coil in an MR imaging experiment is a 1D time domain signal containing the spatial phase and frequency data encoded by the gradient coils. As such, the 2D data acquired during MR imaging is in Fourier space (or k-space) as opposed to image space. In order to perform image reconstruction, this Fourier space data must be converted to image space using an inverse discrete Fourier transform.³⁶

Chapter 3 – Principles of RF Coil Design

3.1 Fundamental Principles of RF Coils

RF coils are near-field antennae, electric circuits designed to convert electric currents into electromagnetic fields and vice-versa.^{38,40} As mentioned previously, RF coils serve two overall functions: transmit (Tx) and receive (Rx). The role of the Tx coil is to efficiently convert a specialized, high-power electrical signal into a homogenous B_1^+ magnetic field, in order to excite spins into the transverse plane. The role of the Rx coil is to efficiently and selectively detect the change in magnetic flux density generated by the precession of the magnetization vector and convert this into an electrical signal which, after digitization, can be interpreted by the console computer.⁴⁰ These two functionalities can be implemented using separate circuitry (i.e., one Rx coil and one Tx coil) or they can be combined into a single, transceiver coil. This section will describe the fundamental principles governing RF coil operation and design.

3.1.1 Transmit Coil: Principles of Operation

As discussed above, the role of the transmit coil is to excite the bulk magnetization of the spin system. In order to accomplish this, the transmit coil produces a circularly polarized magnetic field, known as the B_1^+ field, which rotates at the Larmor frequency of the nuclei under observation. This field is described in the rotating reference frame by³⁶

(3.1)

$$B_1^+(t) = B_1^e(t)$$

Equation 3.2 can be used to understand the effects of this pulse on the bulk magnetization.³⁴

(3.2)

$$\frac{dM}{dt} = \gamma(M \times B)$$

Where B represents the total magnetic field and is given by

(3.3)

$$B = B_0 \hat{z} + B_1^e(t) \hat{x}'$$

In the rotating reference frame. The left side of equation 3.2 can be rewritten as

(3.4)

$$\frac{dM}{dt} = \frac{d}{dt} (M_{x'} \hat{x}' + M_{y'} \hat{y}' + M_{z'} \hat{z}')$$

Since \hat{x}' and \hat{y}' are both functions of time described by equation 2.10, the product rule must be used to evaluate this derivative, yielding:³⁴

(3.5)

$$\frac{dM}{dt} = M_{x'} \frac{d\hat{x}'}{dt} + M_{y'} \frac{d\hat{y}'}{dt} + \frac{dM_{x'}}{dt} \hat{x}' + \frac{dM_{y'}}{dt} \hat{y}' + \frac{dM_{z'}}{dt} \hat{z}'$$

The solutions to $\frac{d\hat{x}'}{dt}$ and $\frac{d\hat{y}'}{dt}$ are:

(3.6)

$$\frac{d\hat{x}'}{dt} = -\omega_0 \hat{x}'$$

and

(3.7)

$$\frac{d\hat{y}'}{dt} = -\omega_0 \hat{y}'$$

Respectively, where ω_0 is the Larmor frequency and frequency of rotation of the rotating reference frame. Using this solution, equation 3.5 can be rewritten:

(3.8)

$$\frac{dM}{dt} = -\omega_0 (M_{x'} \hat{x}' + M_{y'} \hat{y}') + \frac{dM_{x'}}{dt} \hat{x}' + \frac{dM_{y'}}{dt} \hat{y}' + \frac{dM_{z'}}{dt} \hat{z}'$$

Which can further be rewritten as³⁴

(3.9)

$$\frac{dM}{dt} = -\omega_0 \hat{z}' \times M + \frac{\partial M}{\partial t}$$

Where $\frac{\partial M}{\partial t}$ represents the time derivative of the bulk magnetization vector in the rotating reference frame. Substituting this definition for the left side of equation 3.2 gives

(3.10)

$$-\omega_0 \hat{z}' \times M + \frac{\partial M}{\partial t} = \gamma(M \times B)$$

Which can be rewritten in terms of the time derivative of magnetization in the rotating reference frame as

(3.11)

$$\frac{\partial M}{\partial t} = \gamma M \times \left(B - \frac{\omega_0}{\gamma} \hat{z}' \right)$$

As such, the effective magnetic field in the rotating reference frame is given by³⁴

(3.12)

$$B_{eff} = \left(B - \omega_0 \hat{z}' \right) = \left(B_0 - \frac{\omega_0}{\gamma} \right) \hat{z}' + B_1^e(t) \hat{x}'$$

Substituting in the Larmor equation for ω_0 causes the \hat{z}' component of B_{eff} to disappear, leaving

(3.13)

$$B_{eff} = B_1^e(t) \hat{x}'$$

The result is an effective magnetic field oriented in the transverse plane. Based on the same principles governing precession in the laboratory frame, this effective magnetic field will cause the magnetization vector M to precess about the \hat{x}' axis with a frequency given by³⁴

(3.14)

$$\omega_1 = \gamma B_1^e(t)$$

In this way, the magnetization vector can be rotated to any desired angle away from the static magnetic field, with the flip angle provided by equation 2.15. As can be seen from this equation, the time required to achieve a specific flip angle is governed by the magnitude and shape of the $B_1^e(t)$ pulse as well as the gyromagnetic ratio of the nucleus.³⁶

3.1.2 Receive Coil: Principles of Operation

Once flipped out of alignment with B_0 , the magnetization vector will precess at the Larmor frequency before returning to equilibrium. Receive coils are designed to sensitively detect the change in the magnetic flux density generated by the precessing magnetization via the induced electromotive force (emf). This effect is demonstrated in **Figure 1** below.

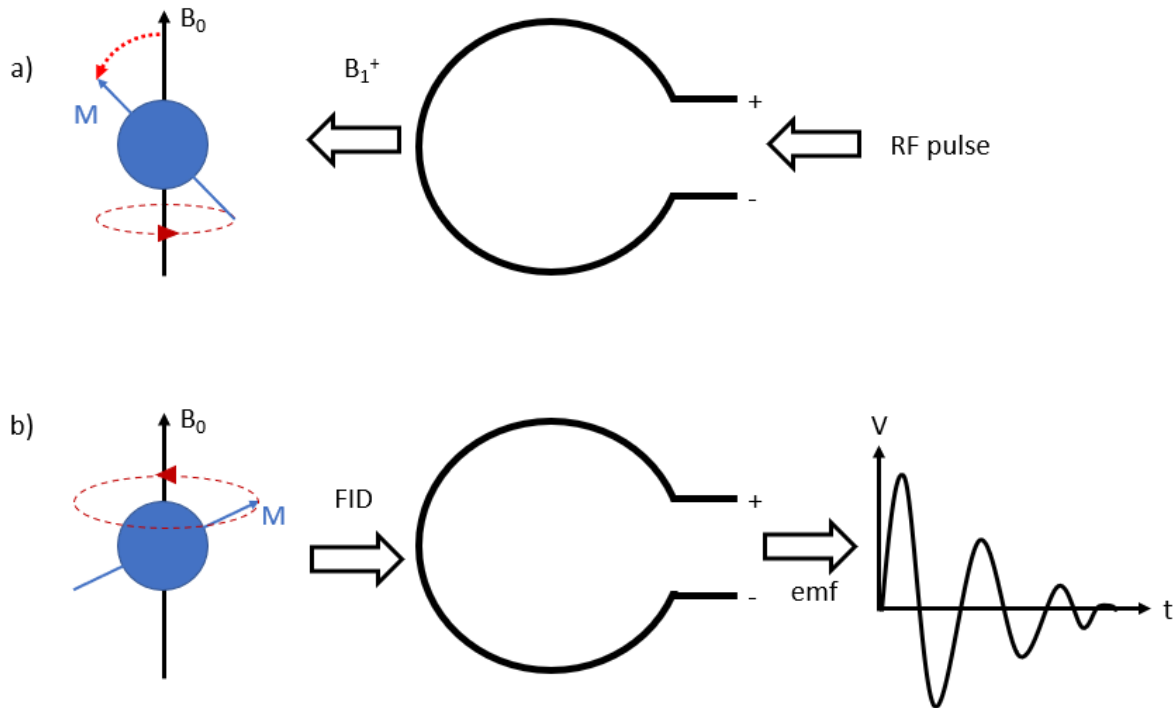


Figure 1: Function of a) transmit element and b) receive element.

A wire loop is placed near a sample immediately following the application of the transmit pulse such that the magnetization vector is precessing in the transverse plane. The magnetic flux through this loop of wire is described as:

(3.15)

$$\Phi_B = \int_S B \cdot dA$$

In which S represents the surface enclosed by the wire loop, B is the magnetic field and dA is an infinitesimal surface area.³⁵ The emf generated in the loop of wire is described as the change in magnetic flux over time.

(3.16)

$$\varepsilon = -\frac{d\Phi_B}{dt}$$

Since the precessing magnetization vector represents a time-varying magnetic field, an emf will be generated in the wire receive loop. This emf generates a voltage in the loop at the Larmor frequency, which is amplified by a low-noise preamplifier, converted to a digital signal, and processed to form the MR image.³⁵

3.2 RF Coil Classes

There are several different kinds of RF coil circuits. A detailed summary of all designs is beyond the scope of this thesis. This section will describe the two general classes of RF coils, namely, surface coils and volume coils.

3.2.1 Surface Coils

Surface coils are used extensively in human and animal MRI. They are generally designed to lie near or on the surface of the sample.^{37,38} They exist in a wide variety of shapes and sizes and can lay flat or conform to a given surface. Some common surface coil designs include circular or rectangular loops.^{37,38} Extensive application of surface coils in MRI is due to the fact that they exhibit improved sensitivity compared to volume coils, generally up to a distance of half their diameter/width.^{34,37-40} This makes them particularly well-suited for high SNR signal detection near the surface of the sample and for preclinical MRI of small animals. A disadvantage of surface coils

is that their limited field-of-view leads to a fairly inhomogeneous excitation field. As such, surface coils are most commonly used as receive-only elements, though transceiver and transmit surface coils do exist.^{37,38}

3.2.2 Surface Coil Arrays

Surface coils can be combined to form surface coil arrays, extending the field of view (FOV) of the coil over a larger region of interest (ROI) than could be viewed with a single surface coil.^{37,38,41} The main benefit of using a surface coil array (also known as a *phased array*), is that the improved local SNR provided by each surface coil is extended to cover the entire FOV covered by the array.^{37-39,41,42} Furthermore, the local sensitivity of each surface element provides additional spatial information in terms of the location of the detected MR signal. This leads to two additional benefits of phased arrays. First, this leads to an improvement in SNR at a greater depth than could be achieved with a single receive element, as the signal from individual receive elements can be combined with a weighting factor based on the position of the imaged voxel.⁴¹ Second, the additional spatial information can be used to reduce MR scan time by under sampling k-space in a technique known as parallel imaging.⁴³ This technique will be described in more detail in a later section.

The main challenge in designing an RF phased array is isolating individual receive elements. When surface coils are placed near one another, they will interact via inductive coupling.^{37,38,41} This is known as *mutual inductance* and is a result of the magnetic fields being produced in each element. Mutual inductance causes a resonance splitting in each of the surface coils, shifting the resonant frequency away from the Larmor frequency and reducing the overall sensitivity of each receive element (**Figure 2**).⁴¹

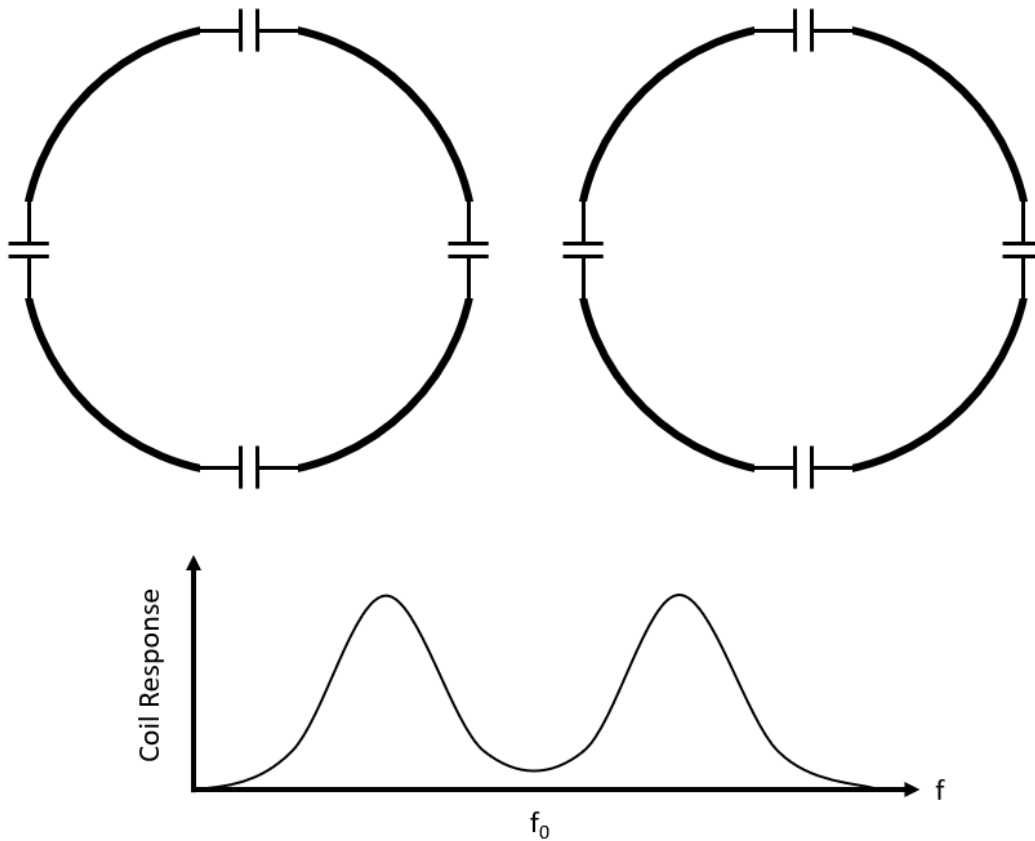


Figure 2: Resonance splitting at the Larmor frequency (f_0) because of coupling between two coil elements.

It also causes a transfer of signal and noise between elements, reducing SNR. Generally, there exist two methods for mitigating inductive coupling between elements in a phased array: a) geometric decoupling, which is used to eliminate coupling between adjacent elements, and b) preamplifier decoupling, which is relevant for reducing coupling between non-adjacent elements.^{37,38,41} These techniques will be described in detail in a later section.

3.2.3 Volume Coils

Volume coils are designed to fully (or partially) enclose the volume of interest, generating or receiving magnetic fields over a large ROI.^{37,38,40} These coils are typically used as transmit-only coils due to their ability to generate highly homogeneous B_1^+ excitation fields, but they are also often employed as transceiver coils. Their increased sensitivity over a large volume, but not necessarily to the sample, makes them less suitable as receive coils in terms of SNR compared

with surface coils or phased arrays.^{37,38,40} Common examples of volume coils include the birdcage coil (BC) and transverse electromagnetic (TEM) resonator.^{37,38} These cylindrical coils create a transverse excitation field by generating a circumferentially distributed sinusoidal current.^{34,37,38} The ability of the birdcage coil to generate a highly homogeneous B_1^+ field has made it one of the most common transmit coil designs at clinical strength MRI (1.5 T, 3 T) as well as at 7 T.³⁷

3.2.4 Volume Coils at UHF: Parallel Transmit Coils (pTx)

As the field strength of the MRI system increases, so does the Larmor frequency of the nuclei under observation. This poses an additional challenge at UHF, as the wavelength of the transmit field approaches the dimensions of human anatomical structures. In proton imaging experiments at 7 T this can lead to inhomogeneity in the RF excitation field.⁴⁴ One strategy to mitigate these effects is to implement a parallel transmit (pTx) coil design.⁴⁴ pTx coils are similar to surface coils in that they generally consist of multiple, individual transmit elements. However, rather than being used to sensitively detect the MR signal, the separate transmit elements are driven by high power amplifiers to generate an excitation field.⁴⁴ The field from each of the transmit elements in a pTx coil can be combined to form the circularly polarized B_1^+ field. The added benefit of a pTx coil compared to a single channel (commonly referred to as sTx) transmit volume coil is that the transmit field produced by each element can be modified in a process called *B₁ shimming*, to compensate for inhomogeneities or other field effects.⁴⁴ This makes pTx coils a powerful tool for UHF imaging. The main disadvantage of pTx coils is the added complexity that arises with multiple, individual transmit elements. For instance, the magnitude and phase of the excitation pulse of each transmit element must be optimized to generate the desired circularly polarized B_1^+ excitation field (termed the CP^+ mode of the coil).⁴⁴ Furthermore, the SAR profile of the combined coil will vary depending on the chosen magnitudes and phases of each element. As such, a more rigorous approach to managing SAR must be undertaken.⁴⁵

3.3 Coil Safety Considerations: SAR

The primary safety concern in the design of RF coils for MRI is tissue heating induced by the electric field component of the transmit electromagnetic field.³² Specific Absorption Rate (SAR) is a measure of the mean power deposited per kilogram in the imaged body area by this process.^{32,38}

Though not equivalent to an exact temperature increase, SAR is used by regulatory bodies to set safe acceptable limits on MRI sequence and RF coil design.

3.3.1 Electric Fields in MRI: Conservative vs. Non-Conservative

Electric fields are an inherent part of MRI and pose a challenge to the safe operation of the MR scanner. This is because electric fields induce currents in conductive structures, such as metallic implants and salt-carrying tissues.³⁷ The induced currents can generate heat through ohmic losses, posing a potential threat to both subject and scanner. In general, there are two kinds of electric fields produced in an MR imaging experiment: non-conservative and conservative electric fields.³⁷ Non-conservative electric fields are those generated by the changing magnetic fields produced by the transmit coil. These fields are inherently coupled to the changing B_1^+ fields according to Maxwell's equations:

(3.17)

$$\nabla \times \vec{E} = -\frac{\partial \vec{B}}{\partial t}$$

Conservative electric fields are those generated by the large voltages present in the transmit coil. Mitigating these electric fields is an important part of RF transmit coil design.³⁷

3.3.2 Modelling SAR

SAR depends on the electric field and the conductivity of the imaged sample. As such, analytical models of SAR generally describe a local, peak, instantaneous value based on the peak amplitude of the B_1^+ field, B_p . One such method provides an approximation of SAR at the periphery of the body by modelling this part of the sample as a conductive loop of radius R .³²

(3.18)

$$SAR = \frac{\sigma}{2\rho} (\pi f B_p R)^2$$

Where σ is the conductivity of the tissue, ρ is the tissue density and f is the frequency of the B_1^+ pulse (i.e., the Larmor frequency). As the Larmor frequency is proportional to the strength of the external magnetic field, it can be seen from this model that SAR increases quadratically with field strength. An estimation of the rate at which a given sample will heat can be achieved by dividing SAR by the heat capacity of the sample.

Given the complexity of accurately modelling SAR analytically, the use of numerical methods is commonplace. Such methods allow for an analysis of SAR in complex, inhomogeneous geometries with spatially varying conductivity and permittivity, yielding highly accurate estimates of both local and average SAR.³² SAR can also be estimated using B_1^+ maps acquired on the scanner to approximate the electric field.

3.3.3 SAR Limits

SAR limits are set by the International Electrotechnical Commission (IEC) and International Commission on Non-Ionizing Radiation Protection (ICNIRP).⁴⁶ They provide limits based on three recognized operating modes: normal mode, controlled mode, and research/experimental mode. The normal mode of operation minimizes risks to the patient and is the most conservative of the three modes. Controlled mode allows for improved imaging performance at the cost of higher exposure to risk than normal mode. In this mode, the patient must be monitored throughout the scan. In research/experimental mode, exposure is only restricted to prevent harmful effects, and any scanning must be approved by a research ethics committee. As with controlled mode, the subject must be monitored throughout the scan. SAR limits and temperature rise limits from these organizations are given in **Table 1** and **Table 2** below.⁴⁶

*Table 1: Whole body, Partial body and local SAR limits for the three different operating modes as listed by the IEC and ICNIRP (*IEC limit is 3.2 W/kg⁻¹).*

Mode	Whole Body [W/kg]	Partial Body [W/kg]		Local [W/kg]		
		Head	Not Head	Head	Trunk	Extremities
Normal Mode	2	3*	2-10	10	10	20
Controlled Mode	4	3*	4-10	10	10	20
Research/Experimental Mode	>4	>3*	>(4-10)	10	>10	>20

Table 2: Temperature rise limits at each of the three operating modes as listed by the IEC and ICNIRP.

Mode	Temp [°C]
Normal Mode	0.5
Controlled Mode	1
Research/Experimental Mode	>1.0

3.4 RF Coil Design

Though RF coils come in a variety of shapes and sizes, they generally operate based on the same fundamental principles and, as such, are constrained by similar design objectives. For transmit, the main objective is to develop a coil that is capable of efficiently producing as homogeneous a B_1^+ excitation field as possible, while minimizing the electric field (i.e., SAR). For receive, the goal is to produce a coil that is capable of efficiently and sensitively measuring the FID of the nuclear magnetization while being insensitive to noise.^{37,38,40} Overall, it is important that both coils be safe and capable of integrating with one another. This section describes the general process of RF coil design, including how these objectives can be achieved for each coil.

3.4.1 Resonance

In order to function effectively, RF coils, both Tx and Rx, must operate at the resonant Larmor frequency of the nuclei under observation. This is generally accomplished by using an LC resonant circuit architecture, in which the resonant frequency (f_0) of the RF coil can be tuned by adjusting either the inductance (L) or the capacitance (C) of the circuit according to the equation⁴⁷

(3.19)

$$f_0 = \frac{1}{2\pi\sqrt{LC}}$$

Ensuring that both the receive and transmit coils are tuned to the Larmor frequency is important for the efficiency of the B_1^+ excitation and the sensitivity (and selectivity) of detection. An example of an LC circuit as a RF surface coil element is given in **Figure 3** below.

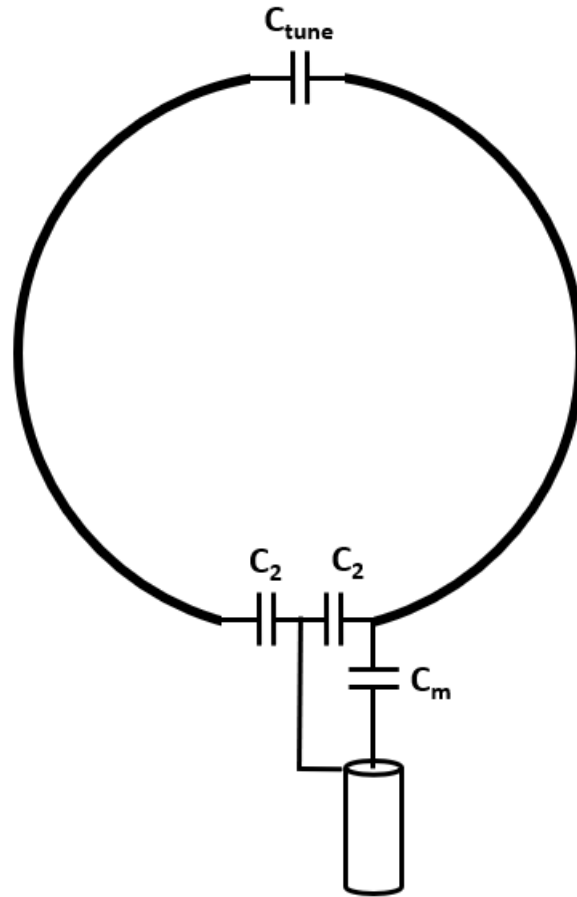


Figure 3: LC resonant loop with tuning capacitor (C_{tune}), matching capacitor (C_m), and capacitor C_2 (equal to $2 \times C_{tune}$).

Here, the inductance is provided by the self inductance of the conductive copper wire, and the capacitance is provided by the lumped element capacitors. Tuning is achieved by adjusting the value of the capacitor C_{tune} .

3.4.2 Impedance Matching

In mathematical terms, resonance in electrical circuits occurs when the imaginary component of the coil's impedance is zero.³⁷ Impedance (Z) is a complex, frequency-dependent resistance, and is an important quantity to consider when designing RF coils because it relates to the amount of power reflected at the circuit interface. The amount of reflected power at the interface between the cable and the coil is given by the reflection coefficient.³⁷

(3.20)

$$\Gamma = \frac{Z_{cable} - Z_{coil}}{Z_{cable} + Z_{coil}}$$

It can be seen from this equation that the reflection coefficient drops to zero when the cable and coil impedances are equal. As such, one of the goals of coil design is to ensure that there is an appropriate “impedance match” at the interface between the coil and the transmission lines, i.e., $Z_{cable} = Z_{coil}$.³⁷ This ensures that the maximum amount of power is transmitted across the coil/transmission line interface. Typical impedance values for transmission lines are 50 and 75 Ω . Impedance matching can be performed in several ways, namely capacitive impedance matching, inductive impedance matching and impedance matching using transmission line elements.³⁷ Only capacitive impedance matching will be explained here.

The impedance of a capacitor of value C is given below.³⁷

(3.21)

$$Z_c = -j \left(\frac{1}{\omega C} \right)$$

Here, j represents the imaginary number $\sqrt{-1}$, and ω represents frequency. In capacitive impedance matching, the coil is tuned to a slightly lower frequency than the Larmor frequency such that the real part of the impedance is equal to the impedance of the transmission line (i.e., 50 Ω). This satisfies the impedance matching criteria described by the reflection coefficient, but equivalently shifts the imaginary component away from the resonant frequency.³⁷ This shift is compensated by adding a capacitor in series with the RF coil. Capacitive impedance matching is shown in **Figure 3** for a representative surface coil element as the capacitor C_M .

3.4.3 Geometric Decoupling (Phased Arrays)

In phased arrays, individual elements must be isolated from one another to achieve optimal SNR.⁴¹ This typically means eliminating the inductive coupling between the individual elements in the array. One of the ways in which this is achieved is by overlapping adjacent loops such that their inductive coupling is cancelled. This technique is called geometric decoupling (**Figure 4**).³⁷

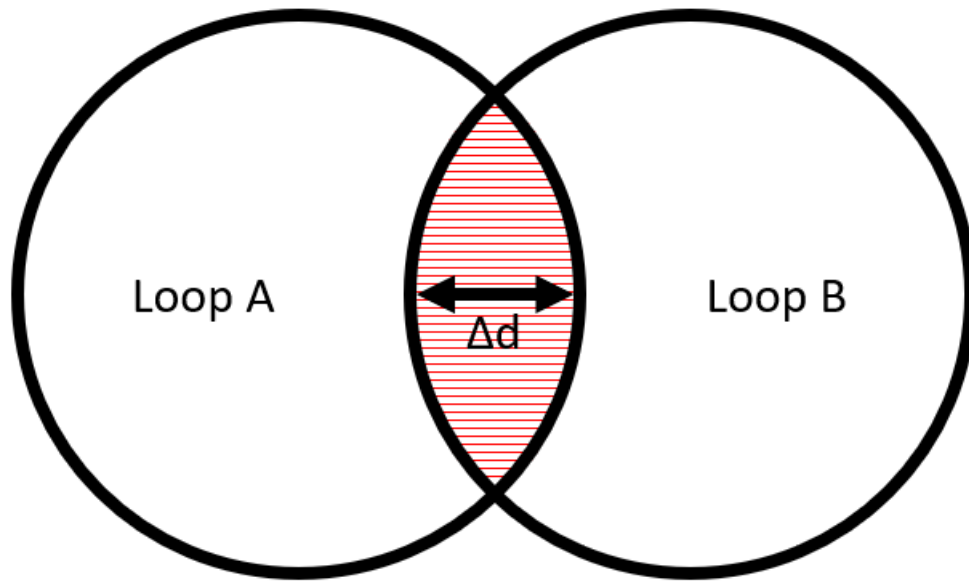


Figure 4: Two overlapped loop elements, with overlap shown in red.

As the distance between adjacent loops decreases (i.e., as Δd increases), there is a point at which the mutual inductance between the elements falls to zero. This is known as the critical overlap.³⁷

3.4.4 Coil Safety Features: Coil Detuning

One of the main safety concerns in RF coil design is the combination of a high power transmit coil near or often directly adjacent to a sensitive receive coil, both of which are tuned to the same Larmor frequency. Being designed to sensitively detect the MR signal, the receive coil is not equipped to handle the high power of the excitation field. This poses a risk to the MRI system hardware as well as to the patient, as high currents can be coupled into the receive coil, generating heat and increasing SAR beyond acceptable limits by focusing RF power.³⁷⁻³⁹ In order to mitigate these safety concerns, the RF coils must be alternatively detuned during the transmit and receive portions of the scan. It is important to note that this only applies to coils in which the transmit and receive coil are separate electrical systems; in transceiver coils, detuning is not required since the same antenna performs both functions, alternated using an electrical switch.³⁷⁻³⁹

There are generally two ways in which RF coils are detuned: active detuning, which requires an input current in order to function, and passive detuning, which does not require an input current

and is implemented as a back-up in case active detuning fails. Typically, active detuning is achieved with the use of a PIN diode. Active detuning is used in both transmit and receive coils, with the function of the PIN diode changing depending on the coil type. In transmit coils, forward biasing the PIN diode typically results in activation of the coil. In receive coils, forward biasing the PIN diode typically results in the coil being detuned.³⁷⁻³⁹ Passive detuning, which is reserved for receive coils, utilizes two PIN diodes in parallel, oriented opposite to one another (called a “cross diode”). The passive detuning circuit is activated when either of the PIN diodes in the cross diode are forward biased, detuning the coil when a threshold voltage is surpassed.⁴⁰

In transmit coils, the PIN diode alone is often sufficient to detune the coil, since the diode acts as an open circuit when it is not forward biased. In receive coils, active and passive detuning circuits are generally more complex, since the coil must be detuned when the diode is forward biased. Common methods of implementing active and passive detuning are shown in **Figure 5**.

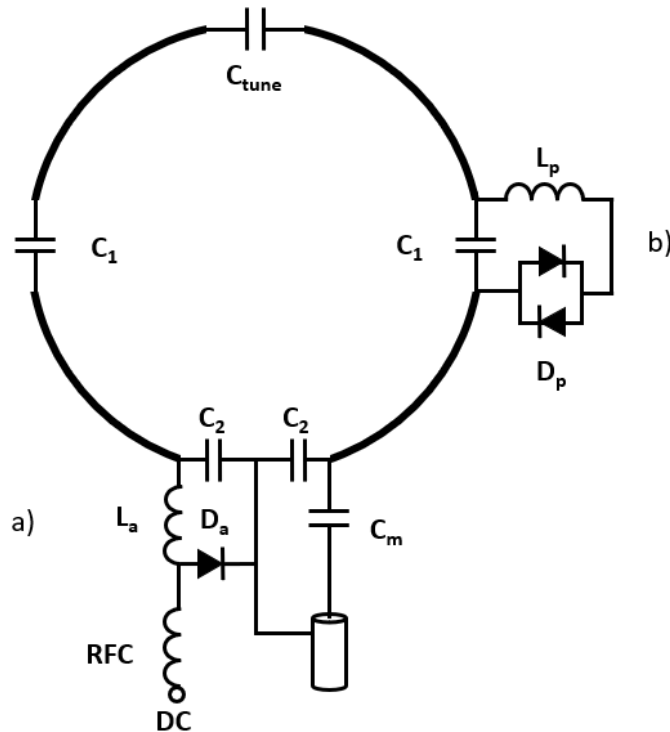


Figure 5: A receive loop with a) active detuning circuit, activated by forward biasing a PIN diode (D_a) with an external DC input isolated from RF current by an RF choke (RFC), and b) passive detuning circuit, activated when the cross diode (D_p) is forward biased by an excessive voltage across its terminals.

When forward biased, the PIN diode acts as a short circuit, introducing a parallel LC resonant circuit in series with the coil. If tuned correctly, this LC circuit has a high impedance at the Larmor frequency, effectively blocking currents at or near this frequency and detuning the loop.^{38,39} As an additional precaution, it is also possible to integrate a low-loss fuse into the receive coil. In the event of a failure in either the active or passive detuning circuits, the fuse will blow, opening the loop.³⁸

3.4.5 Eliminating Common-Mode Currents: Cable traps and Baluns

RF coils, whether transmit or receive, are typically connected to the MRI system via coaxial cables. These cables consist of an inner conductive wire (the “pin”) surrounded by an outer conductive shield (the “ground”), separated by an insulating material.³⁷ There are three ways in which currents can flow along these conductors: along the inner conductor, along the inner surface of the shield and along the outer surface of the shield. The currents flowing along the inner conductor and the inner surface of the shield are desirable, as they form the differential MR signal in the receive case or the excitation signal in the transmit case. The currents flowing along the outer surface of the shield, the *common-mode currents*, are undesirable as they generally consist of noise.³⁷ Cable traps and baluns are both techniques aimed at reducing common-mode currents. Only cable traps will be discussed here.

A cable trap is a circuit designed to present a very high impedance to common-mode currents and a very low impedance to the desired differential current. An example of a cable trap is shown in **Figure 6**. Here, the coaxial cable is wound to form an inductor. A capacitor is placed across the terminals of the inductor and connected to the outer surface of the coaxial cable shield. This forms an LC resonant circuit along the outer surface of the shield, presenting a very high impedance to the common mode currents.

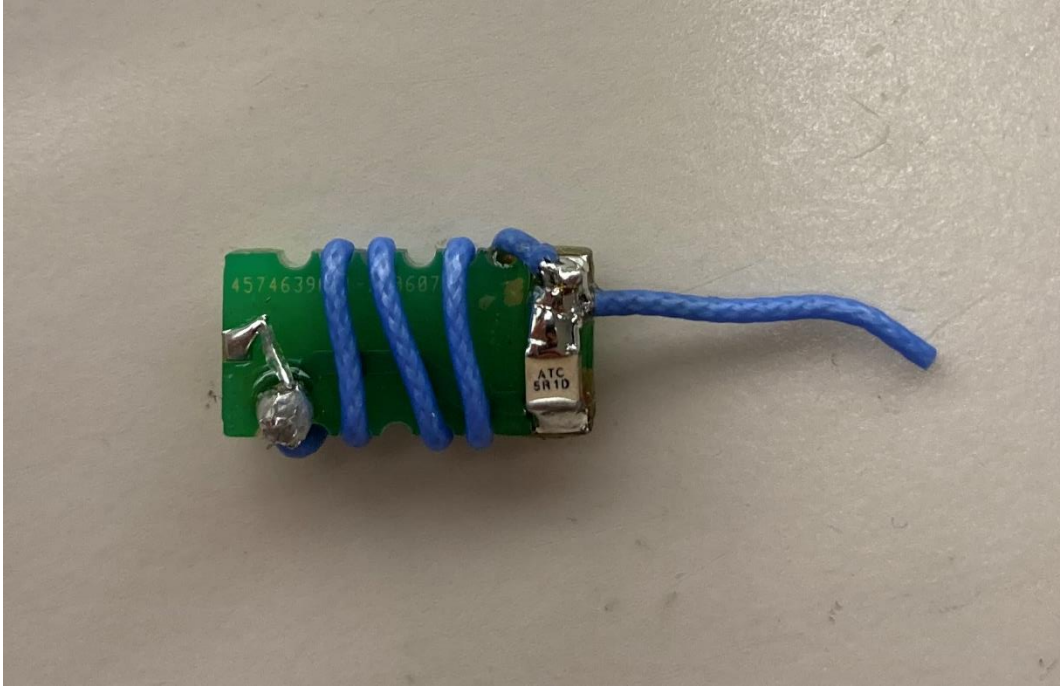


Figure 6: Example of a cable trap. Here the coiled coaxial cable forms the inductance of the LC circuit, and a lumped element capacitor forms the capacitance.

3.4.6 Preamplifier Decoupling (receive arrays)

In coil arrays, geometric decoupling is used to isolate adjacent surface coil elements. Non-adjacent surface elements are decoupled using a method called *preamplifier decoupling*.^{37-39,41} This method consists of attenuating the currents responsible for the mutual inductance between elements by introducing a decoupling circuit at the input of a low input impedance preamplifier. The decoupling circuit is designed to present the low impedance at the input of the preamplifier as a high impedance at the coil terminals.^{37-39,41} A key feature of preamplifier decoupling circuits is that they maintain the ideal impedance match condition at the preamplifier input. Many circuit designs exist which can achieve this impedance transformation, such as phase shifters and matching networks as discussed above.^{37,38} Though current is limited in the coil by the introduction of these circuits, the MR signal is still present in the form of a voltage across the terminals of the coil.

3.5 Coil Design and the RF Lab

3.5.1 Simulation

RF coil design typically begins with electromagnetic simulations of coil performance. Many methods exist for performing these simulations, including Finite Element Modelling (FEM), Finite Integration Technique (FIT), and Method of Moments (MoM), each of which provides advantages and disadvantages in terms of computational speed, accuracy and applicability.³⁸ Regardless of the method chosen, a typical EM simulation for RF coil design involves defining the RF coil circuitry and analyzing the effects of the produced EM fields in a chosen sample. Such simulations are useful for providing a first estimate of coil design and performance, including tuning and matching circuitry, B_1^+ efficiency and homogeneity and SAR maps.³⁸

3.5.2 Vector Network Analyzer (VNA)

Prior to imaging, RF coils are analyzed and evaluated in the lab using a Vector Network Analyzer (VNA).³⁹ VNAs are used broadly in RF and microwave engineering to analyze the impedance at and between the ports of a microwave or RF network (such as an RF coil).⁴⁸ This impedance is represented by the VNA in the form of *scattering parameters* (S-parameters), which consist of the reflection coefficients S_{ii} and the transmission coefficients S_{ij} , where $N = i = j$ is the number of ports in the network.³⁹ The reflection coefficient S_{ii} is given by the ratio of the reflected signal at port i to the incident signal at port i . Transmission coefficient S_{ij} is given by the ratio of the transmitted signal at port j to the incident signal at port i . S-parameters are complex, dimensionless quantities, and are normally represented by the VNA in decibels [dB].³⁹ For a network with an arbitrary number of ports, the S-parameters can be represented in a scattering matrix (S-matrix). For example, a three-port network would be represented by the S-matrix:

$$\begin{bmatrix} S_{11} & S_{12} & S_{13} \\ S_{21} & S_{22} & S_{23} \\ S_{31} & S_{32} & S_{33} \end{bmatrix}$$

Here, the reflection coefficients form the diagonal and the transmission coefficients form the off-diagonal elements. In RF coils, reflection coefficients provide an indication of the quality of the impedance match, with lower reflection coefficients indicating a better match than higher

reflection coefficients.³⁹ Transmission coefficients can be used to provide an indication of the quality of decoupling between the RF coil elements, with lower transmission coefficients indicating better decoupling.³⁹ The VNA can also be used in conjunction with a single or double-loop probe in order to assess the resonant frequency of the coil elements or the quality of the active detuning and preamplifier decoupling.^{39,42} These probes are connected to the VNA and magnetically couple to the RF coil element under test. Single-loop probes are used to measure the transmission between the probe and the RF coil element, whereas double-loop probes are used to measure the transmission between two, geometrically decoupled single-loop probes in the presence of the RF coil element.^{39,42}

3.6 Coil Performance Metrics

3.6.1 Quantifying Coil Losses (Quality Factor)

RF coils exhibit several loss mechanisms which can reduce the efficiency of the coil and increase noise in the detected MR signal. These mechanisms are generally divided into sample- and coil-based losses.^{38,39} Sample losses arise from the interaction of the excitation field with the sample. As discussed above, the changing magnetic flux of the B_1^+ excitation field induces currents in the conductive sample, generating heat through ohmic losses.³² Coil-based losses involve ohmic and radiative losses from the conductors in the coil, as well as losses due to the interaction of the conservative electric field with the sample.³⁷⁻³⁹ Sample based losses are difficult to mitigate, as they are inherent to the MR imaging experiment. As such, RF coil design is typically focused on reducing coil-based losses.

Loss in RF coils can be quantified by the Q factor (Q), which is expressed theoretically as^{38,39}

(3.22)

$$Q = \frac{\omega L}{R}$$

Where ω is the Larmor frequency, L is the inductance of the coil, and R is the resistance of the coil. In practice, the Q factor is measured using a single or double-loop probe and the VNA as⁴²

(3.23)

$$Q = \frac{f_0}{\Delta f_{-3dB}} \quad \text{Double Loop}$$

$$Q = 2 \frac{f_0}{\Delta f_{-3dB}} \quad \text{Single Loop}$$

Where f_0 represents the resonant frequency of the coil element and Δf_{-3dB} represents the -3 dB bandwidth. Higher Q factors indicate that the coil exhibits lower losses.

One method of assessing the loss mechanisms of a coil is by comparing the relative contributions of sample-based and coil-based losses to the total losses exhibited by the coil. This is quantified by the Q-ratio, the ratio of the Q-factor of the coil without a sample (unloaded) to the Q-factor of the coil with a sample (loaded). One of the goals of RF coil design is to have a high Q-ratio, indicating that coil losses are small compared to sample losses.⁴²

3.6.2 Signal-to-Noise Ratio (SNR)

The signal-to-noise ratio (SNR) in MRI typically refers to the SNR of an MR image, that is, the ratio of the mean image signal to the standard deviation of the background noise. Image SNR is dependent on several factors, including the design of the RF coil. One of the primary goals of RF coil design is to maximize the achievable SNR of the coil. The effect of the coil on SNR can be seen by comparing the strength of a theoretical MR signal generated in a specific voxel, ΔV , in a uniform sample to the strength of the noise signal generated by the loss mechanisms describe previously. The voltage induced in an RF coil from this voxel, assuming a static B_1^+ and B_0 field, is given by^{38,39}

(3.24)

$$V_{signal} = \sqrt{2}\omega\Delta VM_{xy}B_t$$

Where ω is the Larmor frequency, M_{xy} is the transverse magnetization in the voxel, and B_t is the effective sensitivity of the coil. The root mean square (RMS) noise voltage is given by³⁹

(3.25)

$$V_{noise} = \sqrt{4kT\Delta fR}$$

Where k is Boltzmann's constant, T is the temperature, Δf is the bandwidth and R represents the coil losses. Combining these equations yields the SNR of the coil.³⁸

(3.26)

$$SNR = \frac{V_{signal}}{V_{noise}} = \frac{\sqrt{2}\omega\Delta VM_{xy}B_t}{\sqrt{4kT\Delta fR}}$$

Though not very practical, this equation shows the effects of the coil on SNR, as well as how SNR can be lost at the coil level. Without increasing the voxel size, it can be seen that SNR can be improved by increasing the sensitivity of the coil or by decreasing coil losses.

3.6.3 B_1^+ Efficiency and Homogeneity

The performance of the transmit coil is typically evaluated based on the efficiency and homogeneity of the B_1^+ excitation field.³⁸ B_1^+ efficiency is defined as the B_1^+ field per unit input power to the coil and is typically given in $\frac{\mu T}{\sqrt{W}}$. A coil with lower losses will have a higher B_1^+ efficiency. Transmit homogeneity represents the uniformity of the B_1^+ field over the imaging volume and is typically represented by a B_1^+ field map or flip angle map.³⁸ Homogeneous excitation over the imaging volume is important for SNR, image uniformity and contrast uniformity between tissues, as the magnitude of the transverse magnetization is related to the flip angle achieved by the B_1^+ field.

3.6.4 Parallel Imaging and the Geometry Factor (g-Factor)

As mentioned previously, coil surface arrays can be used to accelerate MR imaging through a technique called Parallel Imaging. This method functions by reducing the total number of k-space lines acquired, shortening the acquisition time by reducing the FOV of the image. This is known as "undersampling" and typically results in aliasing artifacts if the reduced FOV is smaller than the imaged sample.⁴³ Aliasing artifacts occur when the signal measured at one part of the sample is indistinguishable from the signal measured at another.³⁵ The result is an image with overlapped signal from different regions of the sample. Parallel imaging compensates for aliasing by leveraging the fact that elements in a phased array are more sensitive to the specific region of the

sample nearest to them. This provides additional spatial information about the received MR signal, which can be used in combination with the undersampled data to reconstruct the full, unaliased MR image.⁴³ Parallel imaging is often accompanied with a reduction in SNR, which depends on the specific algorithm used to perform the image reconstruction. Using the SENSE algorithm, a common parallel imaging algorithm in clinical use, the reduction in SNR is given by⁴³

(3.27)

$$SNR_{PI} = \frac{SNR}{g\sqrt{R}}$$

Where R is the acceleration factor (e.g., $R = 2$ if k space is undersampled by a factor of 2) and g is the geometry factor. The coil geometry factor is based on the sensitivity profiles of the individual receive coil elements and is always greater than or equal to one. Since parallel imaging relies on being able to distinguish the signal from different individual receive coils, it is important that these sensitivity profiles be uncorrelated between receive elements in the same RF coil.⁴³ Since the sensitivities of the individual receive coils are generally more similar towards the center of the sample, the SNR loss related to the g-factor is generally greatest at the center of the reconstructed image. g-Factor maps are a method of quantifying the SNR loss from parallel imaging which is attributable to the RF coil.

3.7 Concurrent Studies in Size-Adaptive RF Coil Design

In 2011, Keil et al. developed five size-optimized, 32-channel brain arrays for 3 T pediatric imaging.²⁵ Each array was optimized for a specific pediatric age group, which included neonates, 6-month-olds, 1-year-olds, 4-year-olds, and 7-year-olds. The goal of this work was to identify the potential SNR and parallel imaging performance gains of developing close-fitting arrays designed specifically for pediatric subjects. Each of the size-optimized coils consisted of a posterior segment to cover the back of the head and a “frontal paddle” to cover the forehead, forming a helmet when both segments are combined. The shape and size of the helmet was obtained by performing surface contours of aligned 3D MRI scans of 20 children of both sexes in each age group. The coil shape was then further modified by increasing the size of the 95th percentile contour to accommodate 3mm of foam padding. The obtained head contours were also used to design size-matched,

pediatric head phantoms based on the average head size in each age group. Each receive coil consisted of 32 circular loop elements arranged in a soccer ball-based overlapping tiling pattern. Each receive element included an active detuning circuit comprised of a PIN diode and LC trap circuit, as well as a fuse for passive protection against large currents. The constructed arrays were evaluated against a commercially available 32-channel adult head array and a pediatric-sized circular polarized BC at 3 T. SNR was evaluated based on size-matched pediatric head phantom imaging and *in vivo* imaging of an adult subject whose head was capable of fitting within the 4-year-old and 7-year-old size-optimized coils. The size-optimized coil arrays all showed higher global SNR compared to both the pediatric BC and 32-channel adult coil in the phantom imaging tests. Compared with the 32-channel adult coil, the size-optimized coils showed 2.8-, 2.3-, 2.0-, 1.8-, and 1.6-fold improvement in global SNR for the neonate, 6-month-old, 1-year-old, 4-year-old, and 7-year-old coils, respectively. Compared with the pediatric BC, the size-optimized coils showed 3.4-, 3.1-, 2.8-, and 2.4-fold improvement in global SNR for the neonate, 6-month-old, 1-year-old, 4-year-old, and 7-year-old coils, respectively. The increase in SNR was confirmed *in vivo*, with 2.2- and 1.5-fold SNR increases at the periphery of the brain and 9 % and 5 % SNR increases at the center for the 4- and 7-year-old coils, respectively. The size-optimized coils also yielded overall lower g-factors compared with the standard 32-channel adult coil and pediatric BC, providing roughly one additional unit of acceleration. The size-optimized coils showed overall improved performance in terms of SNR and parallel imaging, indicating the potential benefits of implementing size-adaptive coils for pediatric imaging.

In 2018, Lopez Rios et al. proposed a 13-channel, size-adaptive receive array for brain MRI in human neonates at 3 T.²⁸ The coil former was designed based on the 50th percentile in head circumference of subjects 27-weeks premature to 1.5-months old, accommodating spherical head shapes ranging from 8 to 12.5cm in diameter. The coil consisted of 13 overlapped loop elements, each of which included both passive and active detuning networks. The loops were mounted onto individual mechanical supports, which were connected to a spherical frame via plastic bellows. At atmospheric pressure, the mechanical properties of the bellows maintained the coil in its smallest size. The coil dimensions could be increased by removing air from the bellows with a hand pump to create a vacuum. A custom, adjustable patient bed was designed to support the subject's body and head while the element positions were adjusted. The bellows were initially evacuated to yield the largest coil dimension. The coil was then placed on the subject's head, and air was allowed to

enter the bellows, contracting the size of the former to directly conform to the subject's head. This design allowed all coil elements to be moved independently. The coil SNR performance was evaluated at 3 T against a commercially available 32-channel adult head coil using three head phantoms designed to represent a small, medium and large neonatal head (8, 10 and 12.5 cm diameters, respectively). The size-adaptive head coil showed improved average SNR over whole axial slices, yielding a 68%, 35% and 16% increase for the small, medium and large phantoms, respectively. SNR was especially improved at the periphery of the phantom, yielding a 269%, 111% and 89% increase in SNR for the small, medium and large phantoms, respectively, in comparison with the commercial adult coil. Central SNR was found to be similar for the small phantom, and lower for the medium and large phantom by 20.6% and 34.5%, respectively, in comparison to the adult coil. This decrease is attributed to improved coverage by the commercial coil in the area of interest.

Overall, the size-adaptive neonatal head coil developed by Rios et al. yielded improved SNR in the cortex when compared to the rigid commercial adult coil, with similar or reduced SNR in the centre of the brain. This coil design also showed potential benefits in terms of improving subject comfort and reducing subject motion by stabilizing the anatomy under observation.

In 2021, Ghotra et al. presented a design for a size-adaptive 32-channel array coil for infant neuroimaging at 3 T.²⁷ The goal of this proposed design was to improve patient compliance in fMRI studies involving awake infants. The coil was designed to accommodate the 95th percentile in head circumference of infants aged 1-18 months. The coil consisted of three anatomically shaped independent segments which combined to form a helmet. The posterior part of the coil was integrated with a custom coil base and patient bed to improve subject comfort. The two anterior coil segments connected with the posterior segment and could be slid laterally to adjust the lateral dimension of the coil. The coil was adjusted in the anterior-posterior direction in four increments of 5 mm by raising or lowering the anterior segments of the coil. The anterior segments were designed with dedicated earmuff compartments to accommodate hearing protection. Each segment was designed to overlap such that the elements on separate coil segments were geometrically decoupled when the coil was in its smallest size. This coil design implemented three safety factors to protect against large currents in the receive coil: active detuning, passive detuning, and fuses. Phantom and *in vivo* imaging experiments were performed to compare SNR and parallel imaging

performance of the size-adaptive array with a commercially available 32-channel adult head coil. Subject motion was also assessed during both awake and asleep infant fMRI experiments. When loaded with an infant head phantom, the adjustable coil yielded a 2.7-fold increase in SNR in the phantom region corresponding to the pediatric human brain compared with the adult head coil. Peripheral and central SNR showed 3-fold and 1.25-fold SNR gains, respectively, when compared to the adult coil. The size-adaptive coil also performed better in terms of noise amplification with accelerated imaging techniques. Using the Simultaneous Multi-Slice (SMS) accelerated imaging technique with an acceleration factor of 6, the maximum g-factor measured across six slices was 1.06 and 1.22 for the size-adaptive and adult coils, respectively. This performance was maintained when SMS was combined with in-plane undersampled k-space acceleration, yielding a maximum g-factor of 1.2 and 2.5 for the size-adaptive and adult coils, respectively. The size-adaptive coil also resulted in fewer motion artifacts in infant fMRI studies. One of the concerns highlighted in this paper is the loss of the critical overlap when the coil size is adjusted from the default smallest size. Ghotra et al. were able to compensate for this loss of geometric decoupling by employing robust and effective preamplifier decoupling. The performance of this size-adaptive coil highlights the importance of developing size-optimized, form fitting coils for high quality pediatric imaging.

In 2023, Gilbert et al. developed a size-adaptable pediatric head coil for subjects aged 3-months to 3-years based on the previously proposed design by Ghotra et al.²⁶ The coil consisted of a fixed posterior segment, left and right lateral segments, and an interchangeable anterior segment. The left and right segments of the coil were designed to slide laterally over the posterior section to adjust the width of the coil between 12 and 17.1 cm. The coil included a locking mechanism to fix the lateral segments in the desired position. This locking mechanism also served to restrict head movement. Three interchangeable anterior segments were designed to accommodate anterior-posterior dimensions of 16.5, 18.5 and 20 cm. The coil circuitry consisted of 32 receive loop elements arranged in a soccer ball geometry, each of which included active detuning, passive detuning and fast-blow fuses. Preamplifiers were further isolated from the transmission pulse by placing a PIN diode across their inputs. Adjacent coil elements in separate segments of the coil were overlapped to mitigate inductive coupling. The pediatric size-adaptive coil was compared against two commercial adult coils, 1) a 20-channel head and neck coil and 2) a 32-channel head-only coil, based on phantom and *in vivo* imaging results. The size-adaptive coil showed improved noise correlation compared to both adult coils when loaded with a phantom designed to mimic the

2-year-old pediatric head. In imaging experiments with this phantom, the pediatric coil provided higher SNR throughout most of the brain region relative to the adult coils, with the largest gains (> 2-fold) occurring at the periphery of the brain. Only the central region of the brain as imaged by the adult head/neck coil provided improved SNR over the adjustable pediatric coil. This is attributed to the lack of receive elements in front of the face in the pediatric coil, a deliberate design decision made to allow for future integration of camera-based motion tracking. The effect of size-adaptability on SNR was quantified by imaging a phantom designed to mimic the dimensions of a 3-month-old subject at the largest and smallest sizes of the pediatric coil. In its smallest configuration, the coil showed 1.71-, 1.69-, and 1.15-fold increases in SNR in the frontal, lateral and central regions of the brain, respectively, compared with the same coil in its largest configuration. The pediatric coil also demonstrated substantially lower g-factors across all acceleration rates compared with the adult coils. The pediatric coil was capable of achieving 4-fold acceleration rates along each cartesian axis before substantial noise amplification, versus 3-fold acceleration for the adult coils. Lastly, images of a 3-month- and 1-year-old subject acquired using the size-adjustable coil yielded no sign of motion artifacts.

The results presented by Gilbert et al. further demonstrate the potential gains in coil and imaging performance which can be achieved with a size-adaptive coil design. This is particularly clear in the comparison of the pediatric coil array in imaging a 3-month-old size-matched head phantom at the largest and smallest coil dimensions. The SNR was shown to increase in each of the monitored brain regions by adapting the size of the coil to the geometry of the 3-month-old head phantom.

Chapter 4 – Nuclear Magnetic Resonance (NMR) Field Probes

Precise and accurate knowledge of the behaviour of the dynamic magnetic fields, such as the gradient and B_1^+ fields, over the imaging volume is essential for accurate and reproducible MRI. Unfortunately, there are many factors both inherent to and external from the MRI system which can cause unwanted fluctuations in the dynamic magnetic field. These fluctuations generally become more severe at higher B_0 field strengths. Field fluctuations can result in significant image artifacts which can hamper interpretation of MRI data.^{29,30}

Dynamic field fluctuations in MRI can be monitored using NMR field probes. These probes operate by measuring the nuclear spin precession of an NMR active sample, usually either fluorine or hydrogen (e.g., water), to determine the magnetic field at the location of the probe.

4.1 NMR Probe Design

A diagram of an NMR field probe is given in **Figure 7**.⁴⁹ This diagram shows the NMR active sample contained within a glass capillary and a solenoid coil surrounding the capillary to transmit and receive signal to and from the sample. The casing of the probe is susceptibility matched to ensure that the magnetic field is undistorted by the probe materials.⁴⁹

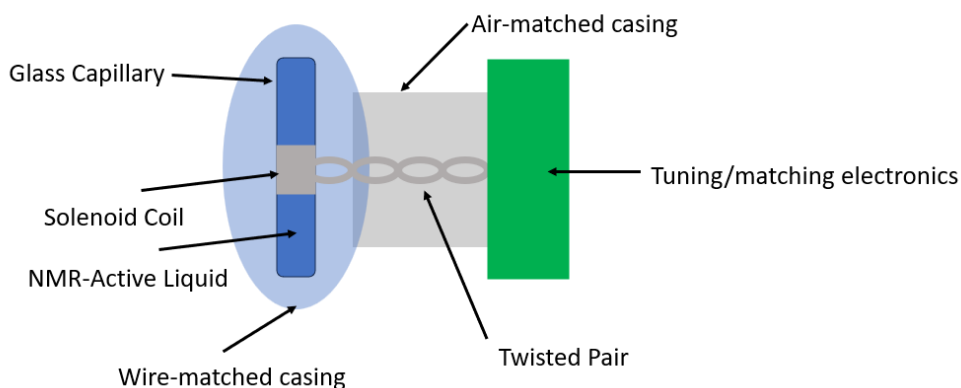


Figure 7: Diagram of an NMR probe. In this specific design, the susceptibility of the probe casing is matched to the susceptibility of the solenoid wire to minimize the effects of susceptibility on the magnetic field measurement.⁴⁹

4.2 Principles of Operation

In order to determine the magnetic field at the position of the probe, the FID signal from the NMR active sample is measured. The phase of the FID is then unwrapped and related to the magnetic field at the position of the probe using equation 4.1.⁴⁹

(4.1)

$$\phi(t) \propto \int_0^t B(\tau) d\tau$$

In this equation, the phase $\phi(t)$ is shown to be proportional to the time integral of the magnetic field $B(\tau)$. The precision of the measurement is given by equation 4.2.⁴⁹

(4.2)

$$\sigma_B \propto \frac{1}{SNR \sqrt{BW} T_{obs}^{\frac{3}{2}}}$$

In this equation, BW represents the bandwidth of the probe and T_{obs} represents the time over which the FID measurement takes place.⁴⁹

4.3 NMR Probes in MRI

The use of NMR field probes for MRI applications is complicated by the fact that the magnetic field must be monitored over the entire imaging volume rather than at discrete locations, as provided by an NMR field probe. Further, it often isn't feasible to place probes within the imaging volume (e.g., in *in vivo* imaging). As such, NMR probes in MRI are used to estimate the spatiotemporal field fluctuations within the imaging volume by sampling the magnetic field at discrete positions around the imaging volume.⁵⁰ This information is then used to estimate the field dynamics within the imaging volume using a least-squares fitting or regression. This process is bound to the following assumptions:

1. The magnetic field is of spatially low order (i.e., smooth) over the imaging volume compared to the number of sensors.⁵⁰
2. Field-generating currents reside outside the volume enclosed by the NMR probe array.⁵⁰

These assumptions hold for dynamic fields produced by the gradient, shim and RF coils, fluctuations in the main magnetic field, and dynamic fields arising from changes in the susceptibility distribution resulting from subject motion outside the imaging volume. The assumptions do not hold for static fields within the imaging volume, which can be of high spatial order due to the highly structured susceptibility distribution within the imaging volume.^{50,51} As such, this method of employing NMR field probes is only effective for measuring dynamic magnetic fields produced outside the imaging volume.⁵⁰

4.4 Principles of NMR Field Probe Array Operation

Consider the magnitude of a magnetic field, B , which is separable into a dynamic and static component as shown in Equation 4.3, in which $B_D(\mathbf{r}, t)$ and $B_{ref}(\mathbf{r})$ represent the dynamic and static components, respectively.

(4.3)

$$|B(\mathbf{r}, t)| = B_D(\mathbf{r}, t) + B_{ref}(\mathbf{r})$$

Given the assumptions listed previously, namely that the dynamic field is spatially smooth, the dynamic component of the magnetic field can be represented by a linear combination of static basis functions with dynamic coefficients.

(4.4)

$$B_D = \sum_{I=0}^{N_L-1} c_I(t) f_I(\mathbf{r})$$

Here, $c_I(t)$ represent the dynamic coefficients and $f_I(\mathbf{r})$ represent the basis functions. This yields a total magnetic field magnitude as shown in the equation below.⁵⁰

(4.5)

$$|B(\mathbf{r}, t)| = \sum_{I=0}^{N_L-1} c_I(t) f_I(\mathbf{r}) + B_{ref}(\mathbf{r})$$

Based on Equation 4.1, we can calculate the phase accrued by a spin experiencing this magnetic field using Equation 4.6 below.

(4.6)

$$\phi(\mathbf{r}, t) = \sum_{I=0}^{N_L-1} k_I(t) f_I(\mathbf{r}) + \omega_{ref}(\mathbf{r})t$$

In which $\omega_{ref}(\mathbf{r})$ refers to the Larmor frequency at the reference field given by the Larmor equation and the dynamic coefficients $k_I(t)$ represent the time integral of the dynamic coefficients $c_I(t)$.⁵⁰

(4.7)

$$k_I = \gamma \int_0^t c_I(\tau) d\tau$$

The goal of employing NMR field probes is to determine the $k_I(t)$ coefficients. These, coupled with the chosen set of basis functions, define the dynamic magnetic field over the imaging volume. Since the magnetic field is being sampled at discrete locations, the position of each of the probes is held constant, yielding Equation 4.8 below for the phase accrued by a given probe.⁵⁰

(4.8)

$$\phi_j(t) = \frac{\gamma_P}{\gamma} \sum_{I=0}^{N_L-1} k_I(t) f_I(r_j) + \omega_{ref_j} t$$

Here, γ_P represents the gyromagnetic ratio of the NMR active sample of the probe and $\phi_j(t)$ represents the phase accrued by the j^{th} probe as a function of time. The term r_j represents the position of the j^{th} probe and ω_{ref_j} represents the Larmor frequency given by the reference static magnetic field at position r_j . The position and Larmor frequency of the probe are acquired through calibration. The Larmor frequency is determined by measuring the magnetic field at the probe position without the application of dynamic fields.⁵⁰ The position is determined by measuring the magnetic field at the probe positions under the application of well-characterized gradient fields.⁵⁰

Equation 4.8 can be expanded to a system of N_p probes using vector notation to represent the system dynamics, as shown below.

(4.9)

$$\boldsymbol{\phi}_P(t) = \mathbf{P}\mathbf{k}(t) + \boldsymbol{\omega}_{ref,p}t$$

In which,

(4.10)

$$\mathbf{k}(t) = \{k_1(t), k_2(t), \dots, k_{N_L-1}(t)\}$$

(4.11)

$$\boldsymbol{\phi}_P(t) = \{\phi_1(t), \phi_2(t), \dots, \phi_{N_p}(t)\}$$

(4.12)

$$\boldsymbol{\omega}_P = \{\omega_{ref,1}, \omega_{ref,2}, \dots, \omega_{ref,N_p}\}$$

(4.13)

$$\mathbf{P} = \begin{bmatrix} f_0(r_1) & \cdots & f_{N_L-1}(r_1) \\ \vdots & \ddots & \vdots \\ f_0(r_{N_p}) & \cdots & f_{N_L-1}(r_{N_p}) \end{bmatrix}$$

Here, $\boldsymbol{\phi}_P(t)$ is a vector containing the phase accrued by each probe over time t , $\boldsymbol{\omega}_{ref,p}$ is a vector containing the Larmor frequency of spins in the static reference field at each probe position, \mathbf{P} is a matrix containing the set of basis functions used to describe the dynamic field at each position, and $\mathbf{k}(t)$ represents the dynamic coefficients defining the entire probe array. We can rearrange this equation to solve for the $\mathbf{k}(t)$ coefficients using a least-squares fitting or regression technique, as shown in Equation 4.14 below.

(4.14)

$$\mathbf{k}(t) = \mathbf{P}^+[\boldsymbol{\phi}_P(t) - \boldsymbol{\omega}_{ref,p}t]$$

Here, \mathbf{P}^+ represents the Moore-Penrose pseudoinverse of \mathbf{P} .⁵⁰ Using this process, the dynamic magnetic field over the imaging volume can be estimated in terms of the chosen set of basis functions, usually spherical or cylindrical harmonics, with the optimized dynamic coefficients determined through the fitting process. This information can then be used to correct for fluctuations in the dynamic field in real time or during image reconstruction.

4.5 Concurrent Studies in Integrated NMR Field Probe and RF Coil Design

In 2014, Duerst et al. proposed a real-time proportional-integral (PI) feedback control mechanism for stabilizing magnetic field fluctuations in MR imaging experiments at 7 T using dynamic shimming.⁵² The magnetic field was monitored at discrete locations using an array of 16 NMR field probes. This information was then used to update the MRI system's native shim and gradient coils to correct for field fluctuations. This correction was performed under the assumption that the field fluctuations and correction field produced through dynamic shimming share the same relevant degrees of freedom. As such, it was assumed that each shim field could be described uniquely by the values they assume at the positions of the 16 field probes. Under this assumption, field correction was achieved by explicitly controlling the field at the position of the probes. The probes were arranged on the cylindrical surface of a 32-channel receive head coil in four parallel rings of four probes, with adjacent rings offset by 45° to ensure that field responses from different shim channels generated at these positions were close to orthogonal. The proposed feedback-control method was evaluated in terms of its ability to correct for thermal field drifts during a gradient-intensive Echo-Planar Imaging (EPI) sequence, as well as field fluctuations arising from subject breathing. Thermal field drifts and fluctuations from subject breathing of up to 15 Hz were measured using the probes and reduced to the MR systems baseline stability of 0.5 Hz using the feedback-control approach. T_2^* -weighted images performed with concurrent field correction showed a reduction in ghosting, blurring and signal loss artifacts compared to images taken without field correction. This correction technique was limited in its ability to correct for high frequency field fluctuations due to a 20 ms latency between detection by the NMR field probe and activation of the correction field.

In 2015, Wilm et al. investigated the potential of concurrent field monitoring using NMR probes and retrospective image correction for correcting field perturbations in diffusion-weighted (DW)

MRI at 3 T.⁵³ An array of 16 NMR field probes was integrated into an eight-channel receive head coil array. The probes were positioned in four rings of 5, 6, 4 and 1 probe per ring around the imaging volume to optimize conditioning for 3rd-order spherical harmonics expansion. Three *in vitro* DW imaging experiments were performed using a single-shot DW-EPI sequence and a low-diffusivity oil phantom: 1) with the scanner's native eddy current correction (ECC) active, 2) without the ECC, and 3) after a gradient-intensive EPI sequence to evaluate the effect of temperature on field fluctuations. The 3rd experiment was repeated *in vivo*. Image reconstruction was performed iteratively without correction, with low-order correction (0th and 1st order) and with the full 3rd order correction in order to assess the effects of higher-order fluctuations on image quality. Wilm et al. found that eddy currents induced by DW gradients and B₀ drift comprised the most significant sources of field perturbations in diffusion-weighted imaging (DWI). It was also demonstrated that the eddy currents generated during DWI had significant higher-order components which could not be corrected by the scanner's ECC. Temperature induced field perturbations were also found to include higher-order components. These higher order terms reduced image congruence and resulted in ghosting artifacts. Irrespective of the use of ECC, field monitoring and retrospective correction were shown to eliminate any visual ghosting artifacts and yield almost complete image congruence across all performed MR experiments, whether *in vitro* or *in vivo*. This improved image congruence was shown to strongly improve the quality of quantitative diffusion data *in vivo*. This was demonstrated by the removal of non-anatomical diffusion tensor anisotropy in DWI human brain images. The results presented by Wilm and colleagues represent the importance of higher-order field fluctuations in DW MRI. They also highlight the potential of concurrent monitoring using NMR probes and retrospective correction in compensating for these fluctuations to enhance image quality.

In 2019, Brunner and colleagues proposed the first RF head coil design with fully integrated magnetic field monitoring capability at the International Society for Magnetic Resonance in Medicine (ISMRM) Annual Meeting and Exhibition in Montreal, Canada.⁵⁴ The proposed 16-channel 3 T receive head coil was designed to house 16 NMR field probes. The size of the head coil was chosen to accommodate 95 % of subjects, with elements covering the entire head apart from the face. The coil was designed to interface with a 3 T MRI scanner, whereas the probe system was connected to a dedicated spectrometer. As such, the coil and probes operated using separate data acquisition systems, with data being synchronized and combined downstream for image

reconstruction. The 16-channel custom coil performance was evaluated against a commercial clinical 32-channel head coil based on optimal SNR and g-factor maps at 3 T. The performance of the fully integrated magnetic field monitoring system was demonstrated through retrospective correction of single-echo diffusion scans with spiral and EPI readout for comparison. The custom 16-channel coil array demonstrated improved sensitivity compared to the commercial 32-channel coil, especially at the periphery of the brain, despite the higher channel count of the commercial coil. This is attributed to the coil's design being tailored to neuroscientific applications, as opposed to the commercial coil which was designed for clinical purposes. The mean and maximum g-factors presented by the custom coil were also found to be 6% to 85% and 21% to 111% lower, respectively, than the g-factors presented by the commercial coil. The integrated NMR probes allowed for retrospective correction of eddy currents, gradient chain delays and magnet drift. These results are similar to those presented previously by Wilm et al. but acquired using a completely integrated field monitoring system.

In 2021, an 8-channel parallel transmit, 32-channel receive RF head coil with integrated field monitoring capability for 7 T MRI was proposed by Gilbert and colleagues.⁵⁵ The transmit coil consisted of six inductively shortened dipole elements spaced evenly about the circumference of a cylindrical housing, and two self-decoupled loops positioned behind the cerebellum. The receive coil was comprised of 32 geometrically decoupled loops arranged in a soccer ball geometry. A commercial field monitoring system (Skopec Magnetic Resonance Technologies Clip-On Camera) consisting of 16 ^{19}F based NMR field probes was integrated into the coil. The position of the NMR field probes on the coil was iteratively determined by adjusting the ideal arrangement of the probes as provided by the manufacturer to accommodate the physical dimensions of the head coil as well as the limited linear region of a head-only gradient coil. The position of the probes was then further modified to minimize coupling between the probes and the coil circuitry, and to minimize the effect of local field inhomogeneity caused by the susceptibility of certain coil materials. Due to the size constraints of the coil, the final probe positions were outside the ideal linear region of the head-only gradient coil. Probes were placed between the transmit and receive coil. After probe integration, the transmit and receive coil elements had to be retuned and impedance matched to compensate for changes introduced by the probes. Field probe cables were bundled into sets of four within the coil housing. Each bundle was passed through a floating sleeve balun to suppress common-mode currents. The NMR probes were connected to a dedicated spectrometer and

preamplifier box (Skopec Magnetic Resonance Technologies) via a custom socket integrated in the MR scanner. The performance of the coil was assessed in-terms of transmit efficiency, SNR and g-factor maps before and after probe integration. The performance of the field probes was evaluated when the probes were integrated into the coil and when they were located on the manufacturer's scaffold (i.e., representing the optimal probe arrangement). Probe performance was assessed in-terms of FID amplitude and lifetime, as well as reconstruction of images acquired through a DW single-shot spiral sequence.

Integration of field probes caused a mean decrease in B_1^+ efficiency of 4% across all channels, which was compensated by employing B_1^+ shimming. The B_1^+ uniformity remained constant over the whole brain at 26%, indicating that the probes had a minimal effect on the performance of the transmit coil. The mean difference in B_1^+ corrected SNR was 1% across all channels. No change in mean g-factor was observed after integration of the field probes. The mean change in probe FID lifetime and amplitude after integration with the coil was 0.8 ± 0.02 -fold and 0.86 ± 0.01 -fold, respectively. In image reconstruction and correction, the coil and integrated field probe system was not capable of performing 3rd order correction without the introduction of systematic error. This error could be reduced by limiting the correction to 2nd order, which still showed significant improvement over the uncorrected spiral acquisition images. The error introduced by 3rd order correction was attributed to the probes being positioned outside the linear region of the head-only gradient field, resulting in spatially non-linear phase accrual of FID phases.

The results published by Gilbert et al. demonstrate a workflow for NMR probe integration with RF coils, as well as a method to assess how the interactions between these two systems affect each others performance.

The objective of this thesis was to design a size-adaptive pediatric RF head coil for 7 T MRI with integrated magnetic field monitoring capability, building upon the works cited above. As demonstrated previously by Keil et al., Rios et al., Ghotra et al. and Gilbert et al., coil performance in terms of SNR and g-factor can be increased substantially by employing a size-adaptive former design.²⁵⁻²⁸ Such systems can also be employed to mitigate motion artifacts because they allow securing of the subject's head. We specifically aimed to build upon existing work by designing our size-adaptive coil for 7 T MRI of pediatric subjects aged 4-9 years old. Our coil was designed to

operate at 7 T (higher field strength than previous designs) and with an older age group than considered in previous work. This provided additional challenges compared to previous size-adaptive coil designs, due to the absence of an integrated body coil and the increase in SAR associated with imaging at higher fields. It further necessitated the design and construction of a custom transmit coil optimized for 7 T pediatric imaging that allowed size adaptability of the receive former. This thesis also aims to build upon the work presented by Duerst et al., Wilm et al., Brunner et al. and Gilbert et al. by integrating NMR field probes with a size-adaptive pediatric coil for 7 T MRI.⁵²⁻⁵⁵ This is further complicated for pediatric imaging due to the smaller imaging volume, reducing the available space for optimally positioning the NMR probes.

Chapter 5 - Manuscript

A size-adaptive radiofrequency coil with integrated NMR field probes for Magnetic Resonance Imaging of the pediatric human brain at 7 T

Christian Sprang^{1,2}, Pedram Yazdanbakhsh^{1,3}, Marcus Couch⁴, Sajjad Feizollah^{1,3}, Christine L. Tardif^{1,2,3}, David A. Rudko^{1,2,3}

1. McConnell Brain Imaging Centre, Montreal Neurological Institute and Hospital, Montreal, QC, Canada
2. Department of Biomedical Engineering, McGill University, Montreal, QC, Canada
3. Department of Neurology and Neurosurgery, McGill University, Montreal, QC, Canada
4. Siemens Healthcare Limited, Montreal, QC, Canada

Corresponding Author: David A. Rudko

Email: david.rudko@mcgill.ca

Phone Number: 514-398-3345

Address: Montreal Neurological Institute, Room WB 375
3801 University Street
Montreal, QC, Canada, H3A 2B4

Word count: 4962

Abstract

Purpose: Ultra-high field, 7 T human MRI is currently limited to subjects above 30 kg due to SAR considerations. The purpose of this work was to develop a safe, size-adaptive radiofrequency head coil with an integrated commercial field monitoring system comprised of 16 NMR field probes for pediatric (4-9 years-old) 7 T MRI.

Methods: The coil consisted of an eight-channel transmit coil with eight notched dipole elements operating in parallel transmit mode and a 32-channel conformal, size-adaptive receive array. Coil performance was evaluated at the largest and smallest dimensions of the receive former, with and without integrated field probes. Performance of the array was compared to that of a commercial eight-channel transmit, 32-channel receive adult head coil (Nova Medical). Field probe measurements were evaluated when integrated at the different sizes of the receive former and when externally mounted on the manufacturer's scaffold.

Results: Simulations of transmit coil SAR and B_1^+ performance demonstrated that the coil is safe for pediatric imaging of subjects below 30 kg at 7 T. The SNR performance of the coil was improved by adapting the coil to conform to the imaged sample, yielding SNR comparable to that of the commercial coil. The field probes enabled up to 2nd order spherical harmonic correction of dynamic magnetic field fluctuations in EPI acquisitions. Coil performance was altered by both size-adjustment of the Rx coil and integration of the field probes.

Conclusions: The proposed size-adaptive coil enables safe, high-quality imaging of subjects below 30 kg at 7 T.

Introduction

Pediatric neuroimaging research can significantly benefit from the reduced scan times and improved spatial/temporal resolution afforded by ultra-high field (UHF), 7 tesla (T) magnetic resonance imaging (MRI). Thus, 7 T MRI has the potential to act as a powerful tool for studying human neurodevelopment and neurodevelopmental disorders. However, there are notable challenges to performing pediatric neuroimaging research, particularly at UHF.

One of the most challenging aspects of pediatric neuroimaging is the impact of head motion during MRI scans.¹⁻³ Historically, this has been addressed using general anesthetic and sedation. This practice is still implemented clinically, but has generally been discontinued in research due to the associated risks.⁴ Other methods to limit motion include performing scans while pediatric subjects are asleep, reducing the level of noise in the scanner and/or implementing practice sessions in a mock scanner to better prepare the subject.⁴ Subject motion can also be addressed by using MRI pulse sequences that are less sensitive to motion, or by implementing motion correction techniques.⁵ Reducing the duration of the scan can also assist in reducing subject motion, highlighting the benefits of UHF MRI for pediatric neuroimaging.^{2,6}

Pediatric-specific MRI hardware, such as radiofrequency (RF) coils designed to conform to the smaller brain anatomy of pediatric subjects, can reduce the impact of motion. Such designs have the additional benefit of improving coupling between tissue and the RF coil elements, resulting in higher signal-to-noise ratio (SNR) in MR images. However, the design of pediatric-specific RF coils is complicated by the range of pediatric head sizes throughout neurodevelopment.⁷ As such, many pediatric coils are built to accommodate a limited range of head sizes. In an effort to improve the versatility and overall performance of pediatric RF head coils, recent work has examined size-adjustable designs that provide improved performance over a range of head sizes.⁸⁻¹¹

Apart from the conventional challenges of pediatric neuroimaging, UHF MRI provides its own set of challenges which further complicate imaging experiments. For instance, 7 T MRI is prone to more severe magnetic field distortions than conventional field strength MRI.¹²⁻¹⁴ These distortions can arise from a number of different sources, including both hardware imperfections (eddy currents, gradient delays, mechanical vibration, component heating, etc.) and subject motion.^{12,13,15} Recently, the use of nuclear magnetic resonance (NMR) field probes has been shown to be an effective method for monitoring and correcting field fluctuations stemming from a range of

sources.¹⁶⁻¹⁹ As a result, NMR field probes have been integrated into several recent UHF coil designs.^{13,15,20,21}

A further challenge of UHF MRI is the inhomogeneity of the excitation transmit field due to the increase in the Larmor frequency. As a result, 7 T MRI systems are generally not outfitted with an integrated body coil, requiring the design of a separate transmit (Tx) or parallel transmit (pTx) coil to complement the usual receive (Rx) phased array.²² Additionally the increase in magnetic field strength is also associated with an increase in specific absorption rate (SAR), which is an important consideration for pediatric imaging.⁶ Partly as a result of SAR considerations, there are currently no commercially available RF head coils for pediatric neuroimaging of subjects below 30 kg at 7 T.²³

The present work evaluates the design, construction and testing of a size-adaptive RF coil with integrated magnetic field monitoring, using the Skope Clip-On Camera (Skope Magnetic Resonance Technologies), for pediatric neuroimaging at 7 T. The coil was designed to accommodate subjects aged 4-9 years old.

Methods

RF Coil Design

Coil Housing

The coil housing consisted of two physically separable mechanical systems: (i) a rigid Tx housing and (ii) a size-adjustable Rx former (**Figure 8, a**). The Tx coil housing was created using concentric polycarbonate cylinders with end cap rings to provide structural rigidity and isolate the transmit electronics. The outer diameter of the cylindrical housing was 356 mm. The inner diameter of the cylindrical housing was 240 mm. The total height of the cylinder was 270 mm. The transmit coil housing accommodated visual MR experiments by introducing two eye holes separated by a 23 mm gap. The gap was used to accommodate transmit coil electronics. The eye holes each had dimensions of 94 x 60 mm² and, together, provided a lateral field of view of 64°.

The Rx coil housing was comprised of five physically separable mechanical components, one each for the anterior, posterior, left, right and superior regions of the head (**Figure 8, d**). These components were designed such that they could be combined to form a helmet which would

conform to the shape of the pediatric human head. Adjacent Rx coil housing components were also designed to overlap, such that receive elements from adjacent housing elements could be geometrically decoupled. This is similar to the technique described by Ghotra et al. at 3 T.⁹

A specific goal of the Rx housing design was to accommodate subjects with head sizes ranging from the 5th to the 95th percentile of children aged four to nine years old. To this effect, the lateral/medial and anterior/posterior internal dimensions of the helmet could be expanded or contracted by 22 and 27 mm, respectively. This was accomplished by adjusting the relative positions of the individual Rx former components. Once at the optimal size, the individual Rx components could be locked in place using custom clamping knobs. The minimum and maximum achievable dimensions of the helmet in the lateral-medial direction were 150 and 172 mm. In the anterior-posterior direction, the minimum and maximum achievable dimensions were 180 and 207 mm (**Figure 8 b), c**). The overall internal depth of the helmet (superior/inferior) was 221 mm. Eye holes were also integrated into the receive coil design (**Figure 8 d iii**). The receive housing eyeholes were designed with the same dimensions as the transmit housing eyeholes, apart from a narrowing near the bottom of the face to provide room for the subject's nose. The Rx former was primarily 3D printed in-house, with specialized components printed by an external company (OSSY House Inc.).

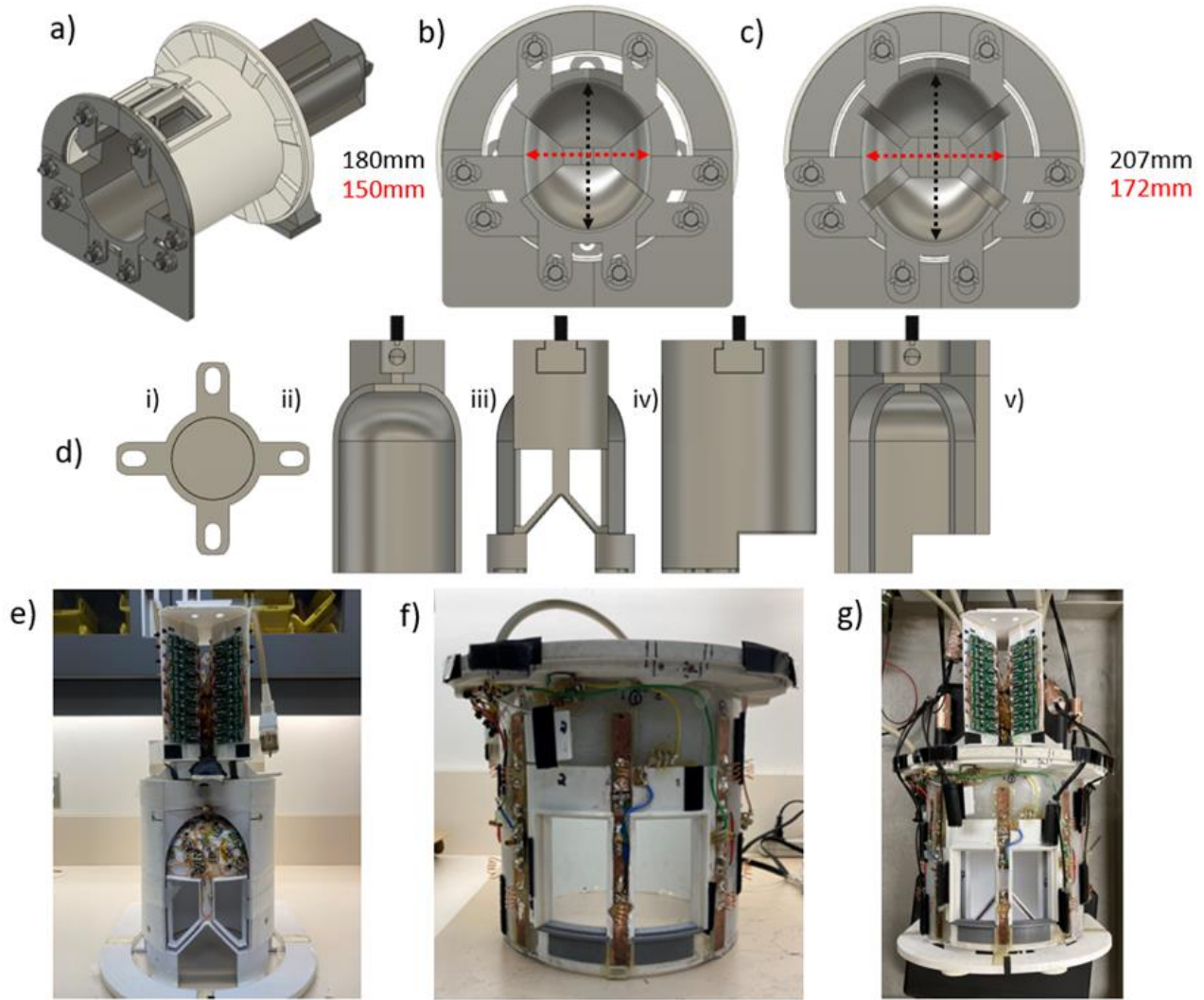


Figure 8: Mechanical design of pediatric coil receive and transmit former: a) CAD model of combined Tx (white) and Rx (grey) coil formers without the outer Tx cylinder, b) Rx coil former adjusted to smallest size, c) Rx coil former adjusted to largest size, d) mechanical components of Rx coil former (i) superior, ii) posterior, iii) anterior, iv) right, v) left), e) receive coil with electronic components, f) Tx coil with electronic components, g) combined Rx and Tx coils with integrated Skope NMR field probes.

Transmit Coil

The transmit coil was comprised of eight dipole antennas offset by 45° to provide full coverage of the head (**Figure 8, f**). The dipoles consisted of a 15 mm wide, 210 mm long copper sheet mounted onto an FR-4 glass-reinforced epoxy laminate (**Figure 9**). The dipoles were tuned to 297.2 MHz using variable inductors placed at either side of the input port (**Figure 9, a, h**). Variable capacitors (Knowles Johanson 80H85) were used to match the dipoles to 50Ω at 297.2 MHz.

Active detuning was accomplished by using two high power PIN diodes (Macom MA4PK2000) on either side of the input port. The PIN diodes were forward biased during the transmit pulse using 1 μ H RF chokes (Richard Jahre GmbH). The 100mA DC current used to forward bias the PIN diodes was blocked from propagating the full length of the dipole by two fixed value 680 pF, high power capacitors (American Technical Ceramics). The dipoles were connected via coaxial cables to a pTx connector plug (ODU-MAC), with cable traps tuned to 297.2 MHz placed at increments of $\lambda/10$ to mitigate common-mode currents travelling along the shield of the coaxial cable.

The low-footprint design of dipole antennas provided flexibility in designing and positioning eyeholes. This also provided flexibility in positioning the Skope Clip-On Camera NMR field probes. The performance of the dipoles was also simulated in CST Microwave Studio (CST) to determine B_1^+ efficiency and SAR levels.

Receive Coil

The receive coil consisted of 32 loop elements (**Figure 9 e), g**) ranging in diameter from 6 to 12 cm. Eight Rx elements were placed on each of the posterior, left and right components of the receive housing. Seven were placed on the anterior component and one element was placed on the superior component. Elements on each piece of the former were geometrically decoupled to reduce inductive coupling. However, due to the adjustable nature of the receive coil, adjacent elements on separate housing components could not be completely geometrically decoupled. At the largest receive housing size, the overlap between adjacent elements on separate housing components was 18 mm. At the smallest housing size, the overlap was approximately 32 mm. Elements were tuned to 297.2 MHz using a variable capacitor (EW Electronics SGC3S060NM) and matched to the 50 Ω input of the preamplifiers using a fixed value capacitor (American Technical Ceramics).

Three safety factors were integrated into the design of the receive loop circuitry: active detuning, passive detuning, and fuses. Active detuning (**Figure 9, d**) was achieved using a parallel-resonant LC circuit topology, which was activated by forward biasing a PIN Diode (Macom MA4P7470F-1072T). Passive detuning (**Figure 9, c**) was achieved using a similar parallel-resonant LC circuit and a cross-diode (MicroSemi UMX9989-AP). As a final precaution, low-loss MR compatible fuses (315mA, Conrac) were integrated into each receive element.

Receive elements were connected to WMM7RP preamplifiers (WanTCom) via coaxial cables. Cable traps were placed at increments of $\lambda/10$ along the coaxial cables to reduce common-mode currents. Coaxial cables and cable traps were fastened to the receive housing to reduce vibrations. The receive loops were further preamplifier decoupled by introducing a π network phase shift circuit at the input of each preamplifier (**Figure 9, b**). Cross diodes (MicroSemi UMX9989-AP) were placed across each preamplifier input port and ground in order to protect the preamplifier from excessive current. The output of the preamplifiers was connected via coaxial cables to a TIM Connector plug (ODU-MAC) for interfacing with the 7 T MRI Scanner.

Field Probes

A commercial field monitoring system, the Skope Clip-On Camera, was integrated with the coil housing. The Clip-On Camera system consisted of 16 ^{19}F based NMR field probes.

Proper positioning of the NMR field probes on the coil housing was important for ensuring optimal probe and coil performance. Theoretically, the ideal arrangement consists of probes placed equidistantly along the surface of a sphere.¹⁸ However, such an arrangement was not feasible given the constraints of the dipole placement on the Tx coil. In similar coil systems, NMR probes are typically placed between the transmit and receive housing.^{13,15,18} Such an arrangement was also not ideal for our coil since there was limited space between the transmit and receive formers. As such, in our work, all probes were placed on the outer surface of the transmit former between dipole elements. The exact positioning of the probes was based on the work of Duerst et al., in which the probes are placed on the outside surface of a cylindrical receive former and arranged in four parallel concentric rings offset by 45° .¹³ These initial positions were then adjusted iteratively to ensure that probes were not placed near current carrying conductors to mitigate coupling between the probes and coil. Once positions were finalized, the probes were fixed to the coil using Velcro tape, which allowed for easy removal and adjustment of the probes, if required. Once all the probes were integrated with the coil, the transmit elements were retuned and rematched to compensate for any changes resulting from interactions between the probes and dipole elements. The Skope Probes were connected to a dedicated spectrometer (Skope Magnetic Resonance Technologies). The probe cables were zip-tied into groups of four and fed through floating cable traps to suppress common mode currents.

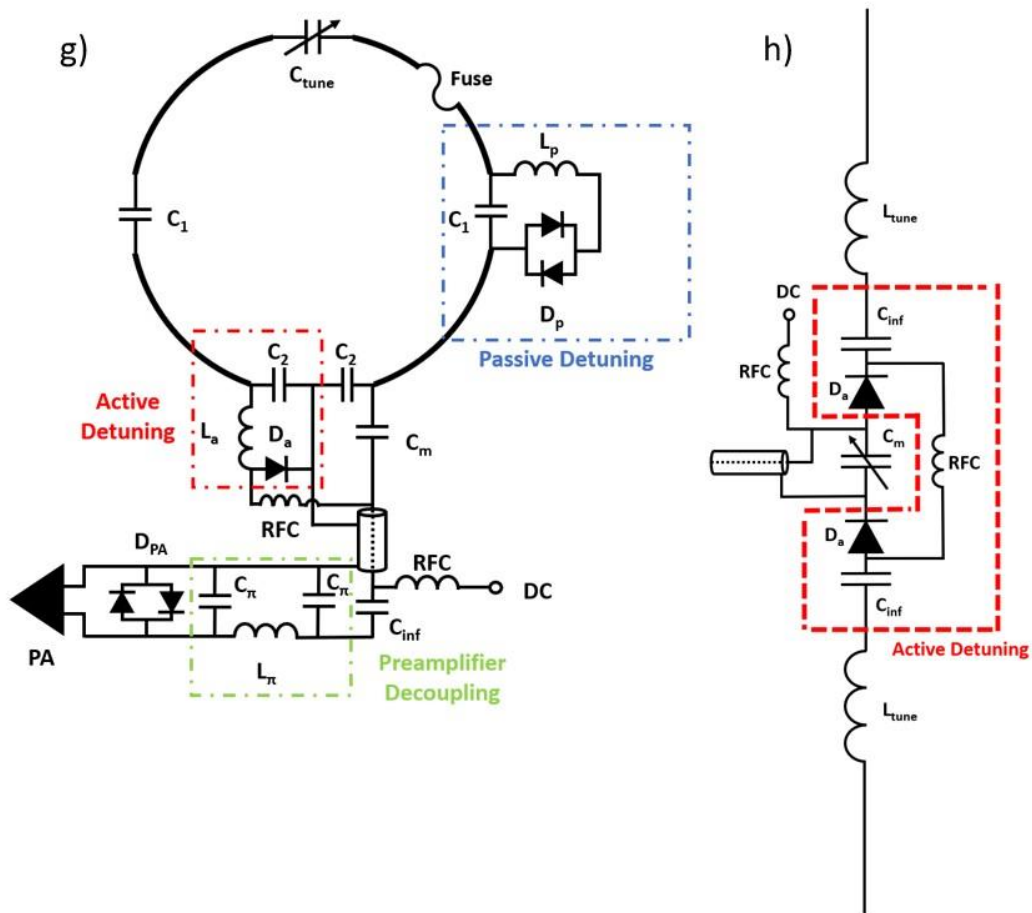
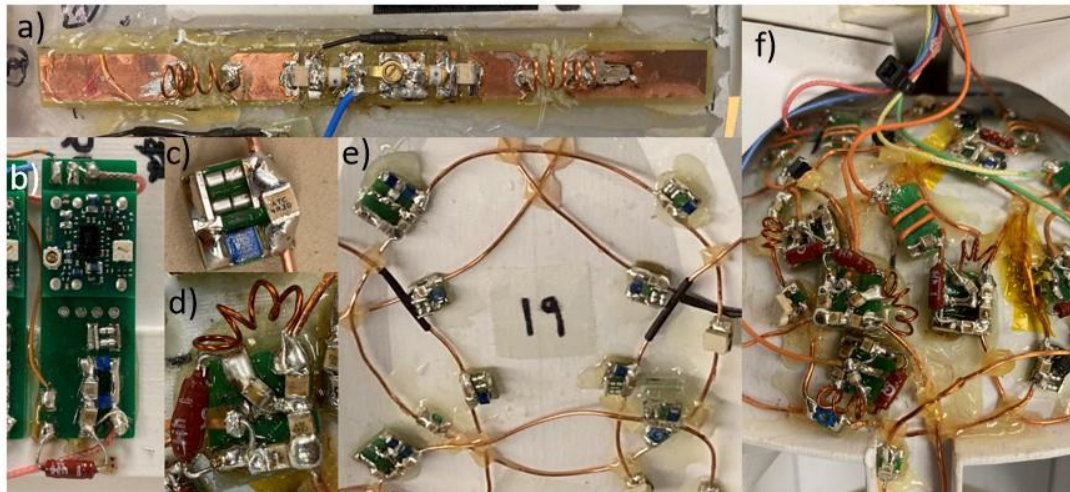


Figure 9: Electrical circuit diagrams and images of: a) transmit dipole, b) preamplifier interface board, c) passive detuning circuit, d) active detuning circuit, matching circuit and loop output, e) receive loop, f) receive loops, cabling and cable traps, g) receive loop circuit diagram showing passive detuning, active detuning and preamplifier decoupling circuits, and h) transmit dipole circuit with active detuning.

Coil Performance and Imaging

Imaging was performed using the Siemens Terra 7 T MRI system (Siemens Healthineers) at The Montreal Neurological Institute of McGill University, in Montreal, Quebec, Canada. All human imaging was performed in accordance with the McGill Ethics Review Board.

Receive Coil Performance

Receive elements were tuned and matched with each individual piece of the receive former loaded with an $\text{NiSO}_4 \times 6\text{H}_2\text{O}$ doped water phantom (12 cm diameter, Siemens Healthineers). Active detuning was measured at both the largest and smallest dimensions of the Rx coil using a single-loop probe. Preamplifier decoupling was measured at the largest size of the coil. Q-factor measurements for two receive elements meant to represent the largest and smallest elements in the array were also performed using a double-loop probe, with the $\text{NiSO}_4 \times 6\text{H}_2\text{O}$ doped water phantom was used as the load.

Heating of the Rx coil array components was assessed using an intensive RF FID pulse sequence (acquisition time of 10 minutes, 100% SAR). During the heating test, the temperature of the inside surface of the Rx former was measured with an infrared camera.

The performance of the receive coil was evaluated in four different configurations: 1) the largest coil setting without field probes, 2) at the largest setting with field probes, 3) the coil's smallest setting without field probes, and 4) at the smallest setting with field probes. Noise correlation matrices were generated for each configuration from noise-only acquisitions. The SNR performance of each coil configuration was evaluated by generating SNR maps using the covariance weighted root sum-of-squares image reconstruction (RSS-COV) technique.²⁴ SNR maps relied on standard 2D gradient echo (GRE) images with and without an RF pulse (matrix size: 256×256 , voxel size: $1 \times 1 \times 5 \text{ mm}^3$, slice gap: 10mm, number of slices: 18, TE: 2.72 ms, TR: 140 ms, flip angle: 15° , BW: 500 Hz/Px, number of averages: 1).

In vivo 2D spoiled gradient echo images of a 33-year-old healthy male subject were acquired with the pediatric coil at its largest setting and with the commercial 8Tx/32Rx pTx Nova Medical coil (matrix size: 128×128 , FOV: $300 \times 300 \text{ mm}^2$, TE: 10 ms, TR: 100ms, BW: 260 Hz/Px, FA: 25° , Slices: 1). This was done in order to a) demonstrate the ability of the pediatric coil to generate high quality in vivo images, and b) to compare the performance of the pediatric and commercial coil for in vivo imaging.

Transmit Coil Performance

Transmit coil performance was initially assessed in CST Microwave studio by simulating an individual dipole element as a perfect electrical conductor (PEC). The tuning and matching of the dipole were optimized by adjusting the values of two tuning inductors and a match capacitor. Once optimized, the same dipole design was repeated to form the full 8-channel pTx coil in CST. Each dipole was then retuned and rematched numerically to compensate for effects caused by inter-element coupling. The performance of the Tx coil was then simulated using CST to evaluate B_1^+ efficiency and SAR.

The CST simulations were performed for three voxel-based models: (1) a phantom model meant to mimic the $\text{NiSO}_4 \times 6\text{H}_2\text{O}$ doped water phantom used in both lab bench and imaging experiments, (2) a pediatric head model of a 7-year-old female subject (the CST “Child” model, height: 115 cm, weight: 21.7 kg), and (3) an adult head model of a 38-year-old male subject (the CST “Gustav” model, height: 176 cm, weight 69 kg). These simulations used the circularly polarized (CP^+) mode of the transmit coil. SAR simulations were performed in the pediatric model to assess the safety of the coil in multiple different parallel transmit coil combinations. This information was then used to set a safety factor in the coil file.²⁵

The transmit coil was tuned and matched while loaded with the $\text{NiSO}_4 \times 6\text{H}_2\text{O}$ doped water phantom. This was carried out at the isocenter of the bore of a decommissioned 1.5 T SONATA MRI scanner (Siemens Healthineers) to approximate the conditions of the 7 T scanner bore. Active detuning of the transmit elements was measured on the lab bench using a single loop probe. The scattering parameters (S-parameters) of the Tx coil with and without NMR probes and at both the largest and smallest sizes of the Rx coil were measured when loaded with the $\text{NiSO}_4 \times 6\text{H}_2\text{O}$ doped water phantom using the MRI scanner’s directional couplers. S-parameters were measured again after retuning and rematching the Tx coil to compensate for integration of the probes. B_1^+ field maps were generated using the scanner’s proprietary B_1^+ mapping sequence (matrix size: 64×64 , voxel size: $4 \times 4 \times 4 \text{ mm}^3$, slice gap: 4 mm, number of slices: 24, TE: 1.72 ms, TR: 4000 ms, flip angle: 10° , BW: 490 Hz/Px, number of averages: 1, GRAPPA acceleration factor: 2, reference phase encode lines: 16). The B_1^+ efficiency and phase of the individual channels of the Tx coil were generated using a flip-angle mapping sequence (matrix size: 100×96 , voxel size: $2 \times 2 \times 3$

mm³, number of slices: 45, TE: 2.39 ms, TR: 15020 ms, flip angle: 10°, BW: 250 Hz/Px, number of averages: 1, GRAPPA acceleration factor: 2, reference phase encode lines: 16).

Field Probe Performance

Free induction decay (FID) curves of the NMR field probes were measured at the largest and smallest size of the receive coil housing and compared to corresponding FIDs recorded on the Skope manufacturer-provided scaffold (i.e., the optimal probe arrangement). The goal of this evaluation was to analyze how FID signal lifetime was affected by integration into our custom coil. For measurements on the scaffold, the scanner's "tune-up" B₀ shim setting was used. B₀ shimming was performed over the entire length of the phantom.

The NMR field probes were used to monitor field dynamics for a 2D EPI sequence (matrix size: 120 × 120, voxel size: 2 × 2 × 3.8 mm³, slice gap: 3.8 mm, number of slices: 32, TE: 39 ms, TR: 3500 ms, flip angle: 90°, BW: 1984 Hz/Px, number of averages: 1, accel. mode: GRAPPA, accel. factor: 2, reference phase encode lines: 24). Based on the field probe measurements, MRI magnitude images of the phantom were reconstructed with the nominal k-space trajectories, as well as with the trajectories as determined by the Skope-measured field dynamics using the expanded signal model method.²⁶ Image correction and reconstruction was performed offline using in-house developed MATLAB software.²⁷

Results

Transmit Coil

After preliminary tuning and matching of the transmit coil, mean reflection at the input of the transmit coil elements was -31 dB, with a worst-case reflection of -22 dB in channel 3. The mean coupling coefficient between individual transmit elements was -24 dB. The worst-case coupling was -11 dB between channels 7 and 8. Active detuning provided a mean isolation of 14 dB between the transmit and receive elements. The minimum level of isolation achieved was 10 dB in channels 1 and 6. Cable traps were shown to be effective in limiting common-mode currents, as no shift in the resonance peak of the transmit elements was observed upon manipulation of the transmit cabling.

Transmit efficiency and SAR simulation results from CST are shown in **Figure 10**. **Figure 10** also includes experimentally generated B_1^+ efficiency maps acquired in both the phantom and in a healthy adult human subject. **Figure 11** shows B_1^+ efficiency maps for individual Tx channels measured experimentally in the phantom at the largest and smallest size of the Rx former, with and without field probes, as well as B_1^+ magnitude and phase maps measured experimentally in vivo.

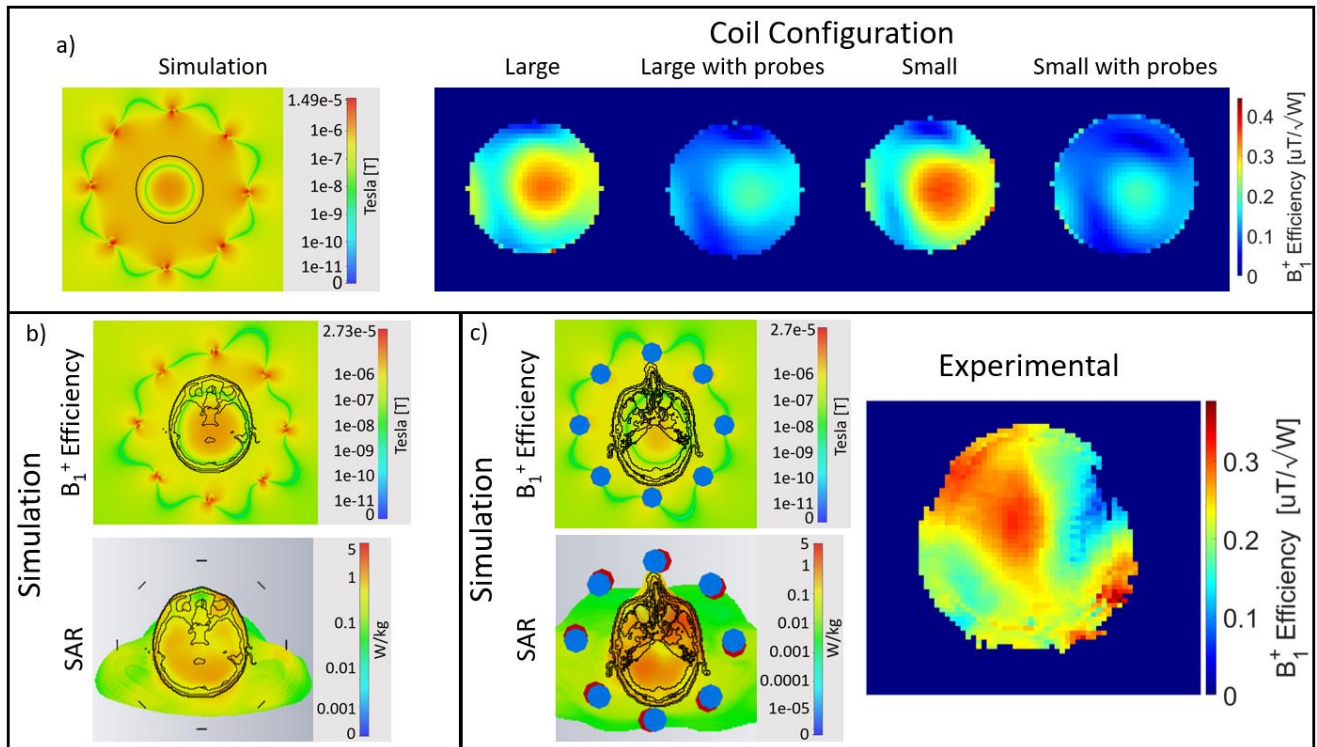


Figure 10: a) Simulated B_1^+ map in phantom and experimental B_1^+ efficiency map for all pediatric coil configurations (from left to right: largest coil size, largest coil size with integrated field probes, smallest coil size, smallest coil size with field probes), b) Simulated B_1^+ efficiency and SAR maps in pediatric head voxel model and c) simulated B_1^+ efficiency and SAR maps in adult head voxel model and experimental B_1^+ efficiency map.

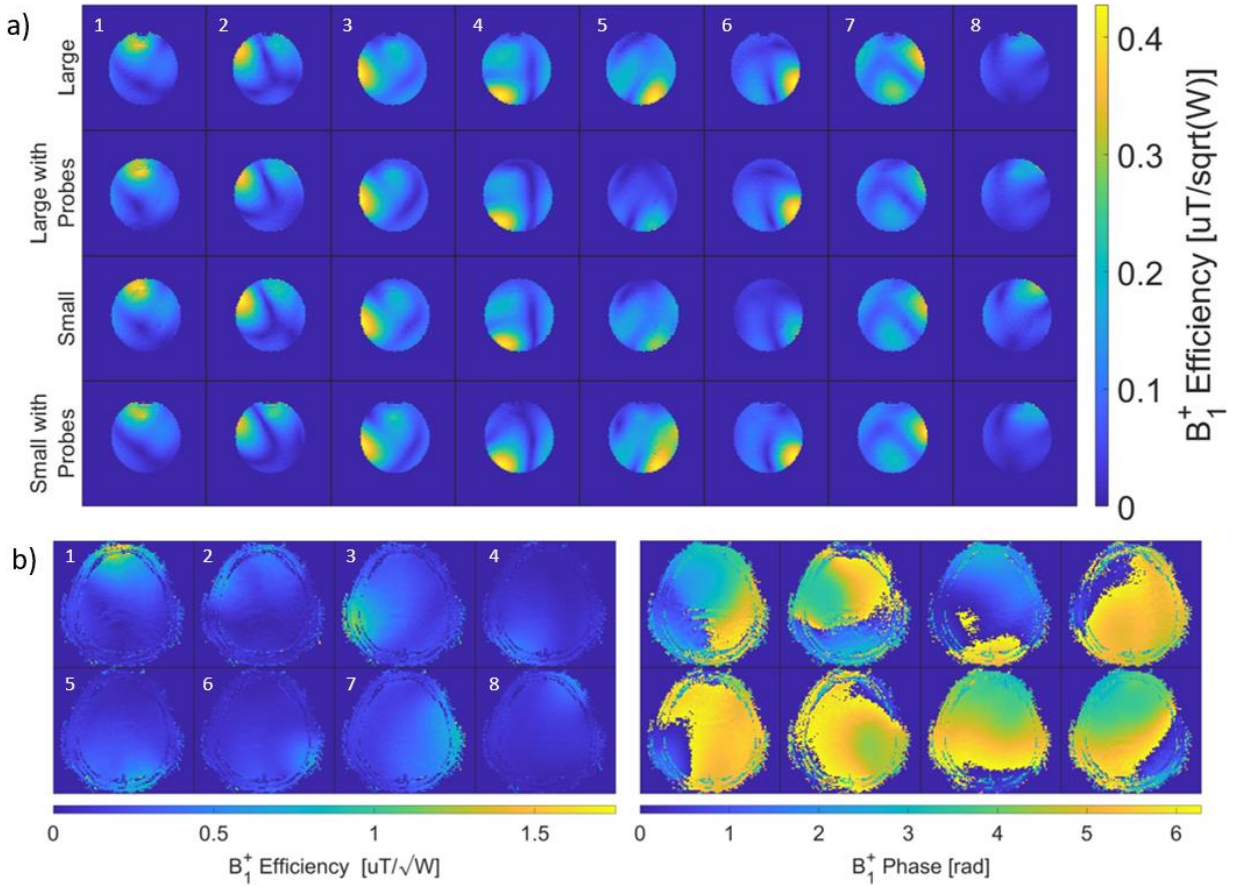


Figure 11: a) B_1^+ efficiency maps of individual channels measured in the phantom at the largest and smallest size of the receive coil, with and without probes, and b) B_1^+ efficiency and phase maps of individual channels measured in vivo, performed at the largest size of the receive former.

The simulated B_1^+ efficiency at the center of the phantom was $1.2 \frac{\mu T}{\sqrt{W}}$, and maximum 10 g SAR per accepted power was 0.75 kg^{-1} . The experimentally measured B_1^+ efficiency was 0.18, 0.11, 0.19 and $0.10 \frac{\mu T}{\sqrt{W}}$ for the large coil, large coil with integrated probes, small coil, and small coil with integrated probes, respectively. In the pediatric model, B_1^+ efficiency at the center of the brain was $1.18 \frac{\mu T}{\sqrt{W}}$, and maximum 10 g SAR over accepted power was 0.87 kg^{-1} . SAR simulations in the adult head model demonstrated a maximum 10 g SAR over accepted power of 1.13 kg^{-1} . The simulated B_1^+ efficiency at the center of the adult brain model was $0.95 \frac{\mu T}{\sqrt{W}}$. The experimentally determined B_1^+ efficiency at the center of the brain was $0.25 \frac{\mu T}{\sqrt{W}}$. B_1^+ efficiency maps generated

for individual transmit channel elements demonstrated that all channels contributed to the overall B_1^+ field. For the in vivo case, the B_1^+ efficiency is shown to be highest in the skull.

Scattering matrix parameters for all coil configurations, with and without integrated field probes, are given in **Figure 12**, along with a table summarizing the key results.

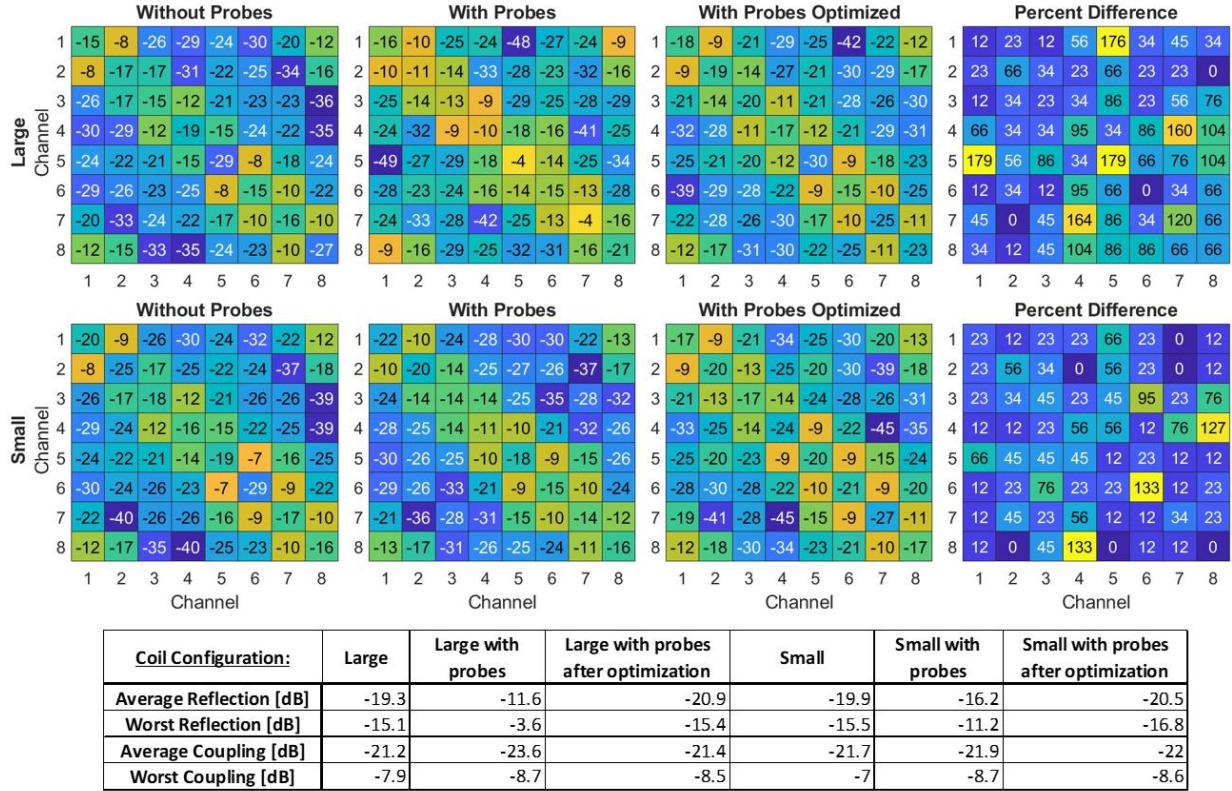


Figure 12: Tx coil scattering matrix (S -matrix) parameters and table of summarized key results. Difference maps for each coil configuration were calculated from S -parameters measured directly before and directly after probe integration.

At both the largest and smallest size of the receive coil, the mean and maximum reflection increased with the integration of the NMR field probes. After retuning and rematching of the transmit coil elements to compensate for the integration of the probes, the mean and maximum reflection were decreased below -20 dB and -15 dB, respectively. Though, globally, coupling remained relatively unchanged between coil configurations, interelement coupling can be seen to vary in the difference maps. The mean and maximum percent difference in interelement coupling before and after probe integration for the large coil dimension was 56.7% and 179% (channels 1-5) respectively. Mean change in reflection coefficients was 73%, with a maximum change of 179%

(channel 5) for the coil at the large size with and without probes. For the small size, mean and maximum percent difference in coupling was 32.1% and 133% (channels 4-8) respectively. Mean change in the reflection coefficients was 44%, with a maximum change of 133 % (channel 6).

Receive Coil

Each component of the Rx array was individually tuned and matched. The mean and maximum reflection coefficients measured in this way were -22 dB and -14 dB, respectively. Geometric decoupling, carried out for each individual part of the adjustable Rx former, yielded a mean isolation between elements of -16 dB and a maximum coupling of -10 dB. At the largest size of the adjustable receive former, active detuning of the Rx array achieved a mean isolation of 17 dB and a worst-case isolation of 9 dB. At the smallest size of the receive housing, active detuning yielded a mean isolation of 18 dB and a worst-case isolation of 8 dB. In both coil configurations, the worst-case active detuning performance occurred for element 32, which was located at the top of the head. All other Rx channels exhibited excellent active detuning with isolation greater than 10 dB. The Q ratio for the representative small Rx element was 6.3 ($Q_{\text{unloaded}} = 82$, $Q_{\text{loaded}} = 13$). The Q ratio for the representative large Rx element was 7.2 ($Q_{\text{unloaded}} = 72$, $Q_{\text{loaded}} = 10$). No appreciable heating was observed during operating of the coil for phantom imaging, with temperature changes well below 2°C and a maximum recorded temperature below 30°C.

Noise correlation matrices for the coil at its largest and smallest size, with and without field probes, are given in **Figure 13**.

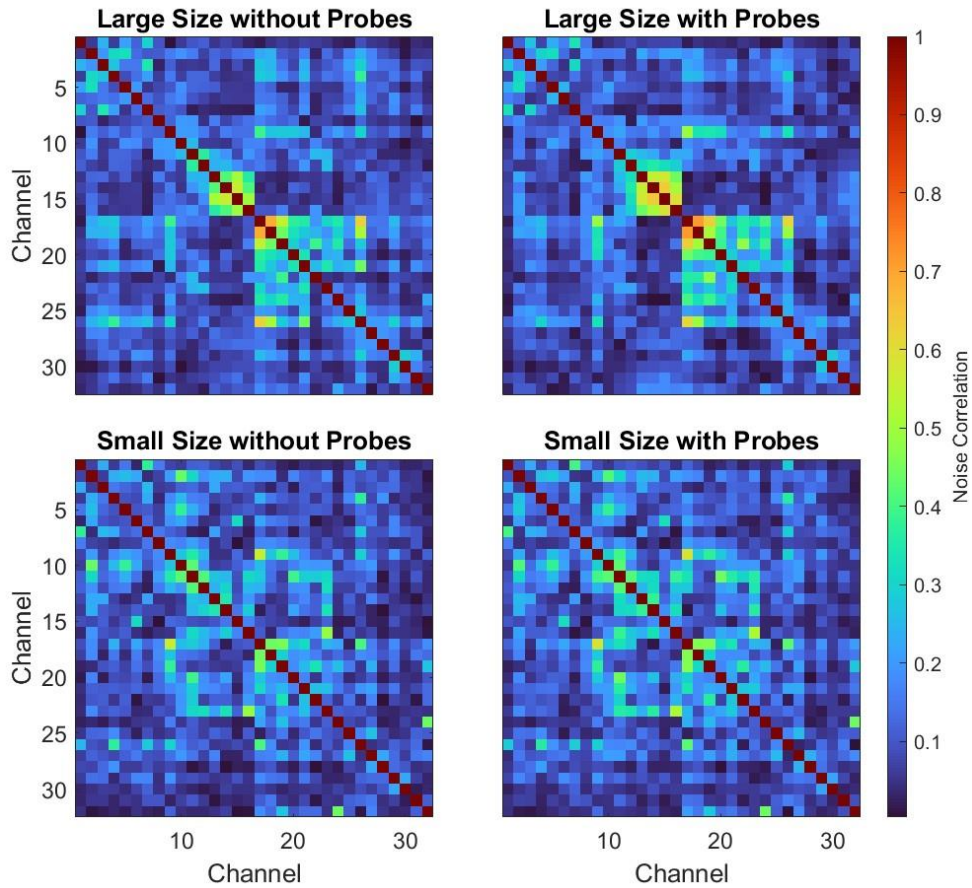


Figure 13: Noise correlation matrices for the Rx coil array with the former at its largest and smallest size, with and without NMR field probes.

At the largest size of the Rx former, the mean noise correlation was 12.7%. The largest value of the noise correlation was 68.5% (channels 17-18). These measurements were carried out before field probe integration. The mean noise correlation increased slightly upon integration of field probes, with a mean noise correlation value of 12.9%. The maximum noise correlation increased to 71.3% (channels 17-18) upon integration of the probes. At the smallest size of the receive former, without NMR field probes, the mean noise correlation was 12.2% and the maximum noise correlation was 55.7% (channels 9-17). After integrating the probes, the mean and maximum noise correlation values were 12.9% and 58.4% (channels 9-17), respectively.

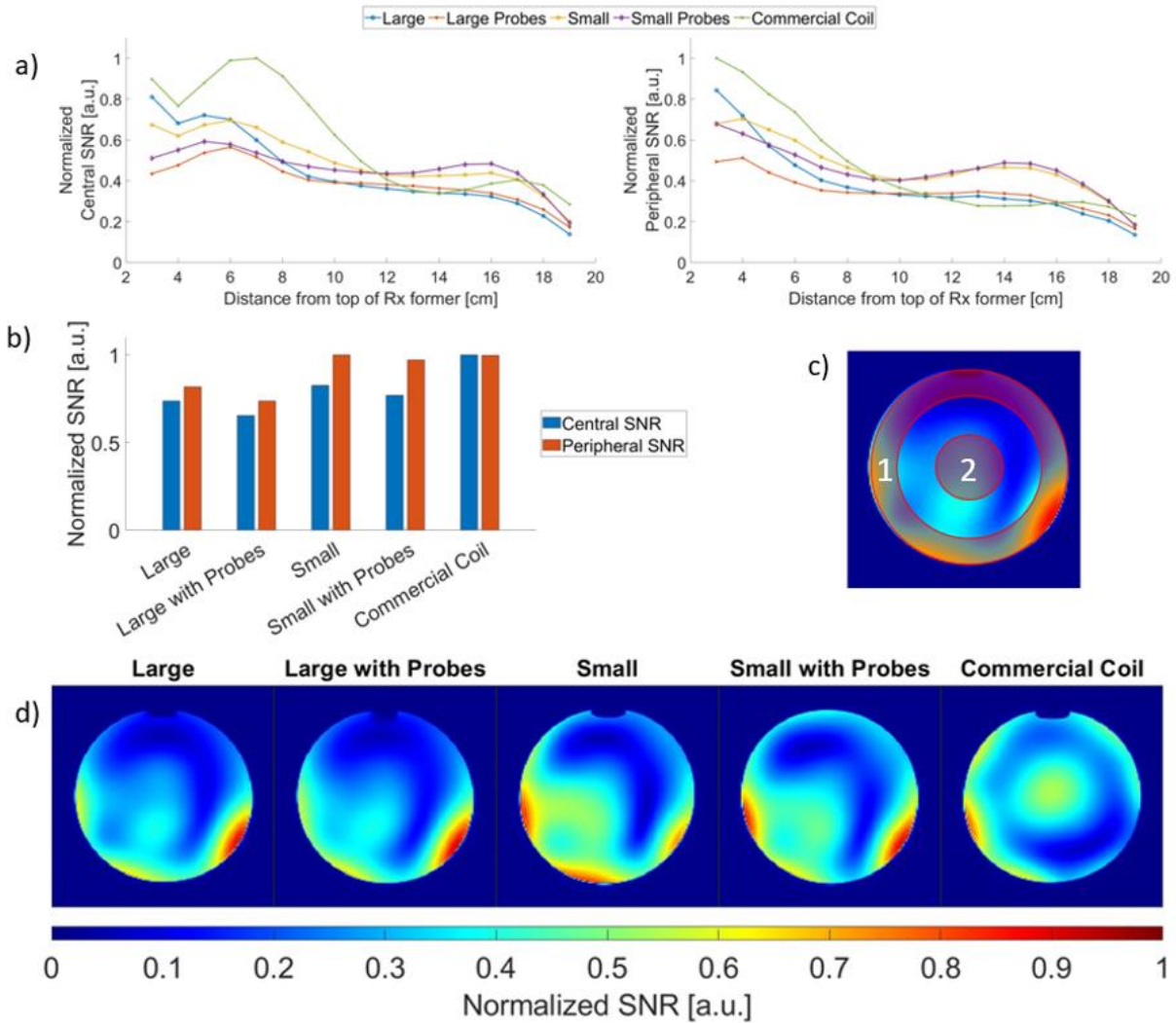


Figure 14: SNR measured in the phantom: a) average central SNR throughout the sensitive region of the coil, b) average peripheral SNR throughout the sensitive region of the coil, c) average central and peripheral SNR over the whole sensitive region of the coil, d) regions of interest (ROIs) used to calculate peripheral (1) and central (2) SNR, and e) SNR map of a representative slice of the phantom.

Phantom SNR maps for a representative slice near the center of the brain are shown in **Figure 14**. The line plots at the top of **Figure 14** show the distribution of average central and peripheral SNR along the length of the Rx coil for each coil configuration. Central SNR was determined by taking the mean value of a 40mm diameter circular ROI at the center of each slice. Peripheral SNR was determined using a 15 mm thick donut-shaped ROI with an outer radius equal to the radius of the phantom.

Adjusting the size of the coil to better fit the dimensions of the phantom yielded a 12% increase in central SNR and a 23% increase in peripheral SNR. However, integration of the probes led to a decrease in both peripheral and central SNR for both head former sizes. For example, for the largest coil size, average central SNR decreased by 11% and average peripheral SNR decreased by 10% with field probe integration. For the smallest coil size, average central SNR decreased by 7% and average peripheral SNR decreased by 3% with field probe integration.

The commercial Nova coil had the highest overall average normalized central SNR (normalized to 100%), followed by the Rx coil at its smallest size (82%), the Rx coil at its smallest size with integrated field probes (76%), the Rx coil at its largest size (73%) and the coil at its largest size with integrated field probes (65%). Average peripheral SNR of the small coil configuration (100%) was comparable to the peripheral SNR demonstrated by the commercial coil (100%). With the addition of the field probes, the average peripheral SNR of the small coil was reduced slightly to 97%. At the largest coil size, with and without probes, the peripheral SNR was 82% and 74% of the SNR of the commercial coil/small pediatric coil, respectively.

In vivo SNR maps for a representative slice near the center of the brain are shown in **Figure 15**. The Nova coil had higher peripheral and central SNR when measured in vivo for an adult subject. When normalized to the Nova coil, the pediatric coil demonstrated central and peripheral in vivo SNR of 58.2% and 56.5%, respectively.

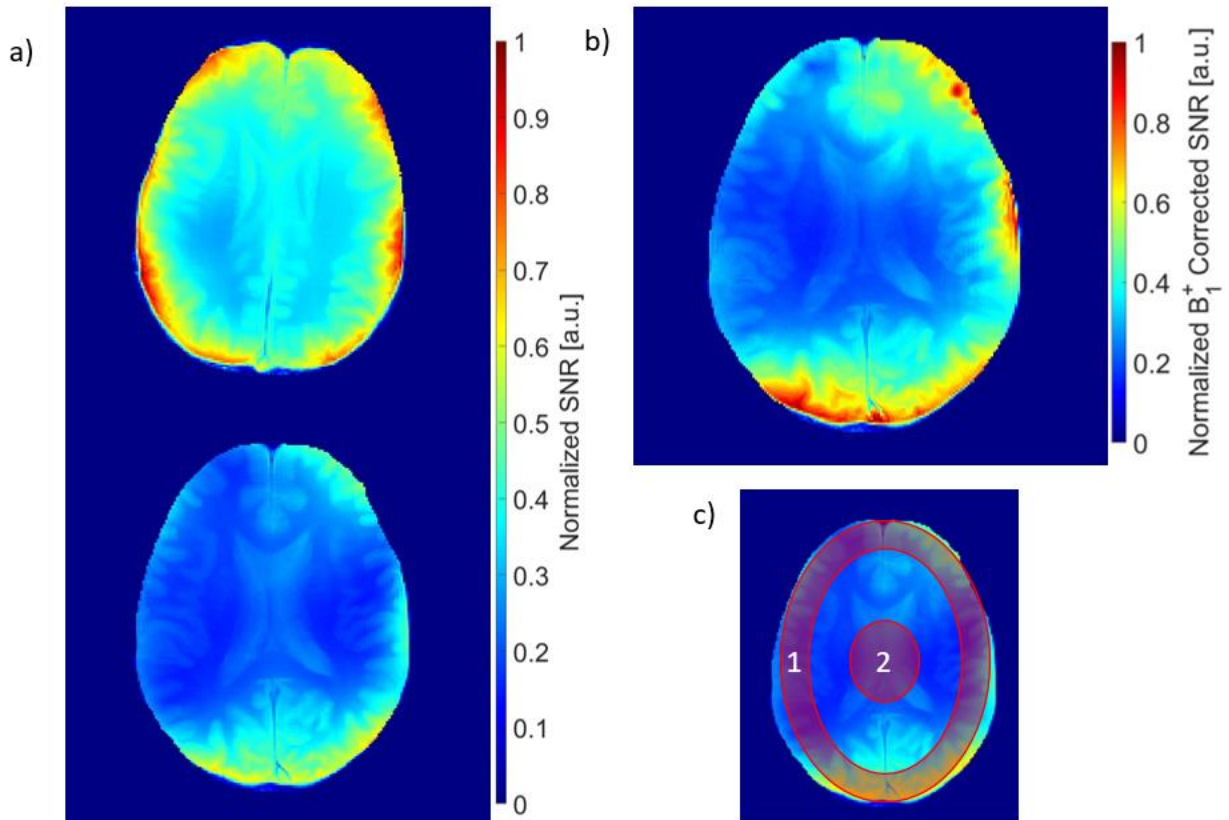


Figure 15: In vivo SNR maps: a) comparison of normalized SNR between the commercial Nova coil (top) and the pediatric coil (bottom), b) B_1^+ normalized in vivo SNR map generated using the pediatric coil, and c) ROIs used to calculate peripheral (1) and central (2) SNR.

NMR Probe Performance

The magnitude free induction decay signals of each probe measured on the manufacturer's scaffold and when integrated with the coil in its largest and smallest configuration are shown in **Figure 16**.

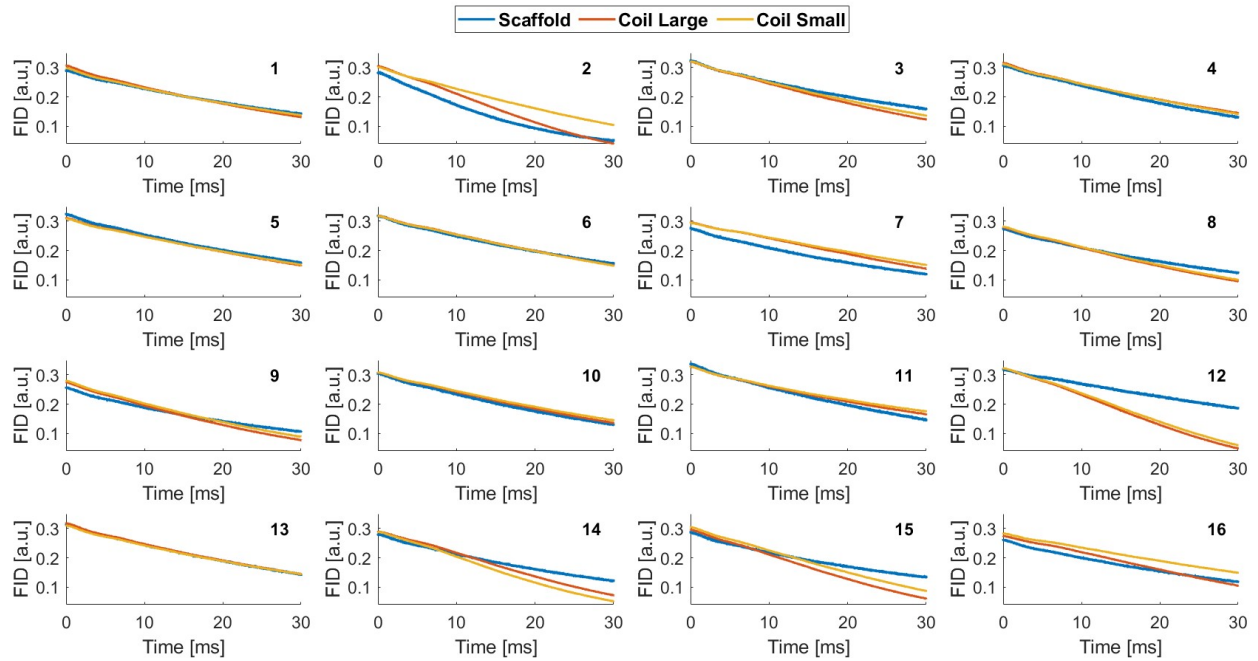


Figure 16: Magnitude free induction decay signals measured on the Skope scaffold, large coil configuration and small coil configuration using Skope probes 1-16 (starting left to right, top-down).

The mean normalized FID signal magnitudes, recorded 30 ms after radiofrequency excitation of the field probes, were 43%, 40% and 36% on the scaffold, small coil, and large coil, respectively. Corresponding minimum signal values after 30 ms were 17%, 18% and 13% on the scaffold, small coil, and large coil, respectively.

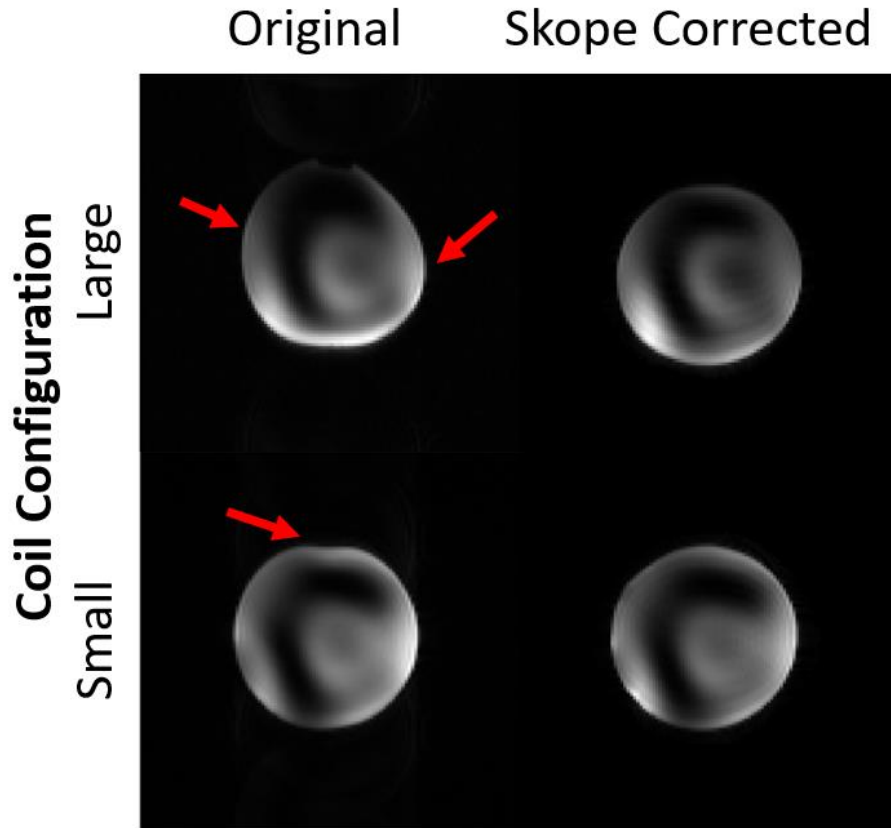


Figure 17: 2D EPI phantom images reconstructed without (original) and with (Skope corrected) dynamic field correction. Red arrows indicate visually apparent distortions.

2D EPI phantom images reconstructed with and without Skope correction are shown in **Figure 17**. Visually apparent distortions are identified by red arrows. When integrated with the coil, the probes were capable of estimating dynamic magnetic field fluctuations up to 2nd order. Implementation of 2nd order spherical harmonic correction of acquired k-space data enabled the elimination of geometric distortions.

Pediatric Coil

Nova Medical Coil

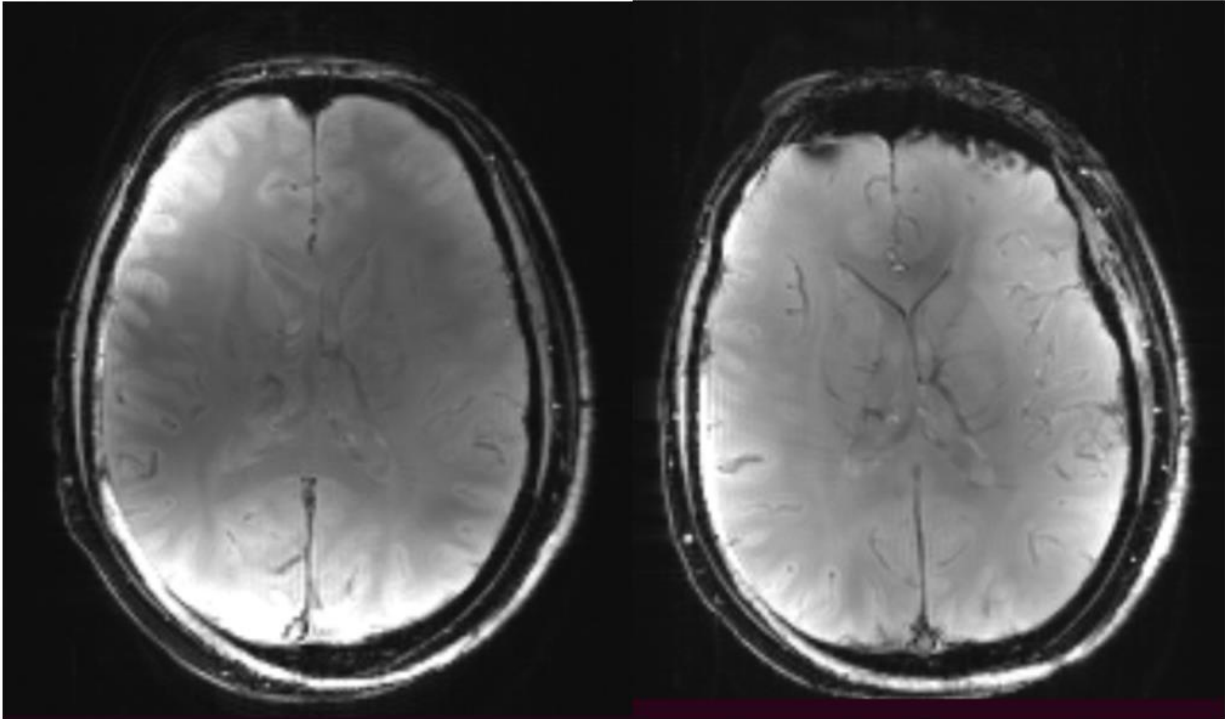


Figure 18: In vivo 2D spoiled GRE image of an adult human taken with the pediatric coil adjusted to its maximum size (left) and the Nova coil (right).

Figure 18 shows in vivo 2D spoiled gradient echo images of a 33-year-old, healthy adult human subject. The image in the left column of **Figure 18** was acquired using the pediatric coil at its largest size. The image in the right column of **Figure 18** is taken from the same subject with the Nova coil.

Discussion

In this work, we presented the design, construction, and performance of a size-adaptive 7 T pediatric head coil with integrated NMR field probes. Our primary goal was to develop a conformal coil that could safely be applied to carry out 7 T brain imaging of pediatric subjects aged 4-9 years, with weights under 30 kg. We simulated the SAR performance of the coil with CST using a pediatric head/body model and also developed pediatric-specific, Virtual Observation Point (VOP)-based SAR safety factors.

Compared to the Nova commercial head coil, our pediatric coil exhibited more uniform SNR over the entire length of the Rx array in the phantom imaging experiments. This was true for both the large and small sizes of the coil. ROI-derived central and peripheral SNR at the top of the sensitive region of the Rx former (i.e., in the region corresponding to the top of brain) were higher for the Nova coil by 34% and 18%, respectively, compared to the coil at its smallest size. Near the bottom of the sensitive region of the receive coil (i.e., near the bottom of the brain), the pediatric coil in its smallest size demonstrated an improvement in ROI-derived central and peripheral SNR of 3% and 37%, respectively, compared to the Nova coil. The B_1^+ corrected in vivo SNR map produced using our coil shows evidence of some residual B_1^+ excitation field effects. In future, we will aim to improve the B_1^+ efficiency of our pediatric coil further through optimization of the default B_1^+ field and the implementation of pTx pulse design to further enhance SNR, particularly in the superior regions of the brain.

The Rx noise correlation matrices for our phased array demonstrated that SNR could also be improved through more rigorous decoupling of the receive channels, particularly channels 17 and 18. The improvement in central and peripheral SNR (12% and 23%, respectively) observed when the coil was adjusted to better fit the dimensions of the phantom also demonstrated the benefit of implementing a size-adaptive Rx former design.

The performance of the coil was impacted by the integration of the NMR field probes, with observed reductions in SNR and B_1^+ efficiency. These changes were less severe when the coil was in its smallest size, i.e., when the receive elements were further away from the NMR field probes. This indicates that retuning and rematching the receive elements after integrating the probes, as was performed by Gilbert et al.,¹⁵ is likely important for maintaining high coil performance.

The coil did not substantially alter the performance of the NMR field probes, particularly at the smallest size of the receive coil. The probe FID lifetimes were comparable to the lifetimes measured on the manufacturer's scaffold. Retrospective correction of 2D EPI data using Skope-measured k-space trajectories reduced the impact of distortion artifacts. The field probe configuration we applied with our coil enabled up to 2nd order spherical harmonics estimation and correction of field dynamics. This is less than the 3rd order correction possible with the probes positioned on the manufacturer's scaffold but is in line with similar integrated coil/probe systems

and is a result of the geometric constraints imposed on the positioning of the probes when integrated with an RF coil.¹⁵

Acknowledgements

We would like to thank Paul Weavers and Cameron Cushing from Skope Magnetic Resonance Technologies for their helpful insights. Funding support for the present work was provided by the Transforming Autism Care Consortium, the Natural Sciences and Engineering Research Council of Canada and the McGill Healthy Brains Healthy Lives Initiative.

References

1. Copeland A, Silver E, Korja R, et al. Infant and Child MRI: A Review of Scanning Procedures. *Front Neurosci.* 2021;15:666020. doi:10.3389/fnins.2021.666020
2. Dagia C, Ditchfield M. 3T MRI in paediatrics: Challenges and clinical applications. *European Journal of Radiology.* 2008;68(2):309-319. doi:10.1016/j.ejrad.2008.05.019
3. Barkovich MJ, Li Y, Desikan RS, Barkovich AJ, Xu D. Challenges in pediatric neuroimaging. *NeuroImage.* 2019;185:793-801. doi:10.1016/j.neuroimage.2018.04.044
4. Barkovich MJ, Xu D, Desikan RS, Williams C, Barkovich AJ. Pediatric neuro MRI: tricks to minimize sedation. *Pediatr Radiol.* 2018;48(1):50-55. doi:10.1007/s00247-017-3785-1
5. Zaitsev M, Maclaren Julian, Herbst M. Motion Artefacts in MRI: a Complex Problem with Many Partial Solutions. *J Magn Reson Imaging.* 2015;42(4):887-901. doi:10.1002/jmri.24850
6. Malik SJ, Hand JW, Carmichael DW, Hajnal JV. Evaluation of specific absorption rate and heating in children exposed to a 7T MRI head coil. *Magnetic Resonance in Med.* 2022;88(3):1434-1449. doi:10.1002/mrm.29283
7. Rollins JD, Collins JS, Holden KR. United States Head Circumference Growth Reference Charts: Birth to 21 Years. *The Journal of Pediatrics.* 2010;156(6):907-913.e2. doi:10.1016/j.jpeds.2010.01.009
8. Gilbert KM, Nichols ES, Gati JS, Duerden EG. A radiofrequency coil for infants and toddlers. *NMR in Biomedicine.* 2023;36(8):e4928. doi:10.1002/nbm.4928
9. Ghotra A, Kosakowski HL, Takahashi A, et al. A size-adaptive 32-channel array coil for awake infant neuroimaging at 3 Tesla MRI. *Magnetic Resonance in Med.* 2021;86(3):1773-1785. doi:10.1002/mrm.28791
10. Lopez Rios N, Foias A, Lodygensky G, Dehaes M, Cohen-Adad J. Size-adaptable 13-channel receive array for brain MRI in human neonates at 3 T. *NMR in Biomedicine.* 2018;31(8):e3944. doi:10.1002/nbm.3944
11. Keil B, Alagappan V, Mareyam A, et al. Size-optimized 32-channel brain arrays for 3 T pediatric imaging: Pediatric Brain Arrays. *Magn Reson Med.* 2011;66(6):1777-1787. doi:10.1002/mrm.22961
12. Duerst Y, Wilm BJ, Wyss M, et al. Utility of real-time field control in T2*-Weighted head MRI at 7T. *Magnetic Resonance in Medicine.* 2016;76(2):430-439. doi:10.1002/mrm.25838
13. Duerst Y, Wilm BJ, Dietrich BE, et al. Real-time feedback for spatiotemporal field stabilization in MR systems. *Magnetic Resonance in Medicine.* 2015;73(2):884-893. doi:10.1002/mrm.25167

14. Kraff O, Fischer A, Nagel AM, Mönninghoff C, Ladd ME. MRI at 7 tesla and above: Demonstrated and potential capabilities: Capabilities of MRI at 7T and Above. *J Magn Reson Imaging*. 2015;41(1):13-33. doi:10.1002/jmri.24573
15. Gilbert KM, Dubovan PI, Gati JS, Menon RS, Baron CA. Integration of an RF coil and commercial field camera for ultrahigh-field MRI. *Magnetic Resonance in Med*. 2022;87(5):2551-2565. doi:10.1002/mrm.29130
16. Dietrich BE, Brunner DO, Wilm BJ, et al. A field camera for MR sequence monitoring and system analysis. *Magnetic Resonance in Medicine*. 2016;75(4):1831-1840. doi:10.1002/mrm.25770
17. Brunner DO, Dietrich BE, Çavuşoğlu M, et al. Concurrent recording of RF pulses and gradient fields - comprehensive field monitoring for MRI: Comprehensive Field Monitoring. *NMR Biomed*. 2016;29(9):1162-1172. doi:10.1002/nbm.3359
18. Barmet C, Zanche ND, Pruessmann KP. Spatiotemporal magnetic field monitoring for MR. *Magnetic Resonance in Medicine*. 2008;60(1):187-197. doi:10.1002/mrm.21603
19. Gross S, Barmet C, Dietrich BE, Brunner DO, Schmid T, Pruessmann KP. Dynamic nuclear magnetic resonance field sensing with part-per-trillion resolution. *Nat Commun*. 2016;7(1):13702. doi:10.1038/ncomms13702
20. Wilm BJ, Nagy Z, Barmet C, et al. Diffusion MRI with concurrent magnetic field monitoring: Diffusion MRI with Concurrent Magnetic Field Monitoring. *Magn Reson Med*. 2015;74(4):925-933. doi:10.1002/mrm.25827
21. Brunner D, Gross S, Schmid T, et al. Integration of field monitoring for neuroscientific applications - SNR, acceleration and image integrity. In: ; 2019. Accessed July 18, 2023. <https://cds.ismrm.org/protected/19MProceedings/PDFfiles/1046.html>
22. Deniz CM. Parallel Transmission for Ultrahigh Field MRI. *Topics in Magnetic Resonance Imaging*. 2019;28(3):159-171. doi:10.1097/RMR.000000000000204
23. Fagan AJ, Bitz AK, Björkman-Burtscher IM, Collins CM, Kimbrell V, Raaijmakers AJE. 7T MR Safety. *J Magn Reson Imaging*. 2021;53(2):333-346. doi:10.1002/jmri.27319
24. Kellman P, McVeigh ER. Image reconstruction in SNR units: A general method for SNR measurement†. *Magnetic Resonance in Med*. 2005;54(6):1439-1447. doi:10.1002/mrm.20713
25. Padormo F, Beqiri A, Hajnal JV, Malik SJ. Parallel transmission for ultrahigh-field imaging. *NMR in Biomedicine*. 2016;29(9):1145-1161. doi:10.1002/nbm.3313
26. Wilm BJ, Barmet C, Gross S, et al. Single-shot spiral imaging enabled by an expanded encoding model: D emonstration in diffusion MRI. *Magn Reson Med*. 2017;77(1):83-91. doi:10.1002/mrm.26493

27. Feizollah S, Tardif CL. High-resolution diffusion-weighted imaging at 7 Tesla: Single-shot readout trajectories and their impact on signal-to-noise ratio, spatial resolution and accuracy. *NeuroImage*. 2023;274:120159. doi:10.1016/j.neuroimage.2023.120159

Chapter 6 – Discussion and Conclusion

Pediatric neuroimaging can be impacted by subject motion and influenced by variations in head size during human neurodevelopment.^{2,21} Further, overall MRI signal quality is reduced when pediatric neuroimaging is conducted with a conventional, rigid adult-sized head coil. Recent research in pediatric array construction has attempted to address these challenges by implementing custom-made, size-adaptive coil formers for 3 T MRI.^{25–28} These coils are capable of conforming to a wide range of pediatric head shapes/sizes, reducing motion artifacts and better securing the subject's head. Size-adaptive coil designs also improve overall coil performance.

The specific aim of the present thesis was to build on the current research in size-adaptive pediatric coils by designing a size-adaptive pediatric head coil with integrated field monitoring capability for UHF, 7 T MRI. Our coil was motivated by the potential to leverage both reduced scan times and improved spatial resolution with 7 T MRI.

The addition of integrated field monitoring using the Skope Clip-On Camera system served to a) further assist in mitigating motion artifacts generated via bulk motion of the pediatric subject's head and b) partially correct geometric distortions caused by dynamic field fluctuations.

Due to SAR considerations, no commercial 7 T pediatric head coils exist for imaging human subjects below 30 kg. We sought to directly address this challenge through careful simulation, design and assembly of our coil. The following sections summarize the results of this thesis, as well as future directions focused on a final optimized 7 T pediatric coil design.

6.1 Discussion of Transmit Coil Results

Unlike lower field strength MRI systems, 7 T MRI scanners lack an integrated body coil. As a result, our design required development of a dedicated transmit coil for 7T MRI excitation. This constituted a significant difference between our coil and previous, size-adaptive arrays for 3 T MRI.^{25–28}

Our 7 T transmit coil was initially designed in two separate configurations. The first consisted of eight notched dipole elements mounted onto a cylindrical former, as described and presented in

Chapter 5. The second consisted of eight loop elements mounted onto a second, identical, cylindrical transmit former. The performance of these two different Tx coil configurations was then compared through (i) simulations in CST Microwave Studios (CST, Germany) and (ii) experimentally acquired phantom images. This preliminary performance evaluation was carried out at an early stage of the array design. As such, an early version of the Rx phased array, composed of an eight-channel subset of the full 32-channel Rx array arranged to cover the human visual cortex, was applied for measurements (**Figure 19**).⁵⁶

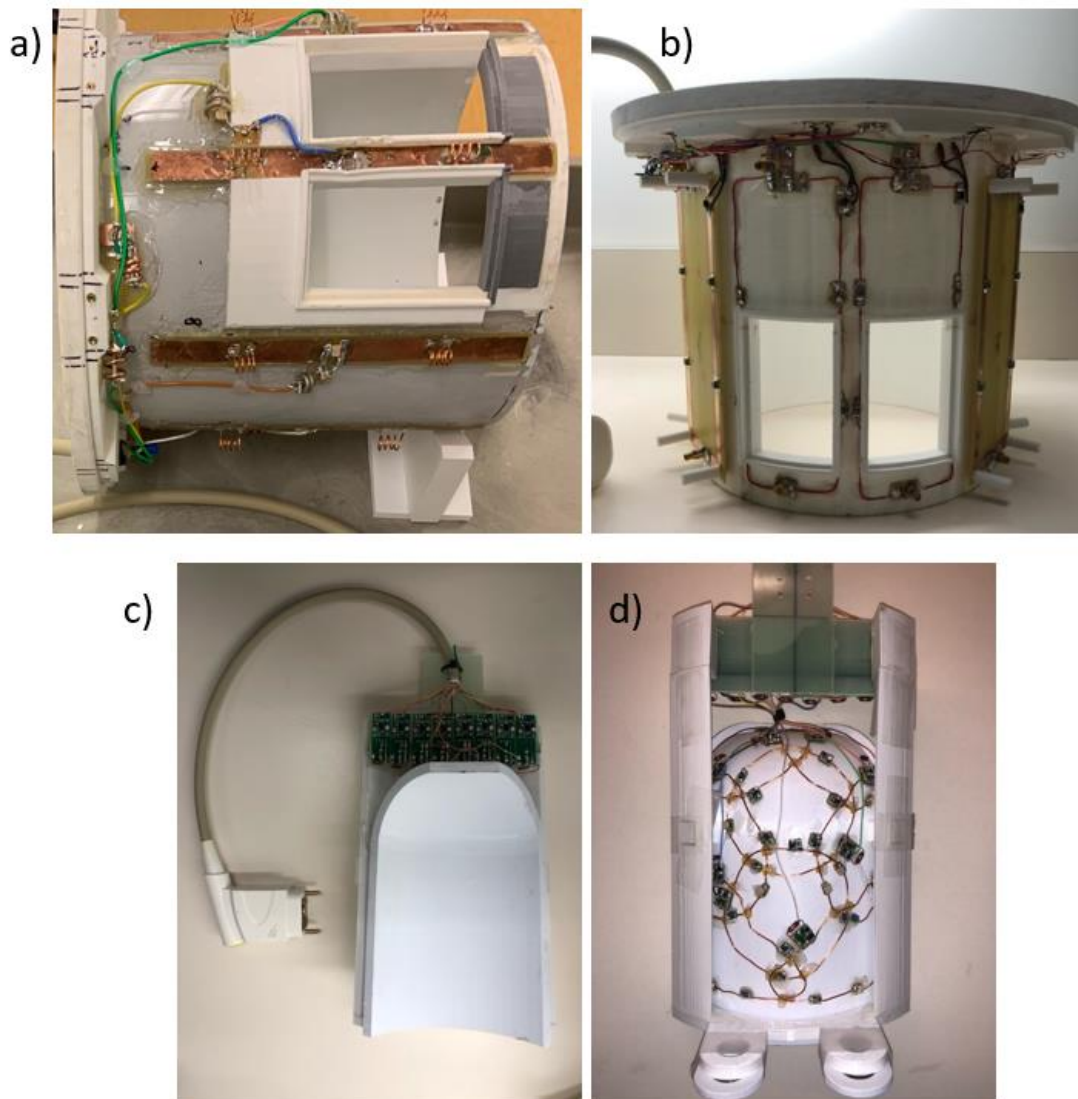


Figure 19: Transmit coil configurations evaluated for potential use with the size-adaptive pediatric head coil: a) eight-channel dipole pTx coil, b) eight-channel loop pTx coil, c) top view of eight-channel Rx coil used in comparing the dipole and loop pTx coils, and d) bottom view of eight-channel Rx coil, demonstrating loop element circuitry.

Both simulated and experimental results suggested that the dipole coil had superior B_1^+ efficiency (approximately 10% better than the loop coil), especially near the center of the phantom (or pediatric head voxel model, in simulation).⁵⁶ In simulation, the loop coil demonstrated improved SAR performance (10 g average SAR of 0.64 kg^{-1}) compared to the dipole coil (10 g average SAR of 0.87 kg^{-1}) by approximately 35%.⁵⁶ Ultimately, however, the dipole transmit coil was chosen for use in the full pediatric head coil due to its improved B_1^+ efficiency. The reduced footprint of the dipole elements also provided additional flexibility for positioning of NMR field probes.

The simulated SAR values for our dipole Tx coil are comparable to those measured in similar coil designs described in the literature. For instance, the 8Tx/32Rx 7 T adult head coil described by Clément et al. consisted of seven center-shortened dipole transmit elements and two loop transmit elements operating in quadrature and had a simulated 10 g average SAR of 0.81 Wkg^{-1} in an adult human head model (the Duke head model from Sim4Life).⁵⁷ There is only one existing, comparable simulation of a 7 T transmit array for pediatric use - pediatric SAR simulations of a 7 T, 16-rung birdcage transmit head coil were carried out by Malik et al. in 2022 with eight voxel-based human models aged 3, 5, 6, 8, 8, 11, 14, and 34 years old.²² Malik et al. sought to evaluate 7 T SAR across a range of pediatric subjects. Of the eight total models, five had weights under 30 kg.²² For each of these models, peak, spatial 10 g averaged power normalized SAR values were 0.517, 0.526, 0.446, 0.489, 0.474, 0.472, 0.515, and 0.448 kg^{-1} , respectively.²² This is slightly lower than the values determined for our dipole pTx coil. Nonetheless, the coil simulated by Malik et al. was a single channel transmit (sTx) coil, while our design functions using parallel transmission (pTx). Furthermore, this comparison does not take into consideration the B_1^+ efficiency of the coils, which also affects SAR.

The *simulated*, mean central B_1^+ efficiency of our dipole transmit coil measured in the $\text{NiSO}_4 \times 6\text{H}_2\text{O}$ doped water phantom voxel model was $1.2 \frac{\mu\text{T}}{\sqrt{\text{W}}}$. The B_1^+ efficiency of the transmit coil was also simulated for the CST Child brain and Gustav brain models. The mean central B_1^+ efficiency measured in these models was 1.18, and $0.95 \frac{\mu\text{T}}{\sqrt{\text{W}}}$, respectively. Experimental B_1^+ efficiency maps in the phantom were generated for the largest and smallest size of the Rx former with and without integrated field probes. Mean B_1^+ efficiencies measured at the center of the $\text{NiSO}_4 \times 6\text{H}_2\text{O}$ phantom for the large coil, large coil with probes, small coil and small coil with probes were 0.18,

0.11, 0.19 and $0.10 \frac{\mu T}{\sqrt{W}}$. The B_1^+ efficiency of the coil was also assessed experimentally *in vivo* for a 33-year-old adult male subject. Mean B_1^+ efficiency at the center of the brain was $0.25 \frac{\mu T}{\sqrt{W}}$.

The differences in simulated and experimentally determined B_1^+ efficiencies measured both in the phantom and *in vivo* are likely due to two factors. First, the simulated coil was modelled as a “lossless” system, i.e., using ideal lumped elements and perfect electrical conductors (PEC). As such, a decrease in B_1^+ efficiency is expected experimentally due to the inherent losses associated with real components and transmission lines. Second, our simulated coil was driven in the CP^+ mode. For the actual physical coil system applied for 7 T imaging, the phases and magnitudes of each excitation pulse are typically optimized. Though, experimentally using the 7 T human MRI system at McGill, some B_1^+ vector optimization was performed, the discrepancy in B_1^+ efficiencies between the simulated and physical coil is partially a function of B_1^+ shimming.

The size of the Rx coil had little effect on the B_1^+ efficiency of the dipole coil, regardless of whether the coil was outfitted with or without field probes. This indicates that the active detuning implemented in the receive coil circuitry was sufficient for isolating the transmit and receive electronics. However, B_1^+ efficiency was observed to decrease substantially after integration of the field probes. B_1^+ efficiency decreased by approximately 40% and 47% for the large and small coil configurations, respectively, upon field probe addition. This suggests a significant interaction between the transmit coil circuitry and the field probes which could not be compensated by the integration of floating cable traps or retuning and rematching of the individual transmit channels. This was not observed by Gilbert et al., who saw no significant alterations in the B_1^+ efficiency of their coil after probe integration.⁵⁵ Although, in our design, all probes and their respective cabling were maintained at least 1 cm away from any conductive structures of the transmit coil, it is still possible that additional clearance must be given to minimize coupling between the probes and transmit elements. Owing to the prototypical nature of our housing design, Skope NMR probes and their cables were fastened to the coil housing using Velcro tape. This was done in an effort to ease optimization of the probe positions. However, this method of fixing the probes was not ideal, as it did not fully immobilize the probes on the coil, allowing some probes and cables to subtly vibrate. Future development of our coil will aim to address this problem by better securing the probes and minimizing probe and cable vibrations.

The transmit coil S-parameters were measured using the directional couplers of the MRI scanner at both the largest and smallest size of the Rx coil, with and without probes. After probe integration, the Tx coil elements were retuned and rematched in the scanner to compensate for the effects of integrating the probes. Tx S-parameters were then recorded again. The mean and maximum reflection and coupling coefficients for each coil configuration are summarized in **Table 3**. Though there were differences in the transmit S-parameters pre- and post-probe integration, these differences were effectively compensated by retuning and rematching the Tx coil. After this compensation procedure, all reflection coefficients were maintained below -15 dB.

Table 3: Summary of Tx scattering parameter results.

Coil Configuration:	Large	Large with probes	Large with probes after optimization	Small	Small with probes	Small with probes after optimization
Average Reflection [dB]	-19.3	-11.6	-20.9	-19.9	-16.2	-20.5
Worst Reflection [dB]	-15.1	-3.6	-15.4	-15.5	-11.2	-16.8
Average Coupling [dB]	-21.2	-23.6	-21.4	-21.7	-21.9	-22
Worst Coupling [dB]	-7.9	-8.7	-8.5	-7	-8.7	-8.6

6.2 Discussion of Receive Coil Results

The measured Q ratios for two representative loops of the phased array were 7.2 for the large loop and 6.3 for the small loop, indicating that the coil was operating in the sample noise dominated regime. Active detuning of our phased array receive elements was successful at isolating the transmit and receive electronics during application of the RF transmit pulse. This was demonstrated by the consistency of the mean B_1^+ efficiency measured at the center of the phantom for different sizes of the receive coil – large and small B_1^+ efficiencies differed by approximately 5%.

Variations in the noise correlation between individual receive channels were also observed between coil sizes. This is in line with changes in noise correlation observed by Ghotra et al.²⁷ It is expected, as geometric decoupling is altered upon adjustment of the receive coil dimensions. At our largest coil size, maximum Rx noise correlation was considerably worse than the maximum noise correlation at the smaller Rx coil size. In both the large and small configurations of the coil, the maximum noise correlation (68.5% and 55.7%, respectively) was considerably higher than the mean (12.7% and 12.2%, respectively). This indicates that a small subset of the elements of the total 32-channel array may be contributing to a degradation in overall coil performance. Channel

combinations with noise correlations above 50% for the different coil configurations are listed in **Table 4**.

Table 4: Channel combinations with noise correlations above 50%. Worst case, maximum noise correlations for each coil configuration are listed in red, and channel combinations with higher than 60% noise correlation are listed in yellow.

Coil Configurations:							
Large		Large with Probes		Small		Small with probes	
Channels	Noise Correlation	Channels	Noise Correlation	Channels	Noise Correlation	Channels	Noise Correlation
13-15	50.20%	13-14	55.50%	9-17	55.70%	9-17	58.40%
14-15	56.10%	13-15	57.40%			16-23	51.60%
17-18	68.50%	14-15	63.30%				
17-19	54.80%	14-16	50.80%				
17-26	62.40%	15-16	59.10%				
18-26	52%	17-18	71.30%				
		17-19	62.80%				
		17-26	60.80%				
		18-19	50.90%				

The coil configuration with the worst noise correlation performance was the large coil with the integrated field probes. It had nine channel combinations with noise correlations above 50%. The small coil demonstrated the best noise correlation performance, with only one pair of channels above 50% noise correlation (channels 9 and 17). Channel 17 demonstrated correlations above 50% with other channels in all coil configurations, indicating that this channel in particular should be targeted for improved preamplifier decoupling. Though our maximum noise correlation measures were higher than those in other reported studies, mean noise correlation at all sizes of our proposed coil was similar to those recorded by Ghotra et al. (11.3 – 9.1%), Gilbert et al. (9.5%) and Rios et al. (14 – 8.7%).²⁶⁻²⁸

SNR maps were generated from GRE images of the NiSO₄ × 6H₂O doped water phantom at both the largest and smallest dimensions of the Rx coil. This was done with and without probes. SNR maps were also generated using the commercial, human 7 T Nova coil. The average central and peripheral SNR of the pediatric coil and Nova coil generated by covariance-weighted root-sum-of-squares (RSS-COV) reconstruction is listed in **Table 5**.

Table 5: Mean central and peripheral SNR generated from root sum-of-squares covariance weighted reconstruction of GRE images of a $\text{NiSO}_4 \times 6\text{H}_2\text{O}$ doped water phantom.

SNR In Phantom		
Coil Configuration	Mean Central SNR	Mean Peripheral SNR
Large	303	214
Large w/ probes	269	193
Small	339	262
Small w/ probes	316	255
Nova	410	261

Our pediatric coil demonstrated more spatially uniform SNR performance over the length of the sensitive region of the receive coil compared to the Nova coil, as well as equivalent or higher SNR in the region of the phantom corresponding to the lower part of the brain. However, importantly, the Nova coil still demonstrated higher SNR in the region of the phantom corresponding to the top part of the brain (i.e., near the top of the Rx array). In terms of average peripheral SNR, the performance of the pediatric coil at its smallest size was comparable to the performance of the Nova coil. However, these comparisons are subject to the caveat that the Nova coil B_1^+ shim weights were optimized, while those of the pediatric coil were not.

Of note, the SNR of the pediatric coil could also be improved by addressing the increased noise correlation in the channels specified in **Table 4**. In particular, we believe that choice of an appropriate phase shifter strategy for preamplifier decoupling of these channels would improve our pediatric coil's SNR.

SNR maps were also generated from *in vivo*, GRE images of a 33-year-old healthy adult male subject. These images were collected with the largest size of the pediatric coil *and* with the Nova coil, for comparison. The Nova coil displayed higher average SNR in the brain. The pediatric coil produced roughly 58.2% and 56.5% of the central and peripheral SNR of the Nova, respectively. This can partially be attributed to the fact that the B_1^+ field of the pediatric coil was not yet optimized, particularly for imaging the adult human head.

Integration of the field probes caused a modest reduction in SNR, particularly at the larger size of the receive coil. In the rigid coil design developed by Gilbert et al. retuning and rematching the Rx coil to compensate for probe integration resulted in minor reductions of local SNR, but minimal changes to mean SNR over the brain before and after probe integration.⁵⁵ In our array, the

mechanical design of the receive former made it more difficult to retune the pediatric receive coil after integrating the probes. Such re-tuning of the Rx elements after probe integration is a future direction.

Parallel imaging performance is an important consideration in the design of phased array coils. It is particularly beneficial for pediatric imaging studies due to the reduced scan times of accelerated acquisitions. Parallel imaging performance can be quantified by g-factor maps, which give an indication of coil-geometry related SNR reductions. The generation of g-factor maps was not performed in this thesis but should be considered in future development and evaluation of the coil to provide a more comprehensive assessment of coil performance.

6.3 NMR Field Probe Results

Field probe performance was not notably affected upon integration of the NMR probes with the Tx coil. This was particularly true with the coil in its smallest size. Mean normalized FID signal after 30 ms was comparable between FIDs measured on the scaffold (43% of initial magnitude) and FIDs measured on the coil configured in its smallest size (40% of initial magnitude). These results are comparable to findings evaluated by Gilbert et al., showing modest reductions in probe FID signal lifetimes when the probes were integrated into their adult 7T head RF coil.⁵⁵

Restrictions on where the NMR field probes could be placed, given the geometry of the dipole Tx coil, meant that the probes could not be positioned optimally when placed on the coil, (i.e., as they are on the scaffold). As such, only 2nd order correction of the k-space trajectories was possible given the probe positioning on the coil, compared to the 3rd order correction achieved with Skope measurements on the manufacturer's scaffold. Gilbert et al. also observed reductions in the fidelity of measuring 3rd order spherical harmonics for dynamic B_0 field correction as a result of probe positioning on their custom coil.⁵⁵

6.4 Imaging Results

Spoiled 2D GRE images of a healthy 33-year-old adult human subject were acquired using the pediatric coil and the Nova coil. This was done to demonstrate the performance of the pediatric coil and to provide a qualitative comparison between the pediatric and commercial coils. The image acquired using the pediatric coil shows some B_1^+ -induced variations in signal intensity

throughout the brain. This was expected given the pediatric coil transmit field had not yet been comprehensively optimized.

To demonstrate the performance of the pediatric coil for dynamic pTx mode brain imaging, MPRAGE images of a healthy 33-year-old adult human subject were acquired with our pediatric coil (base resolution: 288, voxel size: $0.8 \times 0.8 \times 0.8 \text{ mm}^3$, slabs: 1, number of slices per slab: 224, TE: 2.79 ms, TR: 6220 ms, flip angle: 4° , BW: 260 Hz/Px, number of averages: 1). The same adult subject was then imaged with matched MPRAGE parameters using the Nova commercial coil. Representative slices from these imaging experiments, showing the sagittal, axial and coronal planes, are displayed in **Figure 20**.

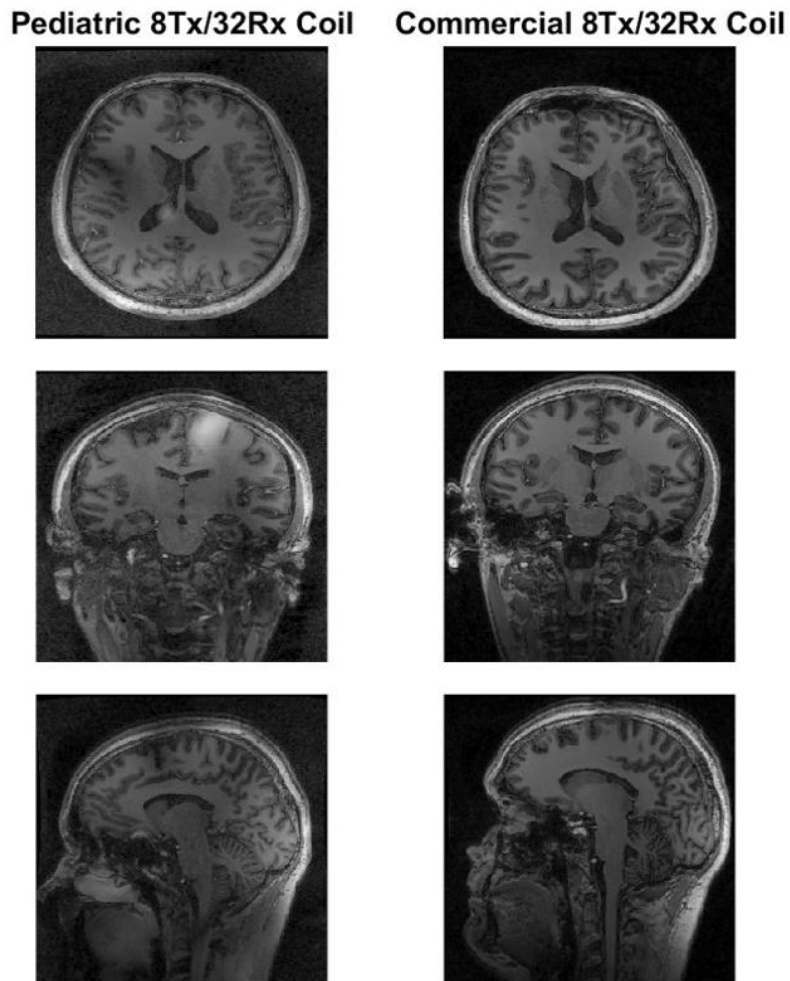


Figure 20: In vivo MPRAGE image of adult human taken with the pediatric coil adjusted to its maximum size (left) and the commercial Nova coil (right) showing axial, coronal and sagittal planes.

To mitigate B_1^+ -induced variations, we applied pTx pulses. However, these were designed by Siemens for the Nova coil. The MPRAGE images acquired using the pediatric coil show B_1^+ -induced variations in signal intensity throughout the brain. This was expected given a) the pediatric coil transmit field had not yet been comprehensively optimized and b) the MPRAGE pTx pulses were designed for the Nova coil. In future, custom pediatric pTx excitation pulses are planned, which would allow more robust comparison of our design to the commercial Nova coil. However, design of such pTx excitations was beyond the scope of the present thesis.

6.5 Future Directions

The size-adaptive RF coil presented in this thesis enables the safe application of 7 T MRI for pediatric neuroimaging. Nonetheless, the coil, in its current configuration, has several limitations.

The mechanical design of the Rx former was a “proof of principle design”. Although our Rx array elements were physically separated, preamplifiers were mounted to a single rigid structure at the top of the head. As such, cabling of all Rx elements required a wired connection to a preamplifier box. Due to the Rx cabling, adjustments to the Rx circuitry necessitated partial disassembly of the former. Such disassembly is not ideal as it resulted in cable tension (and sometimes shearing), requiring repair and further disassembly of the coil (**Figure 21**).



Figure 21: Testing setup used to optimize performance of individual Rx array elements. Since cabling from each component of the Rx former was fed to a single mechanical structure housing the preamplifiers at the top of the coil, optimization of elements required some disassembly of the adjustable pieces. Future designs are seeking to improve the stability of electrical and mechanical components of the size adjustable array design.

Apart from the four internal components which form the shape of the Rx former helmet, the Rx coil was entirely printed in the RF laboratory of the McConnell Brain Imaging Centre at McGill University using a Makerbot Replicator+ 3D printer (UltiMaker, USA). Many of the components of the Rx coil could not be printed in one-piece using this printer and had to be combined from multiple separate pieces using epoxy. This somewhat reduced the overall structural integrity of the former. In particular, the adjustable former relied on 3D printed plastic threads for size adjustment. These threads are presently being redesigned to better withstand mechanical forces and repeated use in the case of pediatric imaging.

An additional focus of effort in this thesis was placed on developing an updated Rx former (“version 2”) to address the challenges described above. The updated Rx former is described in

detail in the Appendix. Because the size-adjustable nature of the Rx coil requires a certain level of precision and durability, new iterations of the former are now being printed using larger 3D printers capable of accommodating the size of the components. The second version of the former includes mechanical components, such as more robust threads, to improve mechanical durability.

The noise correlation matrices (Chapter 5, **Figure 13**) acquired for our 7 T pediatric coil indicate further optimization of the Rx coil decoupling, particularly for channel 17, may be required in order to reduce inter-element coupling. Minimizing such coupling is important for ensuring high image quality. Refined preamplifier decoupling could also be investigated to better isolate individual elements of the Rx array. Furthermore, optimization of the B_1^+ excitation field is still underway to improve B_1^+ homogeneity. Though we investigated the CP^+ mode excitation of the transmit coil, development of the pTx functionality, using high quality B_1^+ shimming or 3D RF pulses, is warranted.

The performance of the pediatric coil was reduced, in terms of SNR and B_1^+ efficiency, after integration of the NMR field probes. This was not observed in a previous 7T study conducted by Gilbert et al.⁵⁵ Re-tuning and matching the Rx coil elements to compensate for the addition of the field probes, as was performed by Gilbert et al., would likely improve the performance of our Rx array after probe integration. However, this was beyond the scope of the present thesis. Further optimization of probe positioning and isolation of the NMR field probes from the transmit and receive elements (i.e., by implementing more rigorous common-mode current suppression techniques) could also be investigated to reduce the coupling of probe and coil electronics.

Although the coil described in this work was designed for pediatric imaging, 7 T imaging of pediatric subjects was not possible within the time frame of this thesis due to considerations related to McGill ethics approval for imaging subjects below 18 years of age at 7 T. However, this is a future aim with our design.

6.6 Conclusion

In this thesis, we developed a size-adaptive, RF coil with integrated NMR field probes for pediatric neuroimaging at 7 T. The design consisted of an eight-channel parallel transmit coil with eight notched dipole elements and a 32-channel size-adaptive conformal, receive array. The coil was

optimized in terms of SAR for pediatric imaging through simulation and the development of VOP-based SAR safety factors. Imaging experiments performed with the pediatric coil demonstrate its potential for high-quality pediatric neuroimaging. We also identified additional optimization steps required to, in future, improve coil performance. Additional development and optimization of the 7 T coil is expected to enable high quality pediatric brain imaging at UHF. Such imaging has the potential to provide more detailed estimation of the structure and function of the human brain during neurodevelopment.

References

1. Kraff O, Fischer A, Nagel AM, Mönninghoff C, Ladd ME. MRI at 7 tesla and above: Demonstrated and potential capabilities: Capabilities of MRI at 7T and Above. *J Magn Reson Imaging*. 2015;41(1):13-33. doi:10.1002/jmri.24573
2. Dajia C, Ditchfield M. 3T MRI in paediatrics: Challenges and clinical applications. *European Journal of Radiology*. 2008;68(2):309-319. doi:10.1016/j.ejrad.2008.05.019
3. Thomas BP, Welch EB, Niederhauser BD, et al. High-resolution 7T MRI of the human hippocampus in vivo. *J Magn Reson Imaging*. 2008;28(5):1266-1272. doi:10.1002/jmri.21576
4. Cai Y, Hofstetter S, van der Zwaag W, Zuiderbaan W, Dumoulin SO. Individualized cognitive neuroscience needs 7T: Comparing numerosity maps at 3T and 7T MRI. *NeuroImage*. 2021;237:118184. doi:10.1016/j.neuroimage.2021.118184
5. Keuken MC, Bazin PL, Schäfer A, Neumann J, Turner R, Forstmann BU. Ultra-High 7T MRI of Structural Age-Related Changes of the Subthalamic Nucleus. *J Neurosci*. 2013;33(11):4896-4900. doi:10.1523/JNEUROSCI.3241-12.2013
6. van Rooden S, Versluis MJ, Liem MK, et al. Cortical phase changes in Alzheimer's disease at 7T MRI: A novel imaging marker. *Alzheimer's & Dementia*. 2014;10(1):e19-e26. doi:10.1016/j.jalz.2013.02.002
7. Kerchner GA. Ultra-High Field 7T MRI: A New Tool for Studying Alzheimer's Disease. Ashford JW, Rosen A, Adamson M, et al., eds. *JAD*. 2011;26(s3):91-95. doi:10.3233/JAD-2011-0023
8. McKiernan EF, O'Brien JT. 7T MRI for neurodegenerative dementias in vivo: a systematic review of the literature. *J Neurol Neurosurg Psychiatry*. 2017;88(7):564-574. doi:10.1136/jnnp-2016-315022
9. Kolb H, Absinta M, Beck ES, et al. 7T MRI Differentiates Remyelinated from Demyelinated Multiple Sclerosis Lesions. *Annals of Neurology*. 2021;90(4):612-626. doi:10.1002/ana.26194
10. Nielsen AS, Kinkel RP, Madigan N, Tinelli E, Benner T, Mainero C. Contribution of cortical lesion subtypes at 7T MRI to physical and cognitive performance in MS. *Neurology*. 2013;81(7):641-649. doi:10.1212/WNL.0b013e3182a08ce8
11. Opheim G, Van Der Kolk A, Bloch KM, et al. 7T Epilepsy Task Force Consensus Recommendations on the Use of 7T MRI in Clinical Practice. *Neurology*. 2021;96(7):327-341. doi:10.1212/WNL.0000000000011413
12. De Ciantis A, Barba C, Tassi L, et al. 7T MRI in focal epilepsy with unrevealing conventional field strength imaging. *Epilepsia*. 2016;57(3):445-454. doi:10.1111/epi.13313

13. Wang I, Oh S, Blümcke I, et al. Value of 7T MRI and post-processing in patients with nonlesional 3T MRI undergoing epilepsy presurgical evaluation. *Epilepsia*. 2020;61(11):2509-2520. doi:10.1111/epi.16682
14. Lehericy S, Bardinet E, Poupon C, Vidailhet M, François C. 7 tesla magnetic resonance imaging: A closer look at substantia nigra anatomy in Parkinson's disease: 7T MRI in PD. *Mov Disord*. 2014;29(13):1574-1581. doi:10.1002/mds.26043
15. Plantinga BR, Temel Y, Duchin Y, et al. Individualized parcellation of the subthalamic nucleus in patients with Parkinson's disease with 7T MRI. *NeuroImage*. 2018;168:403-411. doi:10.1016/j.neuroimage.2016.09.023
16. Maruyama S, Fukunaga M, Fautz HP, Heidemann R, Sadato N. Comparison of 3T and 7T MRI for the visualization of globus pallidus sub-segments. *Sci Rep*. 2019;9(1):18357. doi:10.1038/s41598-019-54880-x
17. Van Veluw SJ, Zwanenburg JJ, Engelen-Lee J, et al. *In Vivo* Detection of Cerebral Cortical Microinfarcts with High-Resolution 7T MRI. *J Cereb Blood Flow Metab*. 2013;33(3):322-329. doi:10.1038/jcbfm.2012.196
18. Van Der Kolk AG, Hendrikse J, Zwanenburg JJM, Visser F, Luijten PR. Clinical applications of 7T MRI in the brain. *European Journal of Radiology*. 2013;82(5):708-718. doi:10.1016/j.ejrad.2011.07.007
19. Barkovich MJ, Xu D, Desikan RS, Williams C, Barkovich AJ. Pediatric neuro MRI: tricks to minimize sedation. *Pediatr Radiol*. 2018;48(1):50-55. doi:10.1007/s00247-017-3785-1
20. Copeland A, Silver E, Korja R, et al. Infant and Child MRI: A Review of Scanning Procedures. *Front Neurosci*. 2021;15:666020. doi:10.3389/fnins.2021.666020
21. Barkovich MJ, Li Y, Desikan RS, Barkovich AJ, Xu D. Challenges in pediatric neuroimaging. *NeuroImage*. 2019;185:793-801. doi:10.1016/j.neuroimage.2018.04.044
22. Malik SJ, Hand JW, Carmichael DW, Hajnal JV. Evaluation of specific absorption rate and heating in children exposed to a 7T MRI head coil. *Magnetic Resonance in Med*. 2022;88(3):1434-1449. doi:10.1002/mrm.29283
23. Zaitsev M, Maclaren Julian, Herbst M. Motion Artefacts in MRI: a Complex Problem with Many Partial Solutions. *J Magn Reson Imaging*. 2015;42(4):887-901. doi:10.1002/jmri.24850
24. Rollins JD, Collins JS, Holden KR. United States Head Circumference Growth Reference Charts: Birth to 21 Years. *The Journal of Pediatrics*. 2010;156(6):907-913.e2. doi:10.1016/j.jpeds.2010.01.009
25. Keil B, Alagappan V, Mareyam A, et al. Size-optimized 32-channel brain arrays for 3 T pediatric imaging: Pediatric Brain Arrays. *Magn Reson Med*. 2011;66(6):1777-1787. doi:10.1002/mrm.22961

26. Gilbert KM, Nichols ES, Gati JS, Duerden EG. A radiofrequency coil for infants and toddlers. *NMR in Biomedicine*. 2023;36(8):e4928. doi:10.1002/nbm.4928
27. Ghotra A, Kosakowski HL, Takahashi A, et al. A size-adaptive 32-channel array coil for awake infant neuroimaging at 3 Tesla MRI. *Magnetic Resonance in Med*. 2021;86(3):1773-1785. doi:10.1002/mrm.28791
28. Lopez Rios N, Foias A, Lodygensky G, Dehaes M, Cohen-Adad J. Size-adaptable 13-channel receive array for brain MRI in human neonates at 3 T. *NMR in Biomedicine*. 2018;31(8):e3944. doi:10.1002/nbm.3944
29. Duerst Y, Wilm BJ, Dietrich BE, et al. Real-time feedback for spatiotemporal field stabilization in MR systems. *Magnetic Resonance in Medicine*. 2015;73(2):884-893. doi:10.1002/mrm.25167
30. Duerst Y, Wilm BJ, Wyss M, et al. Utility of real-time field control in T2*-Weighted head MRI at 7T. *Magnetic Resonance in Medicine*. 2016;76(2):430-439. doi:10.1002/mrm.25838
31. Deniz CM. Parallel Transmission for Ultrahigh Field MRI. *Topics in Magnetic Resonance Imaging*. 2019;28(3):159-171. doi:10.1097/RMR.000000000000204
32. Panych LP, Madore B. The physics of MRI safety: Physics of MRI Safety. *J Magn Reson Imaging*. 2018;47(1):28-43. doi:10.1002/jmri.25761
33. Hoff MN, McKinney A, Shellock FG, et al. Safety Considerations of 7-T MRI in Clinical Practice. *Radiology*. 2019;292(3):509-518. doi:10.1148/radiol.2019182742
34. Jin JM. *Electromagnetic Analysis and Design in Magnetic Resonance Imaging*. CRC Press; 1998.
35. Brown RW, Cheng YCN, Haacke EM, Thompson MR, Venkatesan R. *Magnetic Resonance Imaging: Physical Principles and Sequence Design*. Second edition. John Wiley & Sons, Inc; 2014.
36. Prince JL, Links JM. *Medical Imaging Signals and Systems*. 2nd ed. Pearson; 2015.
37. Webb A. CHAPTER 3. Radiofrequency Coils. In: Webb AG, ed. *New Developments in NMR*. Royal Society of Chemistry; 2016:81-165. doi:10.1039/9781782623878-00081
38. Vaughan JT, Griffiths JR, eds. *RF Coils for MRI*. John Wiley and Sons Ltd; 2012.
39. Mispelter J, Lupu M, Briguet A. *NMR Probeheads for Biophysical and Biomedical Experiments: Theoretical Principles & Practical Guidelines*. Second edition. Imperial College Press; 2015.
40. Gruber B, Froeling M, Leiner T, Klomp DWJ. RF coils: A practical guide for nonphysicists: RF Coils. *J Magn Reson Imaging*. 2018;48(3):590-604. doi:10.1002/jmri.26187

41. Roemer PB, Edelstein WA, Hayes CE, Souza SP, Mueller OM. The NMR phased array. *Magn Reson Med.* 1990;16(2):192-225. doi:10.1002/mrm.1910160203
42. Haase A, Odoj F, Von Kienlin M, et al. NMR probeheads for in vivo applications. *Concepts in Magnetic Resonance.* 2000;12(6):361-388. doi:10.1002/1099-0534(2000)12:6<361::AID-CMR1>3.0.CO;2-L
43. Deshmane A, Gulani V, Griswold MA, Seiberlich N. Parallel MR imaging. *J Magn Reson Imaging.* 2012;36(1):55-72. doi:10.1002/jmri.23639
44. Katscher U, Börnert P. Parallel RF transmission in MRI. *NMR Biomed.* 2006;19(3):393-400. doi:10.1002/nbm.1049
45. Brink WM, Yousefi S, Bhatnagar P, Remis RF, Staring M, Webb AG. Personalized local SAR prediction for parallel transmit neuroimaging at 7T from a single T1 -weighted dataset. *Magnetic Resonance in Med.* 2022;88(1):464-475. doi:10.1002/mrm.29215
46. Grainger MD. IPEM MR SIG Metrasens Ltd.
47. Irwin JD, Nelms RM. *Basic Engineering Circuit Analysis.* 11th edition. Wiley; 2015.
48. Pozar DM. *Microwave Engineering.* 4th ed. Wiley; 2012.
49. Gross S, Barmet C, Dietrich BE, Brunner DO, Schmid T, Pruessmann KP. Dynamic nuclear magnetic resonance field sensing with part-per-trillion resolution. *Nat Commun.* 2016;7(1):13702. doi:10.1038/ncomms13702
50. Barmet C, Zanche ND, Pruessmann KP. Spatiotemporal magnetic field monitoring for MR. *Magnetic Resonance in Medicine.* 2008;60(1):187-197. doi:10.1002/mrm.21603
51. Brunner DO, Dietrich BE, Çavuşoğlu M, et al. Concurrent recording of RF pulses and gradient fields - comprehensive field monitoring for MRI: Comprehensive Field Monitoring. *NMR Biomed.* 2016;29(9):1162-1172. doi:10.1002/nbm.3359
52. Duerst Y, Wilm BJ, Dietrich BE, et al. Real-time feedback for spatiotemporal field stabilization in MR systems: Feedback for Spatiotemporal Field Stabilization. *Magn Reson Med.* 2015;73(2):884-893. doi:10.1002/mrm.25167
53. Wilm BJ, Nagy Z, Barmet C, et al. Diffusion MRI with concurrent magnetic field monitoring: Diffusion MRI with Concurrent Magnetic Field Monitoring. *Magn Reson Med.* 2015;74(4):925-933. doi:10.1002/mrm.25827
54. Brunner D, Gross S, Schmid T, et al. Integration of field monitoring for neuroscientific applications - SNR, acceleration and image integrity. In: ; 2019. Accessed July 18, 2023. <https://cds.ismrm.org/protected/19MProceedings/PDFfiles/1046.html>

55. Gilbert KM, Dubovan PI, Gati JS, Menon RS, Baron CA. Integration of an RF coil and commercial field camera for ultrahigh-field MRI. *Magnetic Resonance in Med.* 2022;87(5):2551-2565. doi:10.1002/mrm.29130
56. Yazdanbakhsh P, Sprang C, Couch M, Hoge R, Tardif C, Rudko D. Evaluation of 8-Channel Transmit Dipoles and 8-Channel Transmit Loops for Pediatric Visual Cortex Imaging at 7 T. In: *Proc. Intl. Soc. Mag. Reson. Med.* 31 (2023). ; 2023.
57. Clément J, Gruetter R, Ipek Ö. A combined 32-channel receive-loops/8-channel transmit-dipoles coil array for whole-brain MR imaging at 7T. *Magnetic Resonance in Med.* 2019;82(3):1229-1241. doi:10.1002/mrm.27808

Appendix

Updated Rx Former Design

An additional focus of this thesis which has not yet been presented is the development of an updated Rx former meant to build upon the current former design. This work was motivated by the limitations of the previous design and aimed specifically to improve the overall workability of the coil in terms of assembly, repair and setup, as well as to improve patient comfort. The updated former design is shown in **Figure 22**.

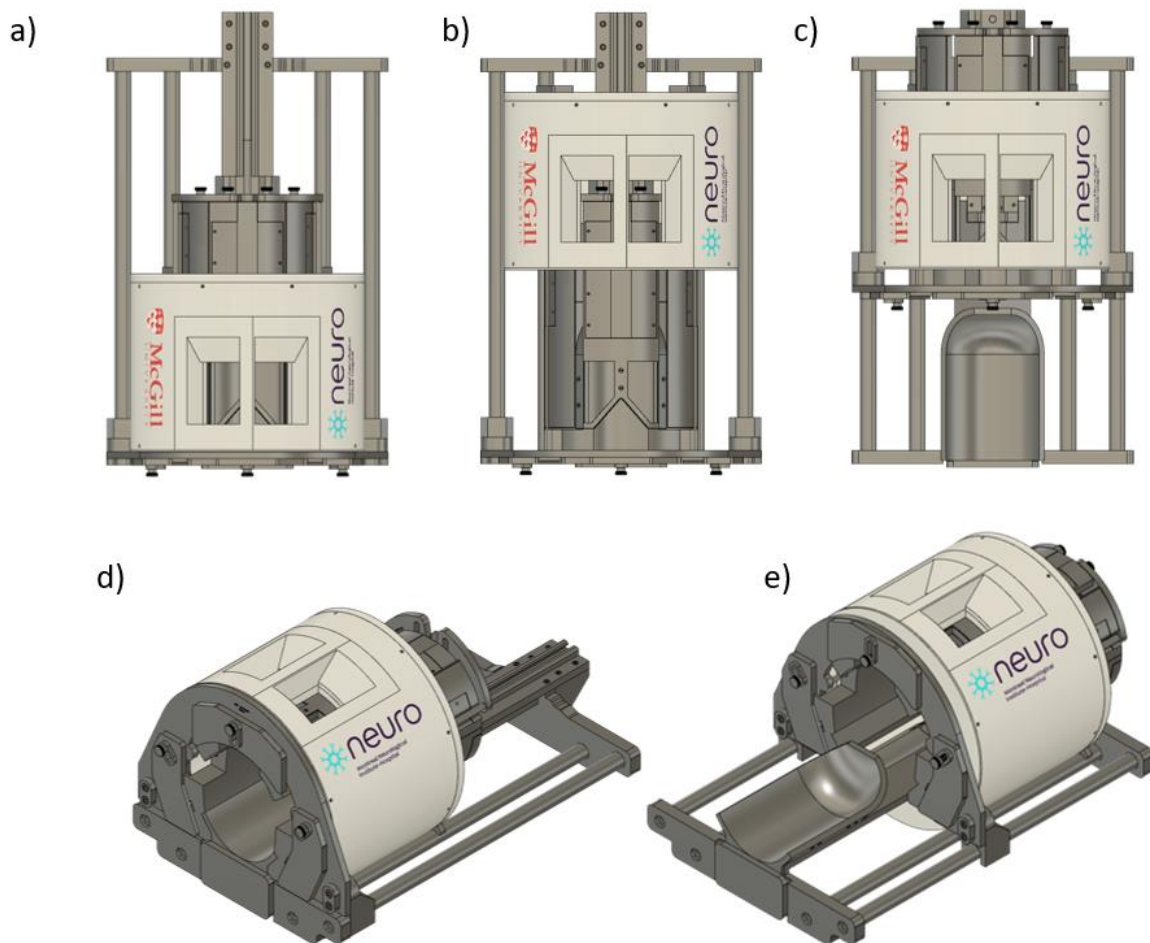


Figure 22: Updated former design with receive coil housing and base in gray and transmit coil housing in white: a) top view of coil with Tx and Rx coil in position for imaging, b) top view with Tx coil removed, c) top view with Rx and Tx coil removed to enable easy positioning of subject, d) isometric view with Tx and Rx coils in position for imaging, and e) isometric view with Tx and Rx coils removed for easy positioning of the subject.

The main difference between the original and updated former designs is the complete electrical separation of the individual components of the receive former. Although receive loops were separated between the individual pieces of the Rx former in the original design, all preamplifiers were mounted to the same, rigid, mechanical structure. As such, each piece of the Rx former was physically connected by the coaxial cables connecting the preamplifiers and receive elements. This presented a challenge for repairing and optimizing the receive array, often requiring the partial disassembly of the coil. To address this limitation in the previous design, the new Rx coil former consists of four, completely physically separable components. This was achieved by integrating the preamplifiers directly into the individual pieces of the former rather than mounting all preamplifiers onto a separate, rigid structure (**Figure 23**). This revision in the design allows for each electrical subsystem of the Rx coil to be easily removed for repair or optimization.

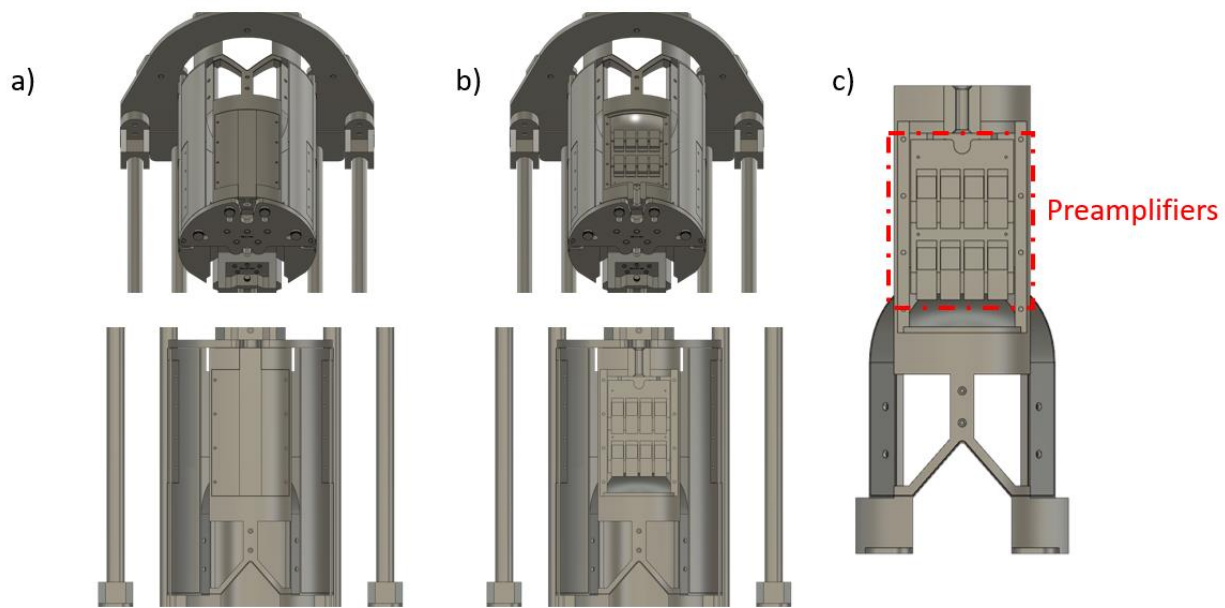


Figure 23: Updated pediatric receive coil housing: a) view of anterior component of the receive coil former, b) view of anterior component of the receive coil former showing cavity for housing preamplifiers, and c) anterior component of the receive coil former separated from the full 32-channel phased array, showing cavity for housing preamplifiers.

The revised former design also includes an updated former support base. The new support base utilizes a rail system that enables both the Tx coil and all but the bottom piece of the Rx coil to be easily repositioned. This allows for easy adjustment of the coil size as well as easy positioning of the subject. It also ensures that the Tx and Rx coil subsystems are maintained in the optimal relative

positions, which can be fixed using a thumbscrew based locking system. The updated former design still enables adjustments in the lateral-medial and anterior-posterior directions to accommodate subjects with head sizes between the 5th and 95th percentile of children aged 4-9 years-old (**Figure 24**).

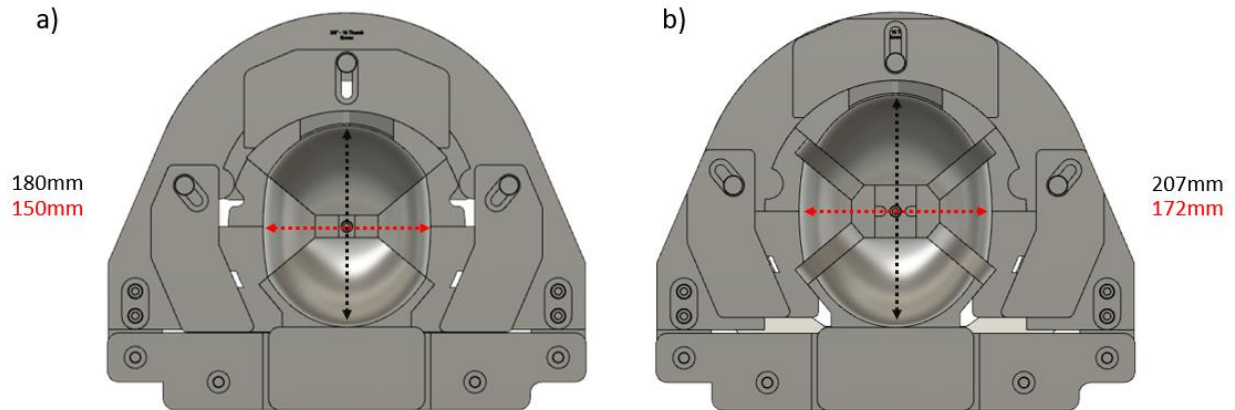


Figure 24: View of updated pediatric coil at a) the smallest size of the receive coil housing and b) the largest size of the receive coil housing.